HIGH-PRESSURE MICRODISCHARGES AS MICROREACTORS FOR MATERIALS APPLICATIONS

Thesis By

Ramanathan Mohan Sankaran

In Partial Fulfillment of the Requirements for the

Degree of

Doctor of Philosophy

CALIFORNIA INSTITUTE OF TECHNOLOGY

Pasadena, California

2004

(Defended May 27, 2004)

© 2004

Ramanathan Mohan Sankaran

All Rights Reserved

ACKNOWLEDGMENTS

When I began my studies at Caltech, the idea of completing a thesis seemed overwhelming. As the years have passed, it has come together slowly, step by step, and in the end, finally come into focus. All of this would not have been possible without the help and support of countless people.

My advisor, Costas Giapis, has been a mentor and this thesis embodies what he has instilled in me: the freedom to explore new ideas without the fear of failing. He has allowed me to be independent and creative and shape the direction of my thesis. During my time, we have worked on many projects with some successes and some failures along the way. In the end, the experiences have given me a broad exposure and knowledge base that gives me confidence for whatever new challenges lie ahead.

My research group has changed a lot over the years. The one constant was Mike Gordon who introduced me to vacuum technology and was always there to help me with new experiments. I'll always remember the chats during our afternoon coffee breaks that have contributed to this work.

An indispensable part of my thesis has been learning how to machine parts. Mike Roy (Chemistry Machine Shop) trained me and always offered his time and immense skill set to help me. There are several parts of my thesis that could not have been accomplished without his assistance.

The experimental work contained in this thesis was a result of numerous collaborations both on and off campus. Dr. Ali Ghaffari (Applied Physics) helped me learn SEM (Chapter 3) in the Watson Laboratory. Micro-Raman spectroscopy (Chapter 4) was

done with Elizabeth Miura in Dr. George Rossman's group (Geology). Dr. Chi Ma (Geology) trained me to use the SEM/EDS (Chapter 6) in the Geology Analytical Facility. Carol Garland (Materials Science) did the TEM work (Chapter 6) and helped me gain an appreciation for "hi-res." PL measurements on liquid samples (Chapter 6) were done with Dave Flanagan in Dr. David Tirrell's group (Chemical Engineering). Robb Walters helped me with PL of films (Chapter 6) in Dr. Harry Atwater's lab (Applied Physics).

Excimer measurements (Chapter 5) were done at Old Dominion University in Dr. Karl Schoenbach's lab (Electrical and Computer Engineering). His post-doc, Mohammed Moselhy, was kind enough to host me during my two visits there and taught me many things about the most difficult type of spectroscopy. I especially enjoyed stimulating discussions with Dr. Schoenbach who is a true scientist.

The nanoparticle synthesis (Chapter 6) is the culmination of joint work with a fellow graduate student, Dean Holunga, and Dr. Richard Flagan (Chemical Engineering). Dean has introduced me to aerosol growth, mobility analyzers, and the toughest material to grow and characterize, silicon nanocrystals. I have been a part of the RCF lab in Keck for my final two years and I have appreciated the comraderie with Dean, Adam, and Tim both inside and outside the lab (where the grass is always greener). Dr. Flagan has been a pseudo-advisor and a mentor whose imaginative input into this project has been a source of inspiration.

All the friends and classmates I have interacted with over the years have been a special part of my experience here at Caltech. My neighbors down the hall in the Davis group have always dropped by to say hello and shoot the breeze. If it wasn't for fantasy sports, I wouldn't need to use the Internet! Lunch breaks with Pops were always a nice getaway to vent about all my problems.

I received an immeasurable amount of support during my Ph.D. from my family. Their constant motivation and love has been something I can never express in words. My parents and my sister have been there to give me words of encouragement, make me laugh, and tell me all about how hard they've had it. I'm in a family of engineers and it's humbling to know that in some ways, all of this has already been done.

-Mohan Sankaran

Pasadena, CA

May 2004

ABSTRACT

This thesis describes a novel "microplasma" source that is suitable for microreactor applications. The high-pressure "microplasma" is a direct current microdischarge, formed between two metal electrodes: a cathode with a pin-hole (diameter~100 μm) and an anode of unspecified shape. Strong radial electric fields are produced in the microhollow cathode geometry, causing electrons to oscillate (Pendel effect). As a result of enhanced ionization processes, it is possible to produce a stable high-intensity discharge at pressures of 1 atmosphere or higher. We have utilized these microdischarges for several applications including pattern transfer, diamond deposition, excimer emission, and nanoparticle synthesis.

Maskless etching of structures for MEMS and microfluidic applications is achieved by forming microplasmas in complex patterns within a stencil mask in contact with the surface to be patterned. In one application, CF_4/Ar microdischarges are formed inside planar copper-polyimide stencil masks that permit direct etching of silicon wafers. To deposit films, microdischarges are formed inside metal capillaries that accommodate flow. A plasma microjet is created and directed towards a heated substrate that enables deposition of polycrystalline diamond films over small spatial scales. Simultaneous operation of multiple micodischarges could form the basis of a combinatorial tool for rapid materials development.

Microdischarges in capillary tubes can serve as sources of intense UV radiation. Excimer emission in argon (Ar_2^*) at 128 nm has been studied by vacuum UV spectroscopy. A method to increase the on-axis excimer radiation is demonstrated by adding discharges in

a linear array. Building of emitting volume shows potential for intensifying excimer emission.

The properties of microdischarges are especially conducive to applications as short-residence time reactors. For example, microdischarges are attractive for nanoparticle synthesis since the residence time of particle nucleation can be limited in the reactor to time scales on the order of milliseconds. This methodology has been used to produce silicon particles with mean sizes of 1-5 nm and narrow size distributions. The silicon nanoparticles exhibit blue photoluminescence at room temperature suggesting quantum confinement. The pristine nature of the nanoparticles enables fundamental studies of surface functionalization.

TABLE OF CONTENTS

Acknowledgements iii
Abstract v
Table of contents vii
List of illustrations and tables ix
Preface 1
Chapter 1: From glows to hollow cathodes: formation of an electrical discharge
- 1.1 Introduction to plasmas 3
- 1.2 Electrical breakdown of gases 5
- 1.3 The glow discharge 7
- 1.4 The hollow cathode effect 9

Chapter 2: Atmospheric-pressure microdischarges
- 2.1 Introduction 20
- 2.2 Microdischarge setup 21
- 2.3 Electrical characteristics 23
  - 2.3.1 Planar microdischarge 23
  - 2.3.2 Plasma microjets 24
- 2.4 Optical characteristics 27
  - 2.4.1 Planar microdischarge 27
  - 2.4.2 Plasma microjets 29
- 2.5 Summary 30

Chapter 3: A non-lithographic technique for etching microscale patterns
- 3.1 Introduction 42
- 3.2 Pattern filling: design of a stencil mask 43
- 3.3 Optical characterization of discharge 45
- 3.4 Etching single holes in silicon 45
- 3.5 Etching patterns 49
- 3.6 Summary 50

Chapter 4: Plasma microjets for deposition of polycrystalline diamond films
4.1 Introduction 62
4.2 Polycrystalline diamond films 64
4.3 Optical characterization of discharge 66
4.4 Characterization of films 67
4.5 Summary 70
Chapter 5: Excimer emission from microdischarges in metal capillaries
5.1 Introduction 80
5.2 VUV spectroscopy 82
5.3 Excimer emission 83
5.4 Effect of gas flow 85
5.5 Series operation of microdischarges 86
5.6 Summary 88
Chapter 6: Nanoparticle synthesis in short-residence time microreactors
6.1 Introduction 103
6.2 Aerosol synthesis and characterization 105
6.3 Particle charging 108
6.4 Materials characterization of silicon nanoparticles 109
6.5 Photoluminescence spectroscopy 111
6.6 Summary 114
Chapter 7: Future applications of microdischarges
7.1 Etching 130
7.2 Film deposition 131
7.3 Excimer emission 131
7.4 Nanoparticle synthesis 132
7.5 Gas processing 133
Bibliography 138

LIST OF ILLUSTRATIONS AND TABLES

Figure *Page*

1.1 Space and laboratory plasmas ... 13
1.2 Electron energy distribution function ... 14
1.3 Plane parallel electrode reactor ... 15
1.4 Paschen curve ... 16
1.5 I-V characteristic of a dc glow discharge ... 17
1.6 Regions of a dc glow discharge ... 18
1.7 Hollow cathode discharge ... 19
2.1 Schematic of microhollow cathode discharge ... 32
2.2 Schematic of plasma microjet ... 33
2.3 I-V characteristic of Ar microdischarge ... 34
2.4 I-V characteristic of microdischarge array ... 35
2.5 I-V characteristic of Ar plasma microjet ... 36
2.6 Plasma voltage as a function of cathode-anode gap for Ar plasma microjet ... 37
2.7 Parallel operation of four Ar plasma microjets ... 38
2.8 Emission spectra of Ar microdischarge ... 39
2.9 Emission spectra of Ar plasma microjet ... 40
2.10 Color photographs of Ar plasma microjets ... 41
3.1 Comparison of microscale pattern transfer ... 51
3.2 Schematic diagram of microdischarge setup used for maskless etching ... 52
3.3 Color photographs of CF_4/Ar microdischarge arrays ... 53
3.4 Emission spectra of microdischarges ... 54
3.5 Discharge current versus time ... 55
3.6 SEM images of single holes etched silicon using CF_4/Ar ... 56
3.7 SEM images of singles etched in silicon using SF_6/Ar ... 57
3.8 Plots of discharge current versus time ... 58
3.9 Discharge currents as a function of time with pressure changes ... 59

3.10 SEM image of single hole etched in silicon 60
3.11 SEM images of silicon substrates after direct pattern transfer 61
4.1 Illustration of setup for thin film deposition using a planar microdischarge 71
4.1 Possible configurations for depositing films 72
4.2 Schematic diagram of the setup used for diamond deposition 73
4.3 Emission spectra of H_2 and CH_4/H_2 plasma microjets 74
4.4 SEM images of diamond crystals 75
4.5 Side-on SEM images of diamond particles 76
4.6 SEM image of diamond film 77
4.7 Micro-Raman spectra of diamond films 78
4.8 SEM images of diamond crystals 79
5.1 Emissive wavelengths of various excimer species 89
5.2 Setup for vacuum ultraviolet spectroscopy 90
5.3 Schematic of the microdischarge setup 91
5.4 VUV emission spectra of Ar microdischarge 92
5.5 VUV emission spectra of Xe microdischarge 93
5.6 VUV optical power and discharge voltage as a function of current at 400 Torr 94
5.7 VUV optical power and discharge voltage as a function of current at 600 Torr 95
5.8 VUV optical power and discharge voltage as a function of current at 800 Torr 96
5.9 VUV optical power and discharge voltage as a function of current at 1000 Torr 97
5.10 Ar excimer emission spectra with gas flown through the cathode tube 98
5.11 VUV optical power and discharge voltage as a function of Ar flow rate 99
5.12 Schematic diagram of dual-tube setup 100
5.13 Argon excimer emission spectra from single- and dual-tube microdischarges 101
5.14 VUV optical power from single- and dual-tube microdischarges 102
6.1 Illustration of processes involved in the formation and growth of nanoparticles 116
6.2 Schematic diagram of microdischarge reactor for synthesis of nanoparticles 117
6.3 Schematic cross section of radial differential mobility analyzer 118
6.4 Particle size distributions of np-Si with and without neutralizer 119
6.5 Particle size distributions of np-Si synthesized in SiH_4/Ar microdischarge 120
6.6 Log-normal fits to particle distributions 121
6.7 Size distributions of positively and negatively charged particles 122

6.8 Steady-state charge distribution of particles passed through bipolar charger 123
6.9 Transmission electron micrograph of np-Si 124
6.10 AFM image of np-Si.. 125
6.11 Characterization of np-Si films deposited on molybdenum substrate 126
6.12 Room temperature absorbance, PL excitation, and PL emission 127
6.13 Room temperature PL spectra of np-Si as a function of excitation wavelength........ 128
6.14 Room temperature PL spectra of a np-Si film 129
7.1 Illustration of short contact time millisecond/microsecond reactor 136
7.2 Ozone production in an O_2/Ar plasma microreactor 137

Table *Page*

1.1 Normal cathode fall thicknesses 9
2.1 Argon ion lines and corresponding energies 28
3.1 Maximum width and depth of holes etched in silicon 47
6.1 Emission energy and Stokes shift as a function of excitation energy 113

PREFACE

There has been a recent explosion in interest in the area of microplasmas. Microplasmas are predicted to have applications in a range of disciplines including lighting, labs-on-a-chip, microelectromechanical systems (MEMS), and materials growth. On a fundamental level, study of plasmas at atmospheric-pressure and small spatial scales is a new processing paradigm. Our research has evolved from the development and characterization of a microplasma source to integration of the source in a variety of applications. The bulk of this thesis is devoted to these applications of microdischarges including etching (Chapter 3), deposition (Chapter 4), excimer emission (Chapter 5), and nanoparticle synthesis (Chapter 6).

This work begins in Chapter 1 with a brief introduction to plasmas. Some background is given on electrical breakdown in gases and glow discharge formation. This leads into a description of the hollow cathode effect which is the operating principle of microdischarges.

In Chapter 2, the two different configurations we have used to generate microplasmas, a planar microdischarge and a plasma microjet, are presented. The electrical and optical properties of these sources are discussed showing their potential for applications.

Chapters 3 and 4 contain materials applications of microdischarges in etching and deposition. In Chapter 3, we introduce the idea of maskless pattern transfer. In this technique, microdischarges serve as stencil masks to directly etch holes and patterns in silicon wafers. Issues related to pattern filling, etch conformity, and etch rate are discussed. In Chapter 4, plasma microjets are utilized to deposit thin films. Results are shown for

polycrystalline diamond, including characterization by electron microscopy and micro-Raman spectroscopy.

The generation of excimer emission from microdischarges in metal capillary tubes is presented in Chapter 5. This work was done in collaboration with Prof. Karl Schoenbach and Dr. Mohammed Moselhy at Old Dominion University (Norfolk, VA). Vacuum ultraviolet spectroscopy is employed to measure the excimer radiation from microdischarges. Results show that the on-axis excimer intensity can be amplified by plasma expansion in single and multiple tubes.

In Chapter 6, we demonstrate the ability of microdischarges to perform as short-residence time reactors for nanoparticle synthesis. This work was done in collaboration with Prof. Richard Flagan and Dean Holunga at Caltech. The synthesis route couples with aerosol instrumentation enabling on-line size classification of the particles. Silicon nanoparticles can be grown with diameters of 1 to 2 nm and collected as colloids that exhibit blue luminescence. The chapter includes aerosol measurements of particle mobility and optical characterization by photoluminescence.

Chapter 7 discusses future applications of microdischarges including gas conversion. Some preliminary experiments performed on ozone generation are presented.

Chapter 1

FROM GLOWS TO HOLLOW CATHODES: FORMATION OF AN ELECTRICAL DISCHARGE

1.1 Introduction to plasmas

The term "plasma" is used to describe a partially or completely ionized gas containing electrons, ions, and neutrals. Although there is always a small degree of ionization in any gas, a stricter definition of a plasma is "a quasi-neutral gas of charged and neutral particles which exhibits collective behavior" [1]. Quasi neutrality refers to the characteristic that the positive and negative space charges balance in a given volume such that overall, the plasma is considered to be electrically neutral. If local concentrations of charge arise, electrostatic forces created by the space charge imbalance act to restore charge neutrality. The collective behavior of a plasma is a result of Coulomb forces that are long-ranged and cause remote regions to interact with one another. These features are important in differentiating a plasma state from a neutral gas and other ionized gases.

A plasma is generally characterized by the number density [particles/cm^3] and average kinetic energy or temperature [eV] of the various charged species. For an electropositive plasma, the electron density, n_e, and ion density, n_i, are considered equal because of quasi neutrality, giving rise to the common charged particle density, n, known as the plasma density. The average temperature of electron, ions, and neutrals can vary

significantly depending on plasma conditions; in an electrically driven, weakly ionized gas, the electrons are preferentially heated and do not exchange energy with the rest of the gas. In that case, the average electron temperature, T_e, is much larger than the average ion temperature, T_i, and neutral gas temperature, T.

Many of the physical characteristics of plasmas can be understood in light of these parameters. In Fig. 1.1, different kinds of plasmas are classified on a log n versus log T_e plot. Two types of processing plasmas that are relevant to this thesis are low-pressure glow discharges and high-pressure arcs. Low-pressure glow discharges are operated between 1 and 1000 mTorr and characterized by T_e=1-10 eV, $T_e >> T_i > T$, and n=10^8-10^{13} cm^{-3}. High-pressure arc discharges are typically formed near atmospheric pressure and have T_e=0.1-2 eV and n=10^{14}-10^{19} cm^{-3}. Arcs are commonly referred to as "thermal" plasmas since they are closer to equilibrium with $T_e \geq T_i \approx T$. While the properties of these two discharges differ greatly, they both find applications in materials processing. Glow discharges are used as miniature "chemical factories" in which feedstock gases are electrically broken into ions and chemically reactive species to then modify a surface [2]. Arcs find applications in heating, melting, evaporation, and cutting of materials.

Microdischarges are a new class of plasmas whose properties fall somewhere between those of glow discharges and arcs. Like arcs, they operate at high pressures up to 1 atmosphere. The electron temperature and non-equilibrium characteristics of microdischarges, however, make them more similar to glow discharges. As a result, they are often referred to as "high-pressure glow discharges." In order to develop an understanding of how these discharges form, the following chapter discusses gas breakdown and the operating principle of microdischarges.

1.2 Electrical breakdown of gases

Formation of a gas discharge occurs when energetic electrons dissociate the gas through impact to create ions. T_e is generally less than the threshold energy required for ionization. Ionization processes are possible because electrons have a distribution of energies [2]. If we assume a Maxwellian distribution at the average electron temperature T_e, the electron energy distribution function will be of the form [2]:

$$g(\varepsilon) = \sqrt{\varepsilon}\ \ \exp\left(-\frac{\varepsilon}{T_e}\right) \tag{1.1}$$

where ε is the electron energy. From the graphical depiction of Eq. 1.1 in Fig. 1.2, the distribution shows a maximum corresponding to $T_e/2$ and a tail at higher energies. Electrons in the high-energy tail of the distribution are responsible for ionization processes that create and sustain the plasma. For non-Maxwellian plasmas, the tail of the distribution may be higher or lower than that shown in Fig. 1.2 because of electron heating or collisional processes.

The simplest configuration employed for striking a gas discharge is a parallel electrode geometry schematically shown in Fig. 1.3. Two plane metal plates are separated by a distance, d, in a tube reactor filled with a particular gas at a pressure, p. Breakdown of the gas is achieved by applying a direct-current (dc) electric field with the cathode and anode biased negatively and positively, respectively. When the voltage between the plates is low, the gas is a near-perfect insulator. As the voltage is increased, a small fraction of electrons present in a gas are accelerated towards the anode making collisions with the background

atoms. Some of these collisions create positive ions which are then accelerated towards the cathode. When the ions strike the cathode, electrons are liberated from the metal surface as a result of neutralization (secondary electron emission). This process gives rise to an entire avalanche of electrons leading to gas breakdown and discharge formation. The voltage at which breakdown occurs is described by Paschen's law [3]:

$$V_b = \frac{Bpd}{\ln Apd - \ln\left[\ln(1+1/\gamma)\right]} \tag{1.2}$$

where A, B are gas-dependent parameter and γ is the Townsend secondary electron emission coefficient for the cathode. The constants A and B are related by the following equation:

$$\frac{\eta}{p} = A\exp\left(-\frac{Bp}{E}\right) \tag{1.3}$$

where η is the ionization coefficient for the gas and E is the electric field. A and B are normally determined experimentally and have been found to be relatively constant for a given gas over a range of fields and pressures (as confirmed by Eq. 1.3). Therefore, the breakdown voltage is found to depend only on the product *pd* for a given gas and cathode material. Plots of the breakdown voltage versus *pd* are known as Paschen curves and an example is shown in Fig. 1.4. A characteristic minimum in the function appears at some intermediate value of *pd*. At low *pd* values, the breakdown voltage is high because of too few collisions (low pressure or small gap). At high *pd* values, the breakdown voltage is high because of too many collisions (high pressure or large gap). It should be noted that Paschen

curves for different gases or cathode materials will have roughly the same shape but will be shifted from one another.

1.3 The glow discharge

When breakdown occurs, the gas suddenly becomes conductive Current is limited through the discharge by using an external ballast resistor. Changes in the power supply voltage will cause the current and voltage in the discharge to vary. These parameters can be measured to obtain a current-voltage (I-V) characteristic for a glow discharge as illustrated in Fig. 1.5. At low currents, the discharge is weakly ionized, characterized by high voltages and large resistance, and is referred to as a Townsend discharge. Increasing the current will result in a decrease in voltage until a minimum is reached, known as the sustaining voltage. This region is the so-called normal glow where the discharge voltage remains relatively constant for varying currents. In this segment of the I-V curve, changes in the discharge current do not alter the current density; only the area over which the current flows is varied. When the cathode is completely covered by the discharge, the current is increased by increasing the voltage which acts to supply more electrons to the discharge. The positively sloped section of the I-V curve is the abnormal mode of the discharge. Further increase in the current will result in a sudden drop in voltage and transition of the discharge to an arc which is characterized by low voltages (~10 V) and high currents (~ 1 A).

The normal glow discharge, unlike the Townsend or arc discharge, is characterized by distinct regions with large variations in the electric field [4, 5]. The approximate appearance of the different luminous regions is shown in Fig. 1.6(a). Also shown for

reference is the associated potential distribution between the cathode and anode in Fig. 1.6(b). In the main luminous region of the glow discharge, termed the "positive column," the electric field remains relatively constant. The term "plasma" applies to this region only where the electric field is uniform. The largest drop in voltage occurs near the cathode across the Ashton dark space, cathode glow, and cathode dark space. These fine-structured regions make up what is known as Crooke's dark space which is commonly referred to as the cathode fall or sheath. Here, the electrons from the positive column are prevented from reaching the cathode. As described earlier, ions are accelerated in the sheath region to high energies and produce secondary electrons by impacting the cathode. It is these electrons which supply the current to maintain the discharge. The potential gradient between the cathode and the positive column causes electrons to then accelerate through the sheath into a region called the negative glow. Unlike the positive column where electron energies are near the average electron temperature, the negative glow has been found to contain electrons in the high-energy tail of the Maxwellian distribution (>10 eV). Before reaching the positive column, the electrons lose their energy through more collisions in the Faraday dark space. A thin sheath also exists near the anode with a similar structure to the cathode fall made-up of the anode glow and anode dark space. The voltage drop in this region is significantly smaller than near the cathode and plays little role in the discharge dynamics.

The thicknesses of the various regions of the glow discharge depend on the gas, pressure, distance between electrodes, electrode materials, and discharge current. Similar to the Paschen law for breakdown, the thicknesses of the regions have been calculated as a function of the product *pd*. For example, the cathode fall thickness for plane cathodes has been determined to approximate the following [6]:

$$pd_{cathode} = B^* + \frac{pB}{J^{1/2}} \quad (1.4)$$

where p is the pressure, d is the cathode fall thickness, B^* and B are parameters depending on gas and cathode material, and J is the current density. Some typical values for the cathode fall thickness are also given in the following table:

Table 1.1. Normal cathode fall thicknesses in *pd* (Torr-cm) [7].

Gas Cathode	Air	Ar	H_2	He	Hg	N_2	Ne	O_2
Al	0.25	0.29	0.72	1.32	0.33	0.31	0.64	0.24
C			0.90		0.69			
Cu	0.23		0.80		0.60			
Fe	0.52	0.33	0.90	1.30	0.34	0.42	0.72	0.31
Mg			0.61	1.45		0.35		0.25
Hg			0.90					
Ni			0.90					
Pb			0.84					
Pt			1.00					
Zn			0.80					

1.4 The hollow cathode effect

The most important physics in a dc glow discharge occurs near the cathode electrode. In this region, there are large voltage drops (cathode fall) and energetic electrons (negative glow) that are necessary to sustain the discharge. Although a simple explanation

for the mechanism of gas breakdown and discharge formation has been given in Sections 1.2 and 1.3, the various processes in the cathode fall and negative glow are more complex. The earliest studies to probe these regions observed that modification of the cathode shape would cause the discharge current to rise by several orders of magnitude. This is now known as the hollow cathode effect.

In the original experiments by Paschen in 1916 [8], a pair of parallel plates was used as the cathode [Fig. 1.7(a)]. He found that reducing their separation caused a rise in the current density with no concomitant increase in the discharge voltage. As previously discussed, this is counter to a glow discharge where an increase in the current density is characterized by an increase in voltage when the discharge becomes abnormal. In this case, ionization processes are increased without a change in the cathode sheath potential! To explain this result, it was surmised that the hollow cathode effect was caused by interactions between the dark spaces of opposing cathodes. Simply, when the cathode plates were too far, there was no interaction between the cathode falls. In 1923, Güntherschulze [9], suggested that electrons could be trapped in the cathode and through increased ionization events cause the observed current enhancement.

Although the hollow cathode discharge has been used in applications such as spectroscopy since these early studies, it was not until the 1950s that a theory for the effect was developed [10, 11]. When the separation between the cathodes is reduced sufficiently, a potential well is formed by the plasma which is near anode potential as depicted in Fig. 1.7(b). This leads to an oscillatory motion of electrons between opposite cathode fall regions known as the Pendel effect [9]. The motion of electrons in the cathode causes a drastic increase in the number of ionization events. In addition, the hollow cathode geometry has multiple effects on the discharge characteristics [12]:

1) increase in ion density and radiation from highly excited states in the negative glow;
2) enhanced secondary electron emission from the cathode from ions, photons, and metastable excited atoms;
3) trapping of fast electrons which are lost otherwise; and
4) increase in the field gradient which increases electron and ion velocity.

A combination of these events is believed to result in many of the interesting properties in a hollow cathode discharge. The physical geometry is critical to ensure the collection of electrons, ions, and metastable atoms at the cathode. Structures including parallel plates, hollow cylinders, and spherical cavities are used as cathodes for this purpose. Also necessary is scaling of the physical dimension of the cathode to allow interaction between the opposing cathodes. It is the overlap of the negative glow regions that leads to intense ionization in the hollow cathode [13]. As described earlier, electrons emitted from the cathode surface are accelerated in the cathode fall and undergo collisions in the negative glow. By trapping these high-energy electrons in the negative glow, collisional excitation and ionization is greatly amplified as compared to a conventional glow discharge.

From this description, a condition for hollow cathode operation can be obtained. We know from Eq. 1.4 that the thickness of the cathode fall depends on pressure and other discharge properties. The cathode gap required for operation in the hollow cathode mode is, therefore, calculated to be the sum of the lengths of two cathode falls and the negative glow [14]:

$$pd_{cathode} = 2B^{*} + \frac{2pB}{J^{1/2}} + l_o p_o \tag{1.5}$$

where p=pressure, $d_{cathode}$=cathode gap, and l_o is an estimation for the negative glow thickness at pressure, p_o. In Eq. 1.5, the thicknesses of the regions have been estimated from experiments on dc glow discharges with a plane cathode. The inverse dependence of the cathode gap separation on pressure that is suggested by Eq. 1.5 has been observed experimentally [9-14]. To produce the hollow cathode effect in rare gases such as argon, the product of the cathode gap and pressure must be of order 10 Torr-cm [10].

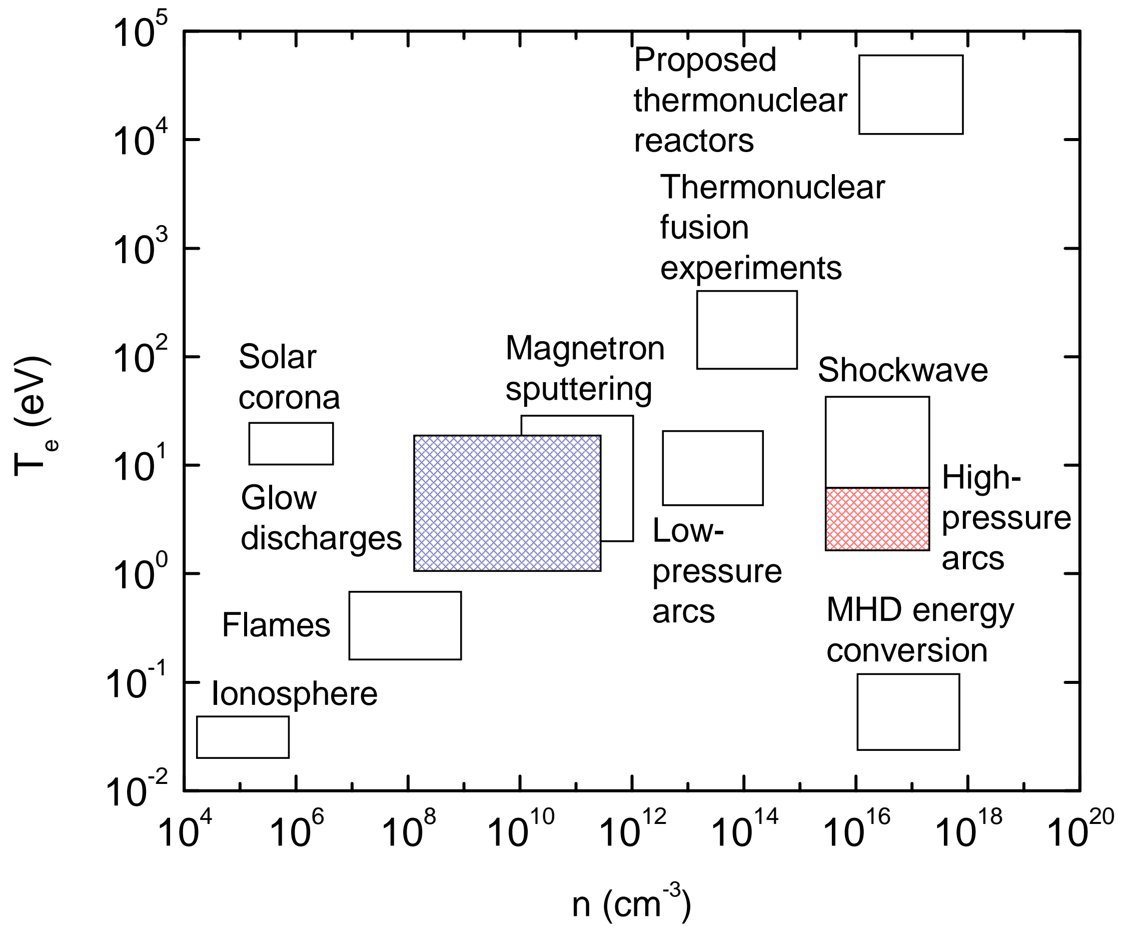

Figure 1.1. Space and laboratory plasmas classified by their electron temperature, T_e, and charged particle density, n. Reproduced from Ref. 2.

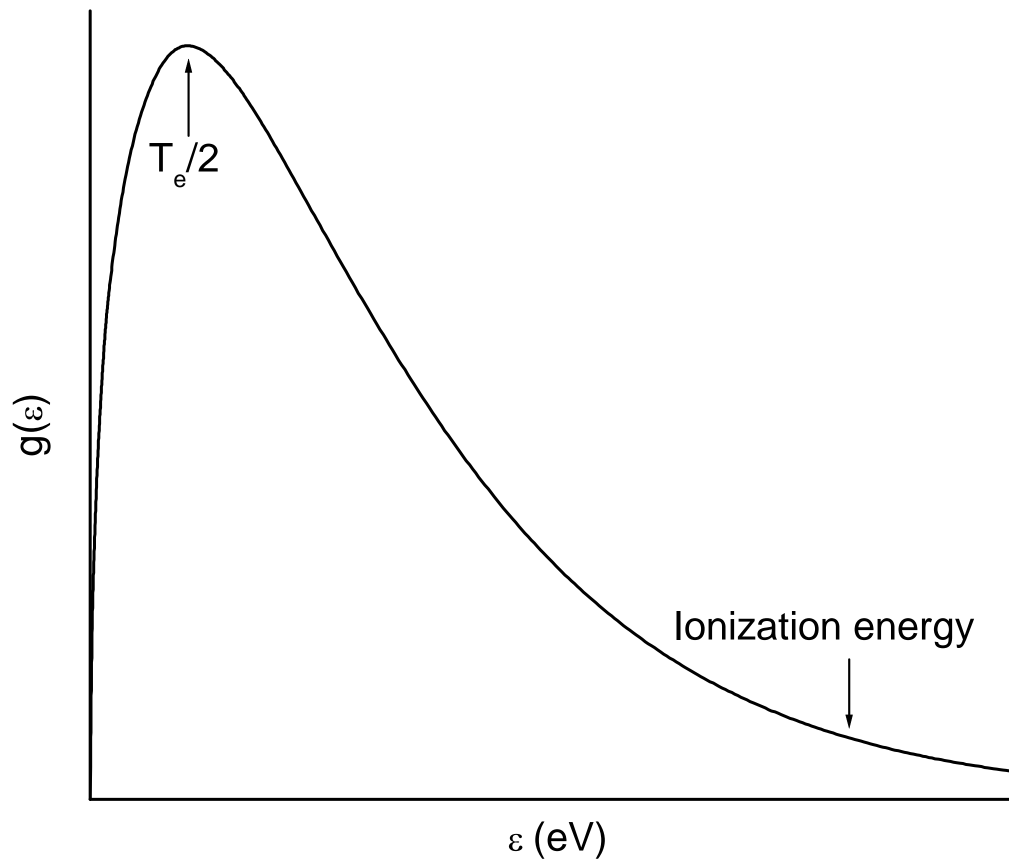

Figure 1.2. Electron energy distribution function (EEDF) in a weakly ionized gas assuming a Maxwellian distribution at the average electron temperature T_e.

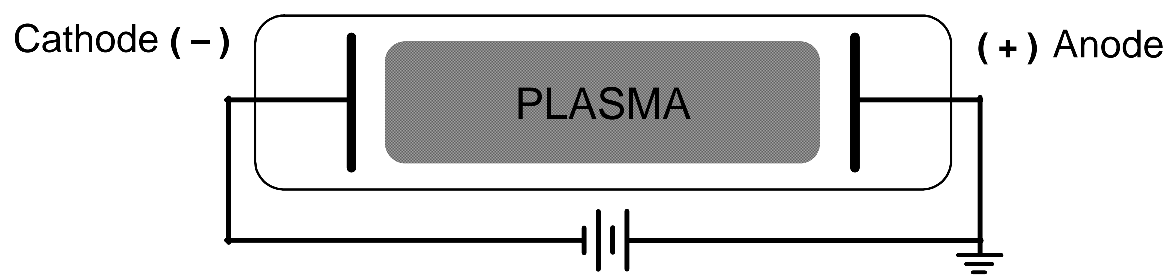

Figure 1.3. Plane parallel electrode reactor for producing a dc glow discharge.

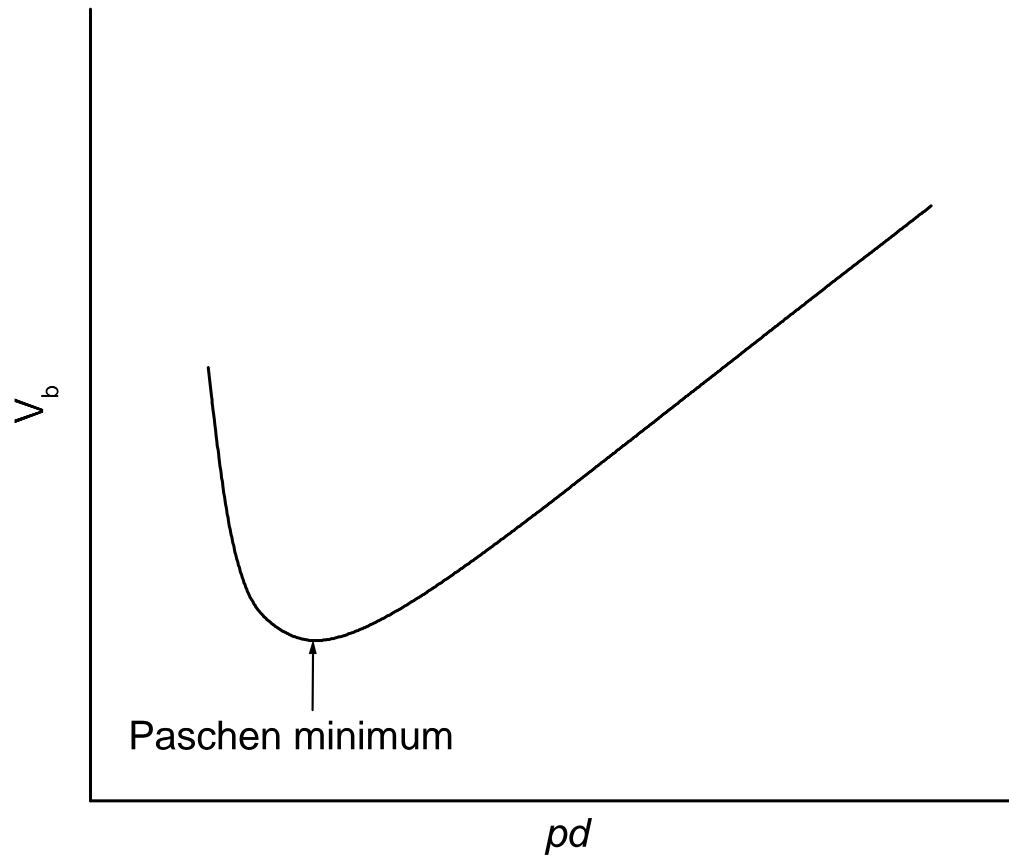

Figure 1.4. Paschen curve for arbitrary gas in a plane parallel electrode discharge. V_b is the breakdown voltage and *pd* is the product of the pressure and distance between electrodes.

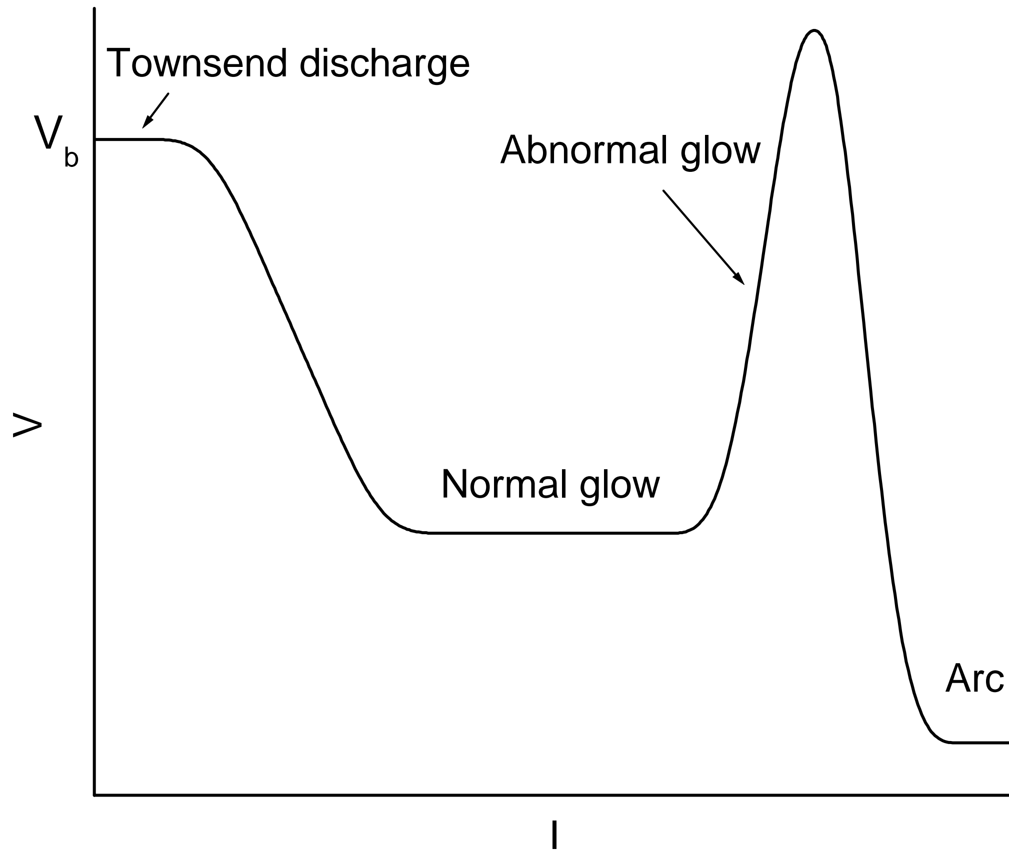

Figure 1.5. Current-voltage (I-V) characteristic of a dc glow discharge. V_b refers to breakdown voltage of the gas.

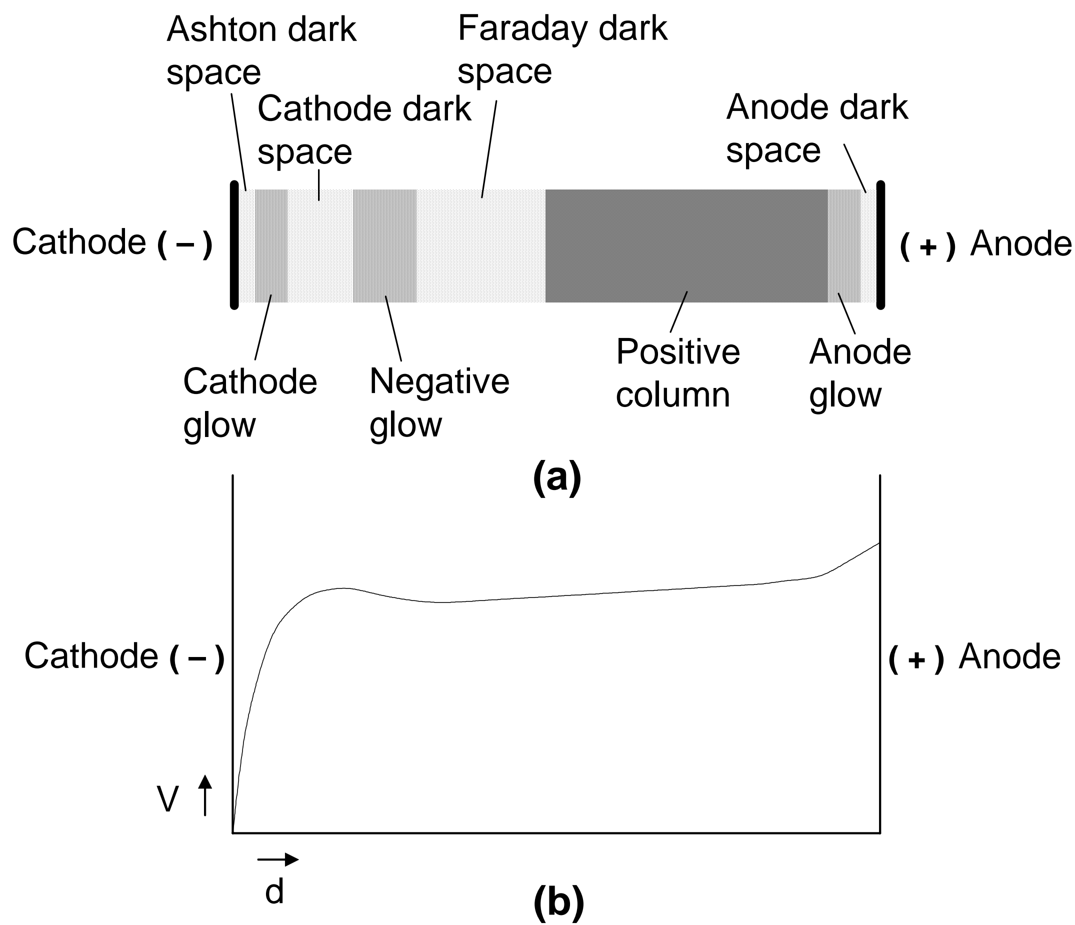

Figure 1.6. Regions of a dc glow discharge showing (a) qualitative characterisitics and (b) potential distribution.

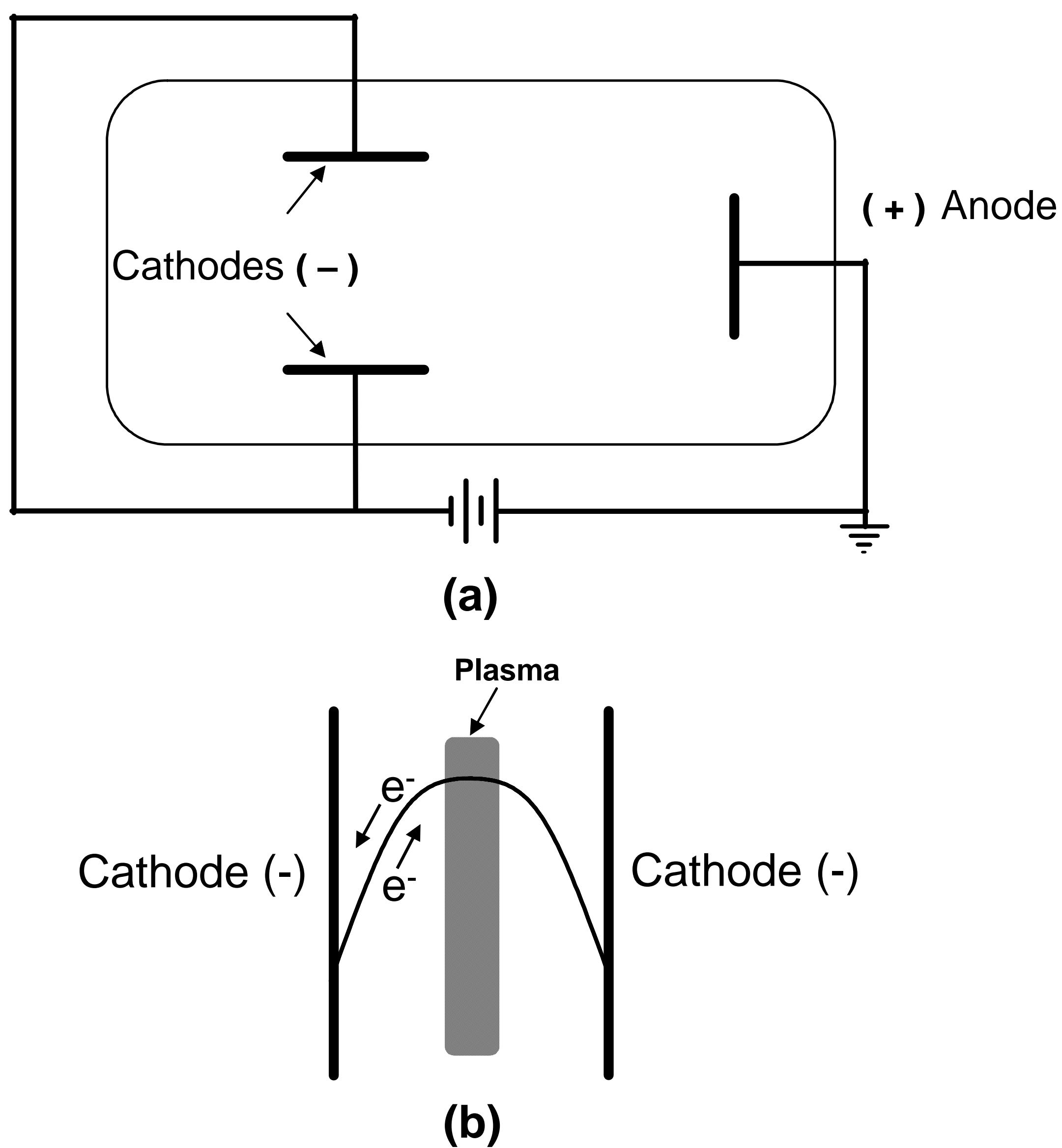

Figure 1.7. Hollow cathode discharge showing (a) setup with two plane parallel metal plates as the cathode and (b) potential well for oscillation of electrons.

Chapter 2

ATMOSPHERIC-PRESSURE MICRODISCHARGES[1]

2.1 Introduction

Hollow cathode discharges are gas discharges between a cathode with a hole and an anode of arbitrary shape. As discussed in Chapter 1, compared to a conventional glow discharge between parallel plates, the hollow cathode geometry is characterized by higher current densities and larger concentrations of high-energy electrons. These properties are preserved even at high pressures simply by scaling the hollow cathode appropriately. In one version developed by Schoenbach in 1996 termed "microhollow cathode discharge" [14], direct current (dc) discharges are struck in a hole between two metal foils separated by a dielectric spacer. Reducing the hole diameter down to about 100 μm allows operation at atmospheric pressure in a variety of rare gases including argon [14], neon [15], and xenon [16]. For applications that require gas flow, we have extended this concept to a metal capillary tube cathode, resulting in the formation of a plasma microjet [17, 18]. In this configuration, the dielectric is eliminated which extends the discharge lifetime significantly. In this chapter, the electrical and optical properties of both the planar microdischarges and the plasma microjets will be presented.

---

[1] Material in this chapter adapted from: R. M. Sankaran and K. P. Giapis, J. Appl. Phys. **92**, 2406 (2002).

2.2 Microdischarge setup

A typical setup for forming planar microdischarges is schematically shown in Fig. 2.1(a). The structure consists of two thin metal layers surrounding a dielectric with each layer being approximately 100 μm in thickness. Examples of materials used as the metal include molybdenum, stainless steel, aluminum, and copper. For the dielectric, materials such as mica, alumina, and polymeric films including Teflon or Kapton (polyimide) are normally chosen. A cylindrical hole between 100 and 500 μm in diameter is drilled through all 3 layers. Alternative versions of microhollow cathode geometries are also illustrated in Figs. 2.1(b)-(d). In each of these designs, the shape of the cathode always contains a circular opening. In contrast, the shape of the anode varies since it is not critical to the underlying physics of discharge operation.

Our studies of planar microdischarges were performed on copper-polyimide-copper devices with geometry and electrical connections consistent with Fig. 2.1(a). Structures were fabricated by spin-coating a 5-20 μm thick polyimide film on an oxygen-free copper foil (100 μm thick, 99.995% purity) [15]. Holes were mechanically drilled to a diameter of 200 μm. Finished devices were placed in a vacuum chamber and initially pumped to 1×10^{-4} Torr before backfilling with argon. To vary the background pressure, the gas flow rate was maintained with a mass flow controller and an automatic "butterfly" valve was used in the exhaust line between the chamber and pump. Discharges were ignited using a Spellman negative dc power supply (0-5 kV, 100 W) connected in series with a 100 kΩ current-limiting resistor (R_{CL}). The discharge current and voltage were measured by a 1 kΩ resistor (R_D) in series and a voltage probe in parallel, respectively.

The two important parameters in the microdischarge setup are the dielectric thickness and hole size. The dielectric acts as a spacer between the electrodes and sets the gap. According to the Paschen law (Eq. 1.2), the distance between the electrodes will affect the breakdown voltage. To reduce the required breakdown voltage, the discharge should be operated at a *pd* value near the Paschen minimum for the particular gas. The function of the hole in the microdischarge structure is to provide a hollow cathode geometry for discharge formation. As inferred from Eq. 1.5, the hole size ($d_{cathode}$) depends inversely on pressure. If we use the scaling constant of 10 Torr-cm, the hole diameter needed to obtain atmospheric operation in rare gases in the hollow cathode mode is found to be approximately 130 μm. Experimentally, this value has been determined to be closer to 250 μm [19].

A preferred geometry for using microdischarges as microreactors is one where flow of gas can be incorporated. This is accomplished by extending the operating principles of planar microdischarges to a tube electrode which serves as both the gas inlet and cathode. Previous studies have employed larger diameter tubes (0.5-2 mm) to sustain hollow cathode discharges consistent with operation at much lower pressures [20-22]. To ensure atmospheric operation, the tube hole size must be reduced to less than 250 μm in diameter as in the case of planar microdischarges. The setup for striking atmospheric microdischarges in a flow geometry is illustrated in Fig. 2.2. In this arrangement, a plasma microjet is formed between a stainless steel capillary tube with an internal diameter of 180 μm and a grid operated as the cathode and anode, respectively. The discharges were operated similar to a planar microdischarge with a dc power supply. One major difference, however, is the elimination of the dielectric between the cathode and anode. In addition to improving the stability of the source, this allows the distance between the electrodes, indicated as L in Fig.

2.2, to be varied to extend the physical length of the plasma. An additional parameter introduced is the gas flow rate which has important effects on the discharge characteristics.

2.3 Electrical characteristics

2.3.1 Planar microdischarges

The current-voltage (I-V) characteristics of a discharge can give valuable information about its mechanism as described for the case of glow discharges in Section 1.3. To obtain I-V curves, the discharge was first ignited by providing an overpotential of up to 1 kV with the dc power supply. The power supply voltage was then adjusted to vary the discharge current. I-V traces obtained between 50 and 760 Torr for a single planar Ar microdischarge are shown in Fig. 2.3. A comparison with the I-V curve for low-pressure glow discharges (Fig. 1.5) indicates that the Townsend mode and initial fall in voltage (negative resistivity) are absent. These regions of the I-V curve are observable at pressures lower than 50 Torr [14]. At higher pressures, breakdown is rapidly followed by a transition to the normal glow discharge mode where the discharge voltage is relatively constant. When the pressure is increased, the average sustaining voltage is found to decrease from approximately 250 V at 50 Torr to 205 V at 760 Torr. The effective plasma resistance, R_{eff}, can be estimated at the various pressures by finding the slope of the I-V plots. From this calculation, R_{eff} is found to decrease from 17.1 kΩ at 50 Torr to 12.7 kΩ at 760 Torr. Evidently, as the pressure is raised, the discharge becomes more conductive.

While single hole devices are convenient for experimental study, applications of microdischarges require the formation of arrays. For example, arrays of planar

microdischarges operated simultaneously would be attractive as a flat panel light source [15]. As we will discuss in Chapter 3, microdischarge arrays are also desirable for patterning of substrates. We have investigated the feasibility of arrays by fabricating copper-polyimide-copper devices with multiple holes. The I-V characteristic for a structure with 10 holes, each 200 μm in diameter, is shown in Fig. 2.4. At low currents, discharges form uniformly in all the holes. Continuing to increase the voltage results in a sharp transition from the high voltage, low current mode to a low voltage, high current mode. In this region of the I-V curve, only a single microdischarge is formed. The characteristics of the single discharge appear to be consistent with that of a hollow cathode. The limitation of parallel operation of microdischarges is reflected by this result. At low currents, the plasma resistance is high (850 kΩ) allowing multiple discharges to be maintained. When the voltage drop occurs, the resistance in one of the microdischarges decreases rapidly and the current flows through only this single, low resistance path. Since the hollow cathode effect is a high current, low resistance mode, operation in parallel requires resistive ballasting and, therefore, isolation of the individual discharges [23].

2.3.2 Plasma microjets

Experiments on plasma microjets (see Fig. 2.2) were performed with gas flow in ambient air. Unlike planar microdischarges, coupling of gas flow directly to the electrodes allows discharges to be sustained stably in open air. Properties of the plasma microjet were studied as a function of the following parameters: plasma current and voltage, cathode-anode separation (L), and gas flow rate. I-V traces of an atmospheric-pressure Ar microjet

flowing in air are shown in Fig. 2.5 for various values of L. The data was obtained by inducing gas breakdown with the gap as small as possible (<0.5 mm), then moving the anode to extend the discharge. This allowed the voltage required for breakdown to be less than 1 kV. The I-V characteristics were reproducible and showed a weak voltage dependence over the current ranges measured similar to the planar microdischarges in Fig. 2.3. In this case, we were able to extend the current to much higher values because of the lack of a dielectric. At a gap of 0.5 mm, the discharge is stable at currents and voltages as low as 2 mA and 260 V, respectively. Sustaining the discharge at lower currents is possible if the gap is decreased further. When the gap is enlarged, the plasma voltage increases as shown more clearly in Fig. 2.6. The dependence is nonlinear at short gap distances but becomes linear at larger gaps. This is representative of an increase in the length of the positive column in the discharge where the electric field remains constant (see Fig. 1.6).

The influence of the flow rate on plasma voltage at various cathode-anode gaps is illustrated in Fig. 2.6. A strong dependence of the plasma voltage on Ar flow rate was found for the experiments in ambient air at 760 Torr. The voltage required to sustain an Ar plasma microjet over a given gap size decreases significantly with the Ar flow rate. At a gap of 3 mm, for instance, the voltage can be reduced from 625 V to 408 V when the flow rate is increased from 50 to 200 sccm, respectively. The maximum distance that the Ar plasma microjet could be extended, however, decreased from 5 to 3 mm for the same flow rate change. Beyond the distances shown in Fig. 2.6 for each flow rate, the Ar plasma microjet extinguished. The behavior was significantly different from that observed for an Ar plasma microjet formed in ambient argon at 760 Torr. In the latter case, the plasma voltage was much lower over the range of gap sizes and exhibited no dependence on the Ar flow rate. The microjet could also be extended over much larger gaps as compared to the experiments

in air. From these observations, it appears that the effect of flow rate on plasma voltage may be related to the diffusion and mixing of air into the argon stream. A higher flow rate could reduce the mixing of air into the argon stream, particularly near the tube exit orifice. A reduction in the plasma voltage ensues then, as a consequence of the lower electric field requirement to sustain a discharge in argon with less air contamination [4]. With increasing flow rate, however, the exit pressure and flow velocity become larger which could cause turbulence. Turbulence could cause significant mixing with air at some distance from the exit of the tube [24] thereby causing the discharge to extinguish at increased gaps. It should be noted that plasma microjets could not be formed when flowing air at atmospheric pressure using the 180 μm diameter tube but operation at lower pressures was possible. The suggestion that mixing of ambient air into the argon stream is responsible for the observed flow rate dependence should be taken with caution as heating effects and plasma instabilities further complicate the picture.

Since the I-V traces do not show any positive resistivity, parallel operation of plasma microjets requires ballasting of individual discharges. Although difficult for the case of planar microdischage arrays, the tube geometry is convenient in allowing individual discharges to be electrically isolated as depicted schematically in Fig. 2.7(a). The ballast resistor, R_b, must be identical in value to ensure that the current is the same in each discharge. This setup has been applied to parallel operation of four Ar plasma microjets, as shown in Fig. 2.7(b); the scheme can be easily expanded to larger arrays of tubes. When running plasma microjet arrays, the sustaining voltage was found to be the same as for a single microjet while the total current increased by a factor equal to the number of tubes. All plasma microjets in the array ignited simultaneously and each discharge behaved similarly to a single plasma microjet.

The current and voltage ranges for operation of planar microdischarges and plasma microjets are very similar. It is instructive to compare their properties to that of another high-pressure plasma source, the arc. With large gas temperatures as high as tens of thousands of Kelvin, the mechanism for arc discharge operation is thermionic emission of electrons at the electrode surfaces [4]. For this reason, arcs are characterized by higher currents (> 1 A) and lower voltages (< 100 V). The I-V characteristics of microdischarges are more similar to those of low-pressure glow discharges. As in the case of glows, the discharge voltages suggest secondary electron emission at the cathode. The importance of the microhollow cathode geometry is to enhance these processes and allow high-pressure operation.

2.4 Optical characteristics

2.4.1 Planar microdischarges

Excited neutral and ionic states in a plasma can decay to lower energy states by photon emission. For atomic gases, the radiation is emitted by transition between electronic levels of the same electronic states. Optical emission spectroscopy is employed to identify these states by their spectral radiation to gain insight about the properties of the discharge. This technique offers non-intrusive characterization of the microdischarges. To collect radiation from microdischarges, a setup consisting of standard optics, a 0.22 m SPEX 1680 double monochromator (gratings ruled with 1200 grooves/mm, blazed at 630 nm) and a Hamamatsu R928 photomultiplier tube was used. Figure 2.8 shows emission spectra as a function of pressure for a copper-polyimide-copper microdischarge in argon. Lines

corresponding to both excited Ar neutrals and Ar ions are present in the spectra. The highest excited states in the discharge are ion lines indicated by an asterisk. These lines are listed in the following table with their corresponding energy:

Table 2.1. Argon ion lines and corresponding energies (above ground state).

Wavelength (nm)	Energy (eV)
410.4	22.51
413.2	21.43
437.1	19.26
438.0	19.64
440.1	19.22
442.6	19.55
454.5	19.87
457.9	19.97
459.0	21.13
461.0	21.14
465.8	19.80
472.7	19.76
473.6	19.26
476.5	19.87
480.6	19.22
484.8	19.30
488.0	19.68
493.3	19.26
496.5	19.76

The presence of these lines in the spectra indicates that the discharge contains a significant population of electrons with energies between 19 and 22 eV. These electrons are not necessarily at the average temperature of the electron energy distribution function (Eq. 1.1). Energetic electrons are normally attributed to the tail of the function. The spectral

characteristics of the microdischarge suggest that its electron energy distribution contains an extended high-energy tail. This is expected since the hollow cathode geometry is known to cause deviations from a Maxwellian distribution [25].

As the pressure is increased from 50 to 200 Torr, the intensity of the ion lines decreases. This reflects the effect of collisional quenching which reduces electron energies at higher pressures. However, the presence of ion lines at pressures up to 200 Torr is still significant in comparison to other high-pressure sources [23]. Production of relatively large concentrations of high-energy electrons at high pressures is possible because of the hollow cathode geometry.

2.4.2 Plasma microjets

Emission spectra have also been collected for plasma microjets at atmospheric pressure. In Fig. 2.9, spectra of Ar plasma microjets formed in two different hole sizes are shown. Although most of the spectrum is composed of Ar neutral lines (415-435 nm) because of the high pressure, weaker intensity Ar ion lines appear in the spectrum from the plasma microjet formed in the smaller inner diameter tube (180 μm). For the larger hole size of 500 μm, these lines are absent from the spectrum. In addition to the difference in spectral radiation, plasma microjets formed in tubes with different holes sizes also vary in visual characteristics. Figure 2.10 compares the appearance of an Ar plasma microjet formed in 180 μm and 500 μm diameter tubes as seen through a concentric metal aperture 1 mm in diameter which serves as the anode. In the smaller diameter tube [Fig. 2.10(a)], the plasma forms in the center of the hole and stretches from the hole to the edge of the anode. The

discharge appears to form outside the boundary of the hole (shown by the dotted line) but this may be caused by plasma expansion outside the hole and/or overexposure. This picture should be contrasted with the discharge in the larger inner diameter tube (500 μm) shown in Fig. 2.10(b). The discharge does not fill the hole uniformly but appears to be localized near the inner surface of the tube.

The discharges formed in tubes with hole diameters of 180 μm are expected to operate in the hollow cathode mode at atmospheric pressure since their *pd* value (13.5 Torr-cm) is close to the upper limit of 10 Torr-cm experimentally determined for planar microdischarges. Comparison of the optical characteristics with a larger hole size confirm that the smaller hole size is necessary to ensure hollow cathode operation at the high pressures. As a result of the microhollow cathode geometry, both planar microdischarges and plasma microjets exhibit enhanced optical characteristics. This is similar to the properties of the hollow cathode discussed in Section 1.4 for lower pressures and larger scales. Our results demonstrate that by reducing the diameter of the hollow cathode, this optimum operating mode can be shifted towards higher pressures.

2.5 Summary

High-pressure operation up to 1 atmosphere has been achieved in planar and flow-stabilized microdischarges by reducing the dimensions of the hollow cathode. Discharges are remarkably stable with relatively constant voltages over a range of currents reflective of a normal glow discharge. Optical characterization indicates intense ionization which is consistent with operation in the hollow cathode mode. Resistive ballasting of individual

discharges permits arrays of microdischarges to be operated using a single power supply. The flow of gas associated with the formation of a microjet allows the length of plasma microjets to be extended to several millimeters by increasing the operating voltage. In the following chapters, we will present applications of both the planar microdischarges and plasma microjets that illustrate their versatility.

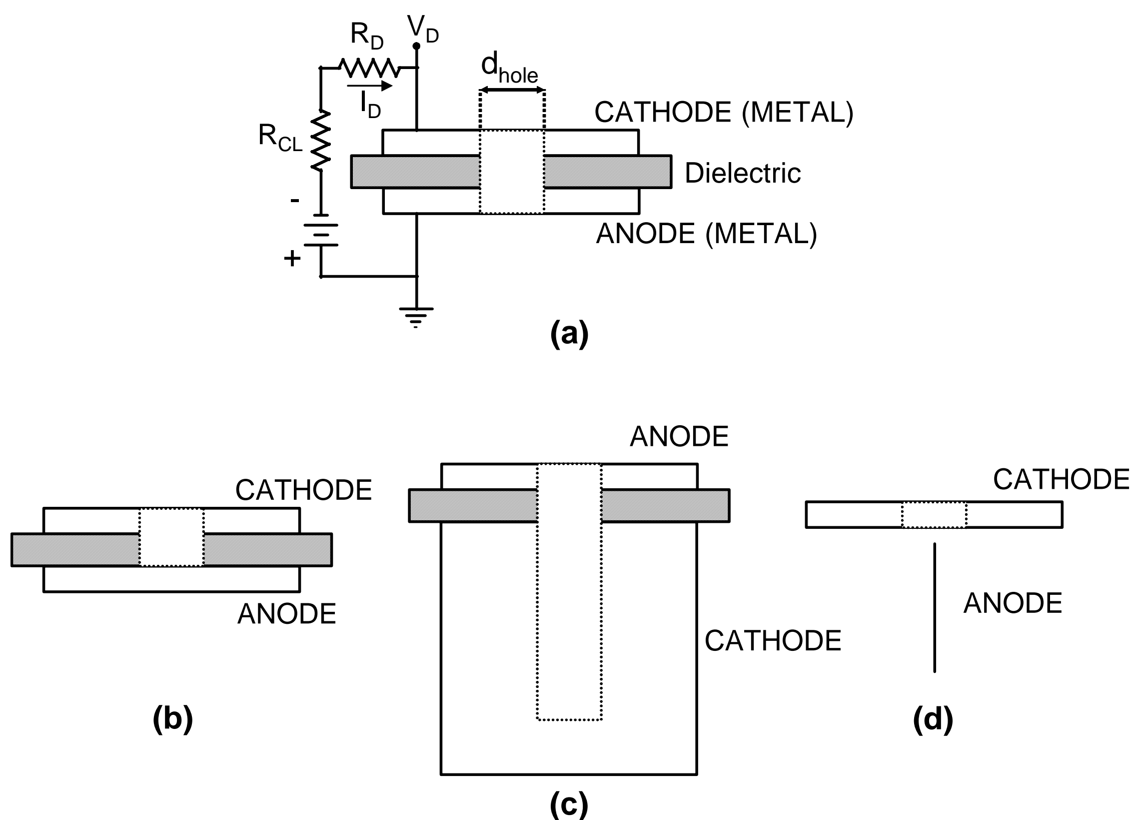

Figure 2.1. (a) Schematic of microhollow cathode discharge setup for typical 3-layer structure. Electrical connections are made using a dc power supply with two resistors in series, R_{CL}=100 kΩ and R_D=1 kΩ. V_D and I_D refer to measured discharge voltage and current, respectively. Alternative geometries are also shown including (b) a plane anode, (c) a cathode with a blind-hole, and (c) a wire anode.

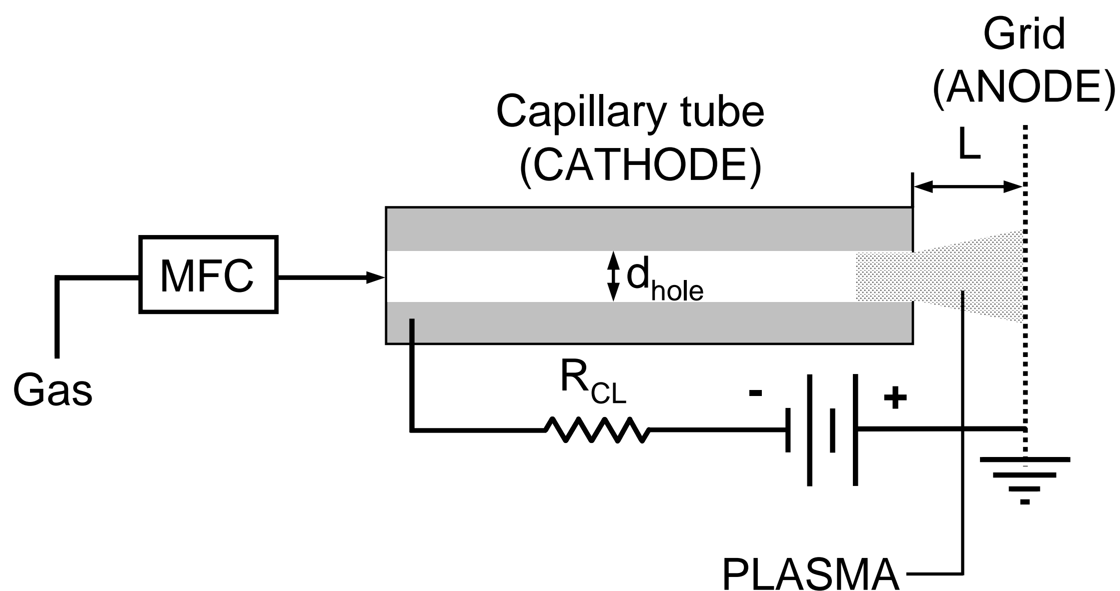

Figure 2.2. Schematic setup of plasma microjet operated between a metal capillary tube cathode (d_{hole}=180 μm) and a metal grid anode. The electrode gap distance, L, was varied during experiments with a micrometer. Gas flow rate was controlled by a mass flow controller (MFC). R_{CL} refers to current-limiting resistor (25 kΩ).

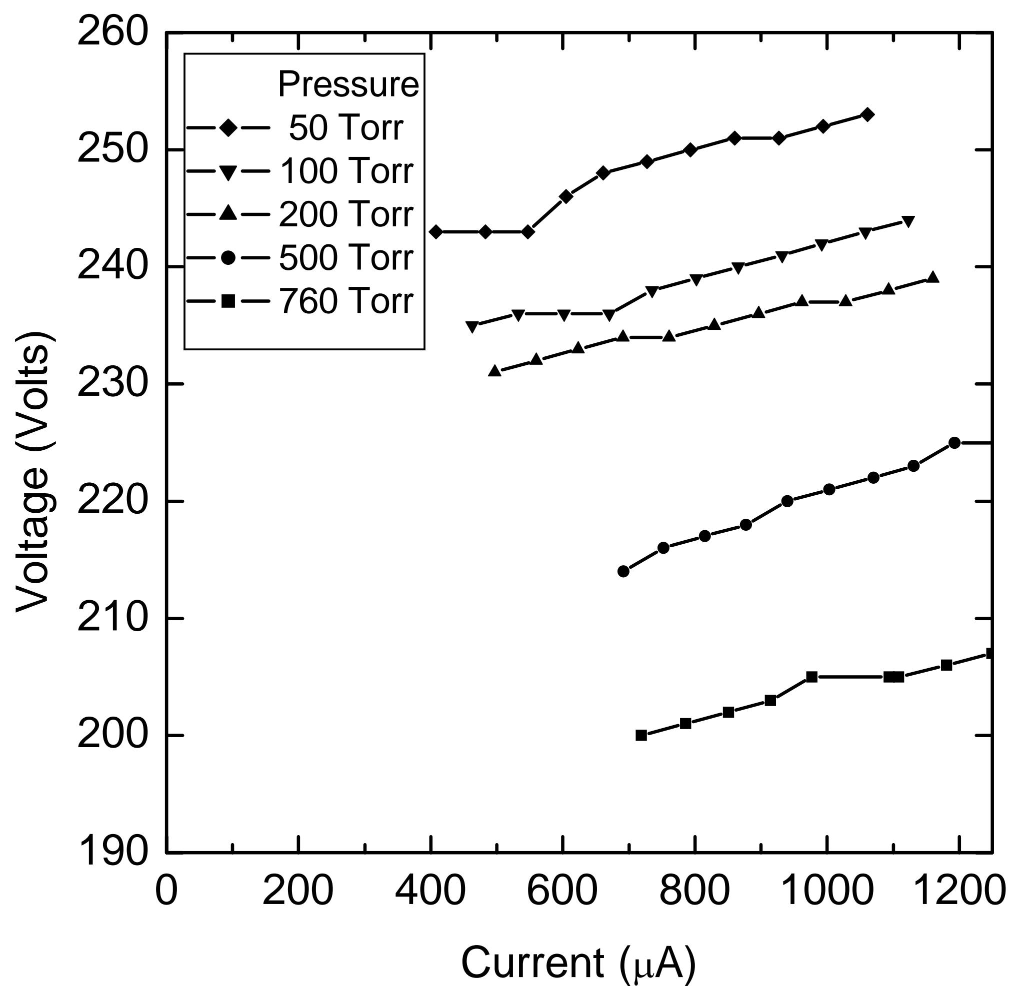

Figure 2.3. Current-voltage (I-V) characteristics of a single Ar microdischarge in a copper-polyimide-copper structure with 200 μm hole.

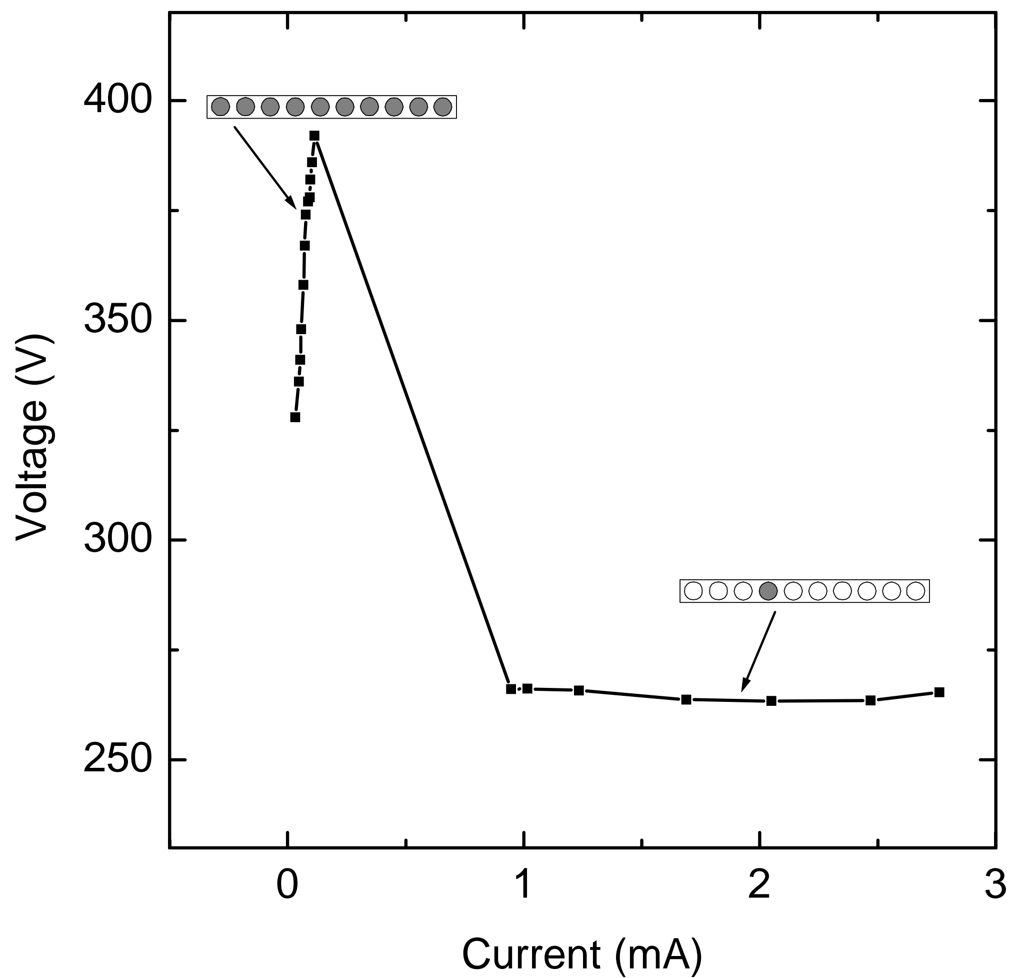

Figure 2.4. Current-voltage (I-V) characteristic of a microdischarge array with ten 200 μm diameter holes operated at 50 Torr. As indicated, at low currents the discharge exhibits positive resistivity and all the holes are filled. After the voltage drops, the discharge fills only a single hole at high currents.

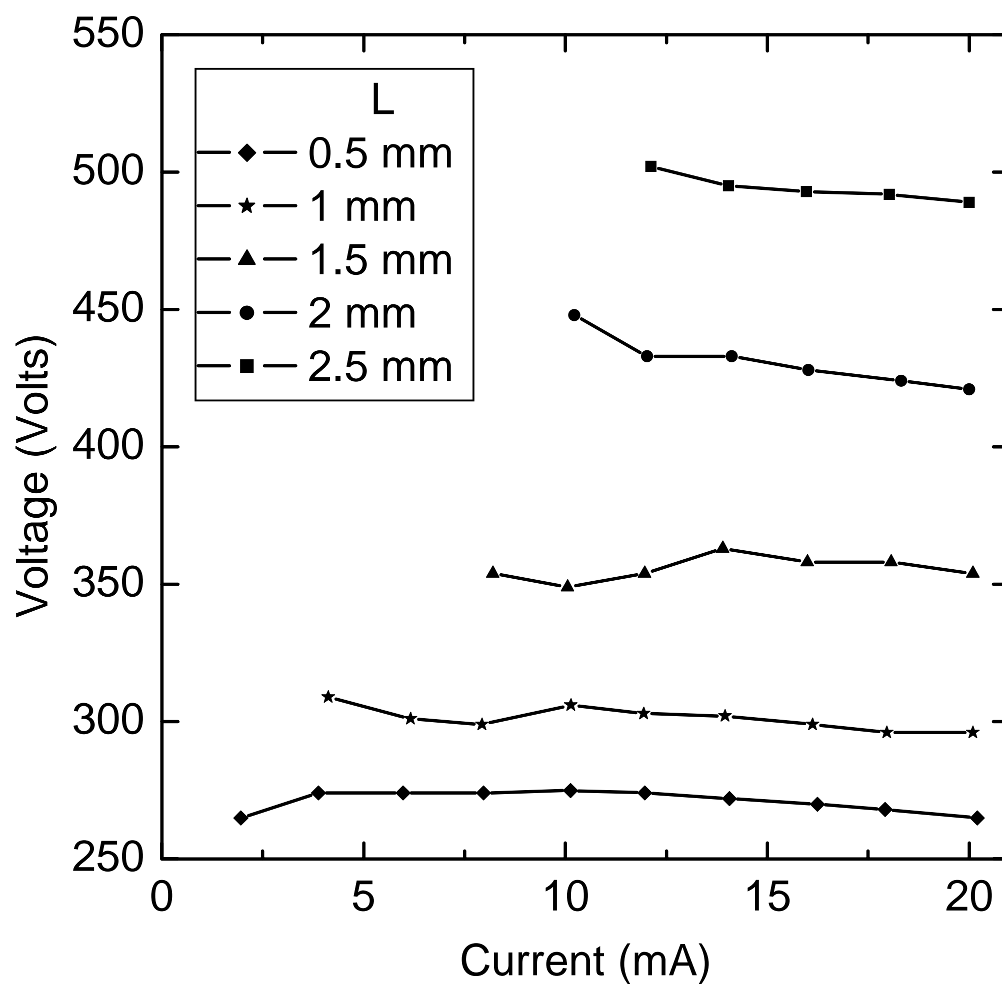

Figure 2.5. I-V characteristics of an Ar plasma microjet flowing in ambient air at 760 Torr at various cathode-anode gap separations (L). Argon flow rate through capillary tube (i.d.=180 μm) was 100 sccm.

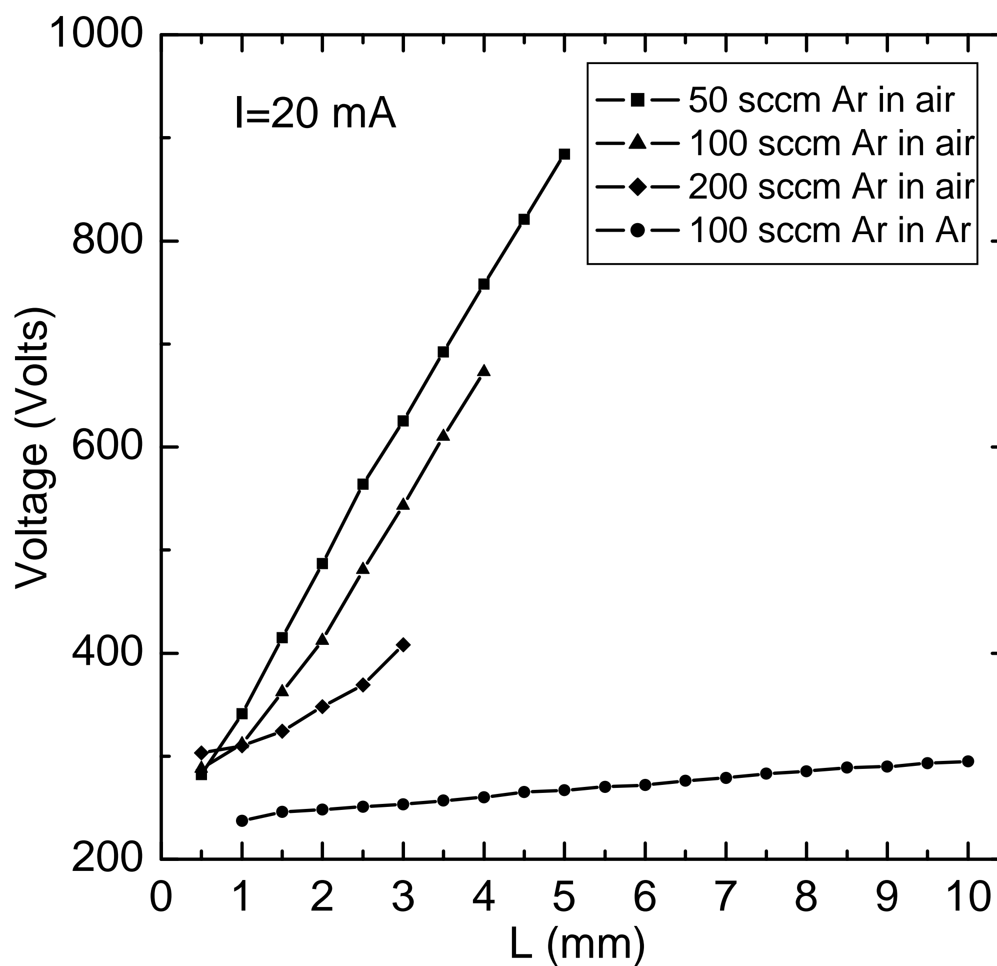

Figure 2.6. Plasma voltage as a function of cathode-anode gap (L) at various Ar flow rates for Ar plasma microjets flowing in ambient air or argon, as indicated. The flow rate is measured upstream from the capillary tube (i.d.=180 μm). The discharge current was fixed at 20 mA.

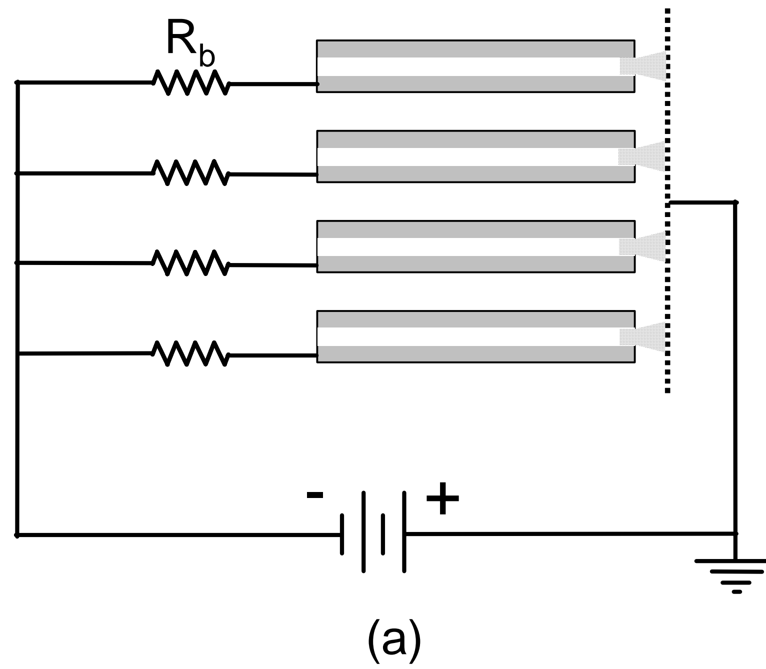

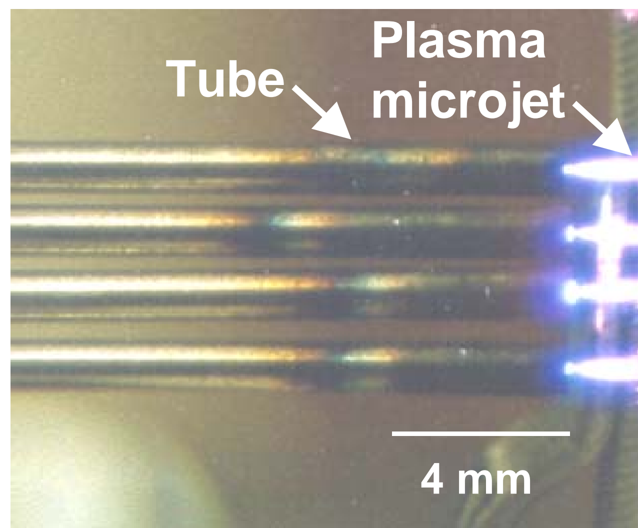

Figure 2.7. (a) Setup for parallel operation of four tubes using an identical ballast resistor, R_b=25 kΩ, for each tube and a single power supply. (b) A color photo of four Ar plasma microjets operating in ambient air at a cathode-anode gap of 2 mm.

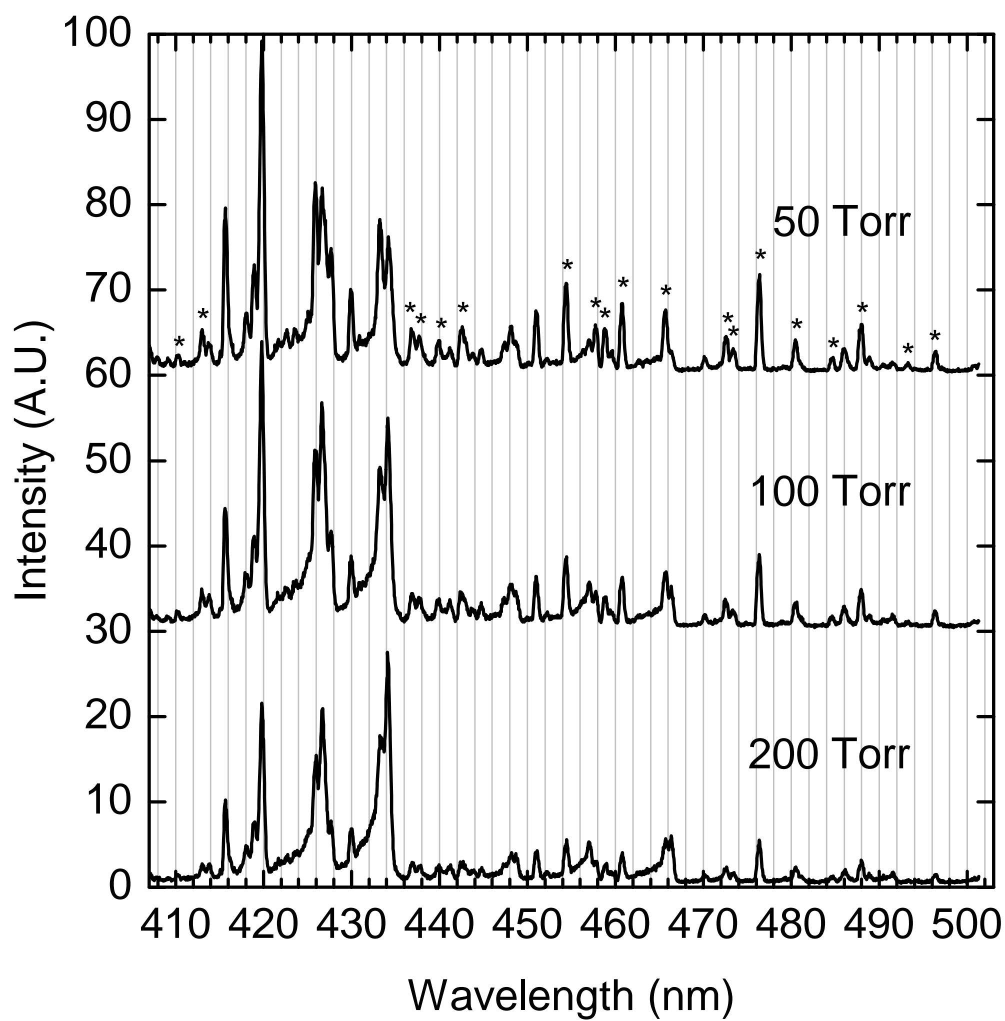

Figure 2.8. Emission spectra of Ar microdischarge in copper-polyimide-copper microdischarge with 200 μm hole. Discharge current was kept constant at 2 mA for each pressure. Argon ion lines are indicated by asterisk.

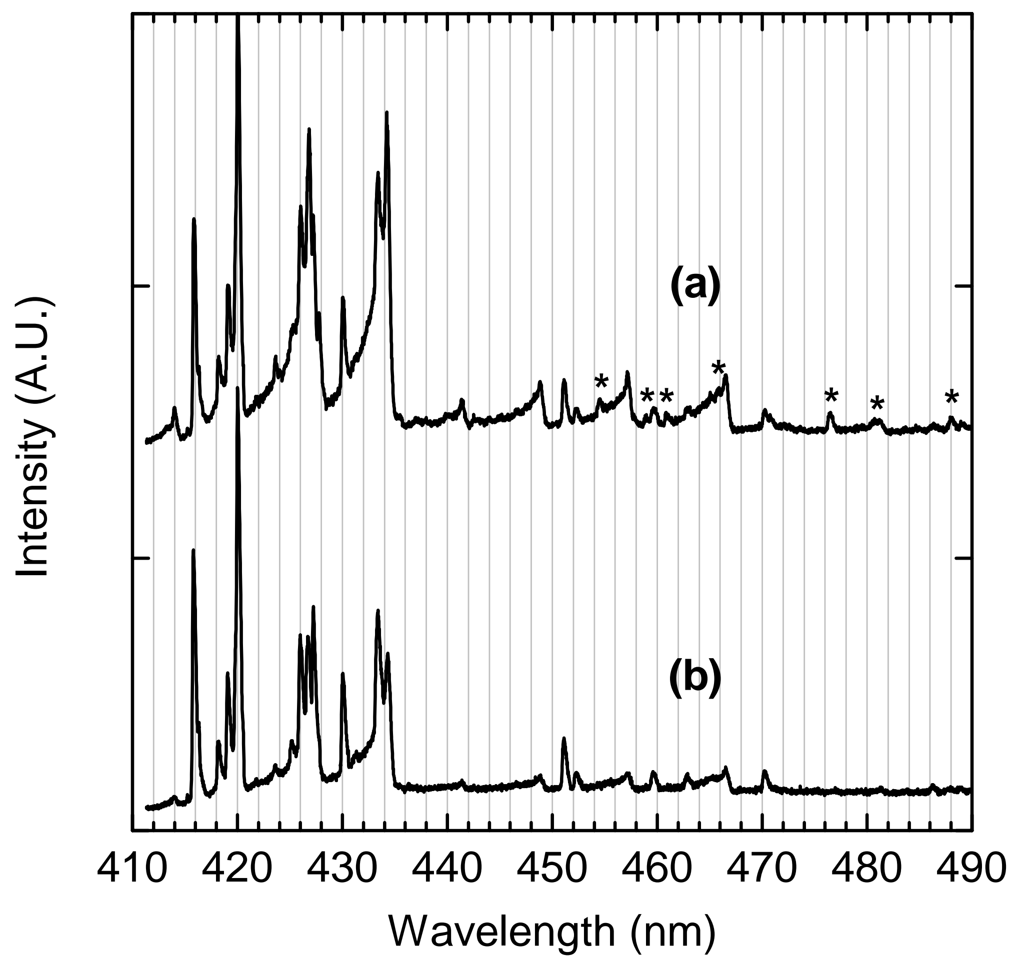

Figure 2.9. Emission spectra of Ar plasma microjet in ambient air at 760 Torr in tubes with hole diameter of (a) 180 μm and (b) 500 μm. Argon ion lines marked by asterisk. Cathode-anode gap=2 mm, flow rate=200 sccm, plasma current=10 mA.

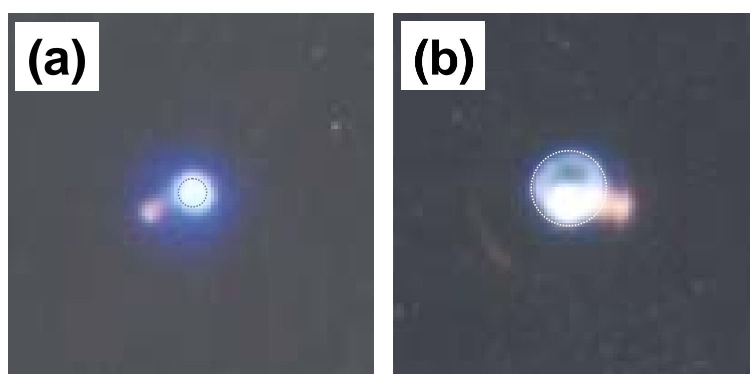

Figure 2.10. Color photographs of Ar plasma microjets in ambient air at 760 Torr in tubes with hole diameter of (a) 180 μm and (b) 500 μm. Photos were taken on axis through a metal aperture as depicted. The capillary tube hole boundary is outlined by a circle. Argon flow rate=100 sccm, plasma current=5 mA.

Chapter 3

A NON-LITHOGRAPHIC TECHNIQUE FOR ETCHING MICROSCALE PATTERNS[2]

3.1 Introduction

Plasma etching of silicon is a well-established process used extensively in the semiconductor industry to define sub-micron features with a high degree of anisotropy. It is also successfully used in patterning larger scale features for optical and MEMS applications. Pattern transfer generally requires multiple lithographic and etching steps depicted in Fig. 3.1(a) that, in turn, are time-consuming and costly as they rely on significant infrastructure. Moreover, there is a lot of waste associated with the use of bulk plasmas in patterning. For example, only a small fraction of the ions and reactive species produced in the bulk plasma contribute to the patterning process. Since the electron Debye length under typical low-pressure plasma conditions (<20 mTorr) is in the order of hundreds of microns, the plasma remains outside the features being patterned. A shift in paradigm to the lithography and etching approach would be to use a stencil mask with the pattern already defined in it, then strike a plasma within the pattern in contact with the wafer surface as shown in Fig. 3.1(b). If the stencil mask could be used multiple times, it could lead to a virtually "maskless" direct patterning technique. Since the plasma is formed only where it is needed to generate the

[2] Material in this chapter adapted from: R. M. Sankaran and K. P. Giapis, Appl. Phys. Lett. **79**, 593 (2001) and R. M. Sankaran and K. P. Giapis, J. Phys. D **36**, 2914 (2003).

reactive radicals and ions, neither plasma volume nor power would be wasted. In order for the plasma to form in such confined spaces, the electron Debye length must be decreased which is easily accomplished by increasing the ambient gas pressure. However, stable plasma operation at high pressures is generally difficult as very large electric fields must be established and maintained for efficient electron acceleration and the ensuing ionization phenomena that sustain the plasma. Microhollow cathode discharges have an inherent advantage from this perspective by means of the Pendel effect. Enhanced ionization within the confines of a mask cutout could facilitate pattern transfer. The question is then, how small a feature can be achieved and with what fidelity? It has been shown that discharges could be struck in features as small as tens of microns [27], a length scale appropriate for MEMS device fabrication [28]. Furthermore, the ability to form microdischarges in flexible stencil masks could allow the patterning of curved surfaces such as cylinders and spheres, a task of considerable difficulty with conventional patterning techniques. We present here an account of our effort to pattern Si wafers using microplasmas formed in flexible stencil masks and discuss limitations of the technique.

3.2 Pattern filling: design of a stencil mask

Direct patterning is possible if and only if the cutout pattern in the stencil mask can be filled with plasma. The cylindrical confinement in holes takes full advantage of the Pendel effect, which may not necessarily occur in lines resulting in lower electron densities and much weaker ionization. Our initial efforts were therefore focused on fabricating and testing multiple hole and line patterns in metal-dielectric-metal structures. Devices were

constructed from thin copper foils (100 μm thick, 99.995% pure) which were spin-coated with polyimide films as described in the literature [15]. These materials were chosen for degradation resistance when exposed to fluorinated gaseous precursors, as well as for their flexibility. Holes were drilled and slots were cut out mechanically in the layered structure to produce a desired pattern. Either a solid copper foil or, in the case of etch experiments, a blanket n-type Si (100) wafer was pressed firmly against the mask as illustrated in Fig. 3.2. The assembly was then placed in a reactor chamber and evacuated to 1×10^{-6} Torr. Silicon wafers were cleaned prior to etching by dipping in a dilute HF solution (1-5% in H_2O) for 1 minute and rinsing with de-ionized water.

Discharges were struck in both pure argon and etch gas mixtures at a variety of pressures and plasma parameters. Complete pattern filling by the discharge depended on pattern shape and operating conditions. In the case of an array of identical holes, discharges were initiated in each hole simultaneously and filled all holes uniformly. An example is shown in Fig. 3.3(a) for a 3 × 3 array of 200 μm holes; the discharge was struck in a CF_4/Ar mixture at 20 Torr. For line patterns, initial breakdown occurred in a part of the open structure requiring higher currents for complete space filling. Figure 3.3(b) shows a microdischarge filling three lines 0.2 mm × 10 mm, operated in CF_4/Ar at 20 Torr; the total current drawn by the discharge was 3 mA. Although not shown here, more complex patterns consisting of multiple holes and crossed lines could also be filled with plasma, provided sufficient plasma current could be supplied.

3.3 Optical characterization of discharge

The presence of reactive species in etch gas mixtures was verified by optical emission spectroscopy. The spectra were obtained with the optical set-up described in Section 2.4. Figure 3.4(a) illustrates a representative spectrum of a CF_4/Ar discharge (1:3) operated at 20 Torr and 1.5 mA. Because of the large amount of argon in the mixture, only the most intense fluorine atom lines are visible at 685.6, 690.2, and 703.7 nm (indicated by an asterisk). These excited states have been found to be important in Si etching involving radio-frequency discharges operated at lower pressures [29]. A spectrum for a SF_6/Ar discharge operated at similar conditions is also shown in Fig. 3.4(b) for comparison. The latter discharge produces higher intensity atomic fluorine lines, corresponding to a larger concentration of these species. It is, therefore, expected that gas mixtures with SF_6 will etch faster than with CF_4 because of enhanced production of fluorine atoms.

3.4 Etching single holes in silicon

When a complete metal-dielectric-metal structure was used to pattern Si wafers, the etching was characterized by low rates as a result of deposition of sputtered cathode material on the Si surface. This observation suggests that either a low sputtering yield electrode must be used as the cathode or the Si wafer must be part of the circuit (the cathode itself). Biasing the Si wafer as the cathode also ensures that ions are directed towards the substrate to promote the etch process. The latter configuration eliminated contamination from the

electrode material and achieved high etch rates of Si attributed to the direct contact between the discharge and the substrate. The etch rate depended on discharge current, pressure, and mixture composition. For example, a Si etch rate of 7.7 μm/min was obtained when etching a single 200 μm hole at 20 Torr using a mixture of 1:3 CF_4/Ar discharge operated at 1.5 mA. After the discharge was initiated, the plasma voltage was kept constant for the duration of the experiment. It was found that etching of the substrate altered the shape of the cathode, which affected both the operating voltage and current. When the voltage was kept constant, the discharge current increased linearly with etch time as shown in Fig. 3.5.

Although we are discussing applications of high-pressure microdischarges, etching experiments were confined to below 50 Torr. It was found that etching at higher pressures generally results in isotropic profiles with significant undercutting. Most of the experiments were performed between 10-50 Torr for high etch rates and profiles that conform to the mask at least initially (*vide infra*). Note that these pressures are still very high as compared to those employed in modern plasma etching reactors (~10 mTorr).

Scanning electron microscope (SEM) images of etched substrates were taken to determine etch rates and profiles. Parts (a)-(c) of Fig. 3.6 show profiles obtained after etching in CF_4/Ar (1:3) discharges for 10, 15, and 20 minutes, respectively. In each case, the pressure was controlled at 20 Torr while the voltage drop between anode and cathode was maintained at 400 V. The same stencil mask with a 200 μm diameter hole was used to etch each of these samples with no observable damage to the mask. For the etch times studied, there was also very little undercutting of the mask. At the early stages of etching [Fig. 3.6(a)], the pattern transferred with good fidelity and virtually no dimensional loss; it was noted that the bottom of the profile was rounded. As etching continued [Fig. 3.6(b)], erosion of the sidewalls occurred resulting in a bowl-shaped profile. At even longer times

[Fig. 3.6(c)], the etch rate in the vertical direction diminished greatly while etching in the horizontal direction accelerated. To quantify these effects, the dimensions of the etched holes have been measured in the horizontal and vertical directions and listed in the following table:

Table 3.1. Maximum width (w) and depth (d) of holes etched in silicon for various etch times. The corresponding etch rates are also listed.

Time (min)	w (μm)	Rate in w (μm/min)	d (μm)	Rate in d (μm/min)
10	210	1.0	77	7.7
15	258	4.8	112	7.0
20	274	1.6	129	3.4

Initial etch rates in the vertical direction are as high as 7.7 μm/min, but decrease with time. Etching in the horizontal direction is initially low (1.0 μm/min) before increasing as the etch progresses. After 20 minutes, the etch rates in both directions are low.

To explain this process, it is hypothesized that the bowl-shaped profile is a result of the expansion of the plasma into the etched void. As the plasma fills this volume, the sheath may conform to the shape of the generated cavity. A conformal sheath could result in ion bombardment of the cavity walls in a spatially uniform fashion, yielding etching of both the bottom and the sidewalls. We have verified the proposed mechanism by calculating the surface areas of the voids. As shown in Fig. 3.5, the estimated areas follow the trend of the increase in discharge current during the etch. This is representative of a constant cathode current density in the discharge which confirms that the plasma occupies a larger volume as

the etch progresses. But, why does the etch slow down over time? Since the current density is constant, the plasma density should not change during the etch. The etch rate may decrease over time because of etch products that are not removed from the hole and redeposit or remain in the hole. Similar profiles have been reported in experiments with sub-millimeter hollow cathode discharges operated in neon gas, albeit due to sputtering [10]. In that case, initially cylindrical holes also approached a stable spherical profile which was attributed to a balance between sputtering and deposition [10].

Silicon etch profiles were also studied for SF_6/Ar (1:3) discharges as a function of time. At identical pressure and bias conditions, the Si etch rate was substantially larger than that for CF_4 gas mixtures with notable similarities in the profile (bowl-shaped). However, the profile also exhibits significant undercutting resulting in dimensional loss and larger holes (Fig. 3.7). Both observations are consistent with formation of a larger number of fluorine atoms in the SF_6 microdischarge as found by optical emission spectroscopy (Fig. 3.4).

In each of these etch experiments, the Si etch rate is proportional to the total discharge current. By plotting the discharge current as a function of etch time we can appreciate the significant differences in Si etch rate between CF_4 and SF_6 mixtures (Fig. 3.8). The increase in current observed in both cases is concomitant with the expansion of the discharge into the generated cavity. Assuming that the discharge is uniform over the entire hole, it appears that the cavity surface area (that is, the effective cathode area) increases a lot faster in the case of SF_6. The larger etch rate in the case of SF_6 is confirmed by SEM measurements. Thus, unlike conventional plasma etching, the discharge current offers a method to monitor the etch process *in situ*. This observation suggests that the profile shape can be tailored by altering the operating conditions during the same experiment. For example, in Fig. 3.9, etching of a Si wafer was started in a CF_4/Ar (1:3) gas mixture at 20

Torr; the voltage drop across the discharge was fixed at 400 V. The discharge current was observed to increase in a slight superlinear fashion. After 10 minutes, the pressure was reduced to 15 Torr, resulting in an immediate decrease in the discharge current as the plasma stabilized at the new pressure. Again the discharge current was observed to increase as etching progressed. After 10 more minutes, the pressure was again reduced to 13 Torr and the experiment continued with similar observations. After a total time of 30 minutes, etching was stopped and the sample was imaged, as illustrated in Fig. 3.10. In comparison to the etch results of Figs. 3.6 and 3.7, the profile was etched approximately to the same depth but with less widening of the hole. By reducing the pressure during etching, the plasma density was decreased which may have affected the etching mechanism in the hole. Other changes in the plasma conditions may also have similar effects on the etch profile allowing etching of higher aspect ratio structures.

3.5 Etching patterns

We have also etched arrays of 200 μm holes simultaneously at the same process conditions as those used in single-hole experiments. For the same operating voltage, an array of *n* holes required a discharge current approximately *n* times larger than that for a single hole. Figure 3.11(a) shows a Si wafer etched for 10 minutes using a stencil mask with an array of nine 200 μm holes. Etching occurred uniformly in each hole and produced profiles nearly identical to those seen for individual holes. The ability to etch arrays of holes is especially attractive for fabrication of microdischarge devices in silicon [23]. As a proof-of-concept, we have successfully initiated discharges in pure Ar after etching structures in Si

and evacuating the chamber from any reactive fluorine radicals. We have not yet studied what, if any, is the impact of the cathode shape on the characteristics of these discharges. While microdischarges are normally operated in holes, we have also extended our patterning method to other shapes. Figure 3.11(b) illustrates a result for etching Si (10 min in 1:3 CF_4/Ar mixture, discharge current adjusted to fill the pattern) using a stencil mask with three parallel lines, each 200 μm wide. There are notable similarities in cross-section with the arrays of holes.

3.6 Summary

A non-lithographic process has been developed using microdischarges as a stencil mask. Formation of CF_4/Ar and SF_6/Ar microdischarges allows direct etching of single holes into silicon wafers. Measurement of the discharge current during the etch provides an *in situ* monitor of the process. Power requirements are less than 50 mW to etch single holes to a depth of 100 μm. The technique is characterized by high etch rates, but is self-limited because of the expansion of the plasma into the etched area. The increase in the plasma volume is corroborated by the constant current density as the etch proceeds. At long times, the etched hole approaches a stable bowl-shaped profile implying that etching and deposition processes compete. Etching of complex patterns in silicon such as arrays of holes and lines is attractive for applications in micromachining.

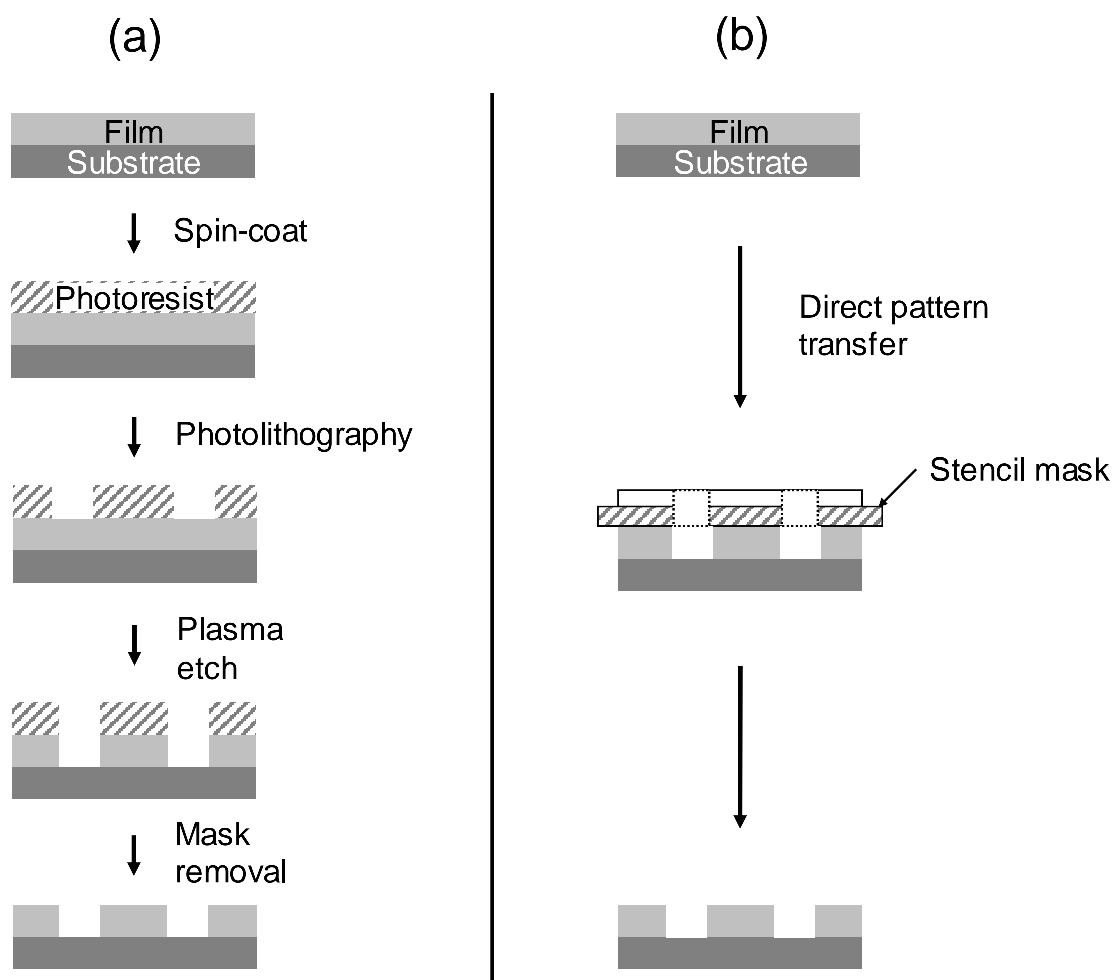

Figure 3.1. Comparison of microscale pattern transfer using (a) conventional lithographic steps and (b) new maskless technique with a microplasma stencil mask.

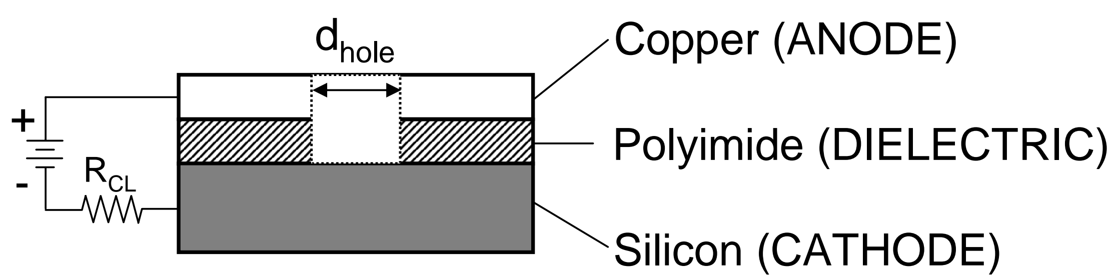

Figure 3.2. Schematic diagram of microdischarge set-up used for maskless etching of silicon. Current-limiting resistor, R_{CL}=100 kΩ.

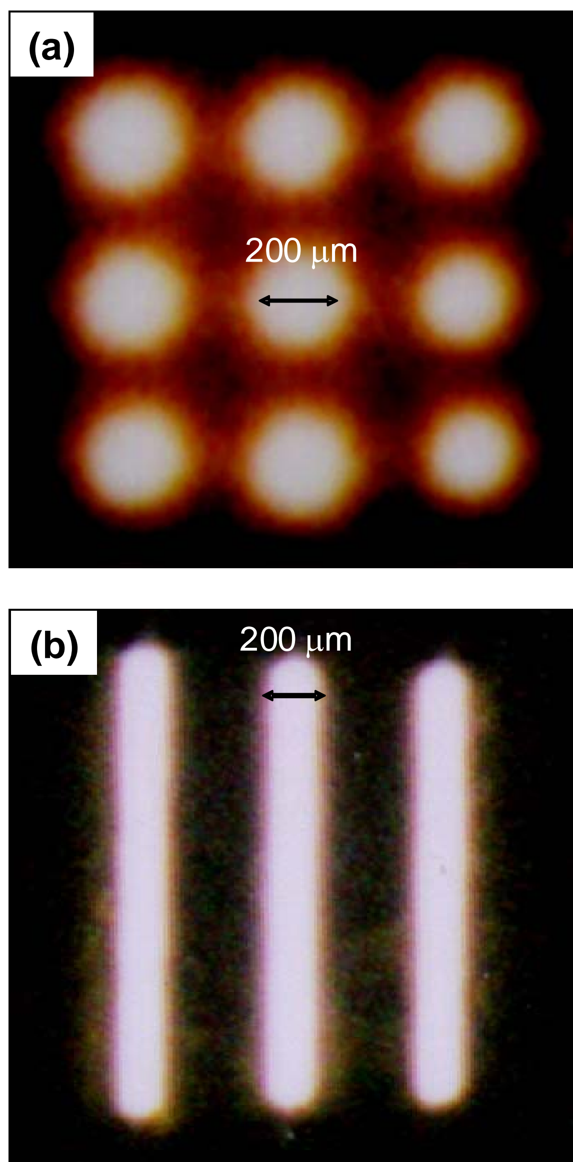

Figure 3.3. Color photographs of CF_4/Ar (1:3) microdischarge arrays at 20 Torr in copper-polyimide-copper devices for (a) 3 x 3 array of 200 μm holes (separated by 400 μm center-to-center) and (b) array of 3 lines each with width of 200 μm. Total discharge currents were 0.6 and 3 mA, respectively.

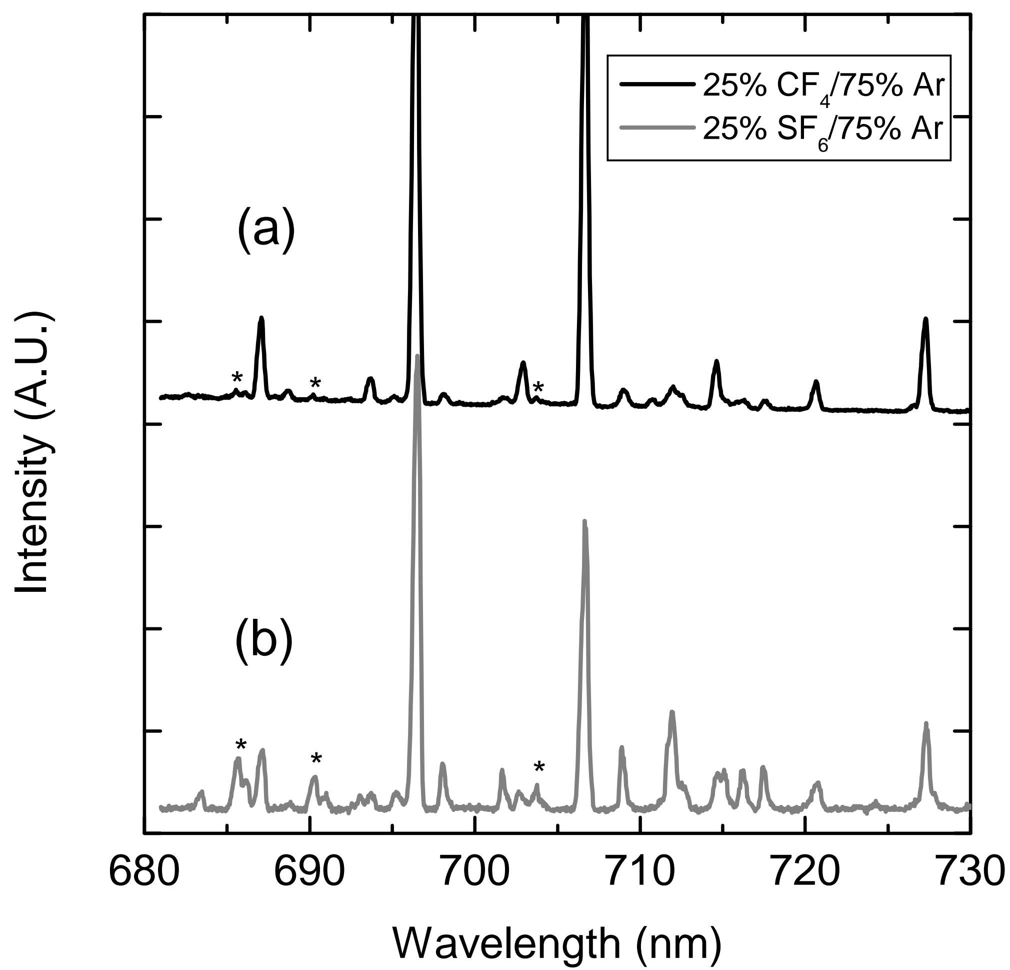

Figure 3.4. Emission spectra of microdischarges in copper-polyimide-copper devices at 20 Torr in (a) CF_4/Ar (1:3) and (b) SF_6/Ar (1:3). Discharge currents were 0.2 mA in both cases.

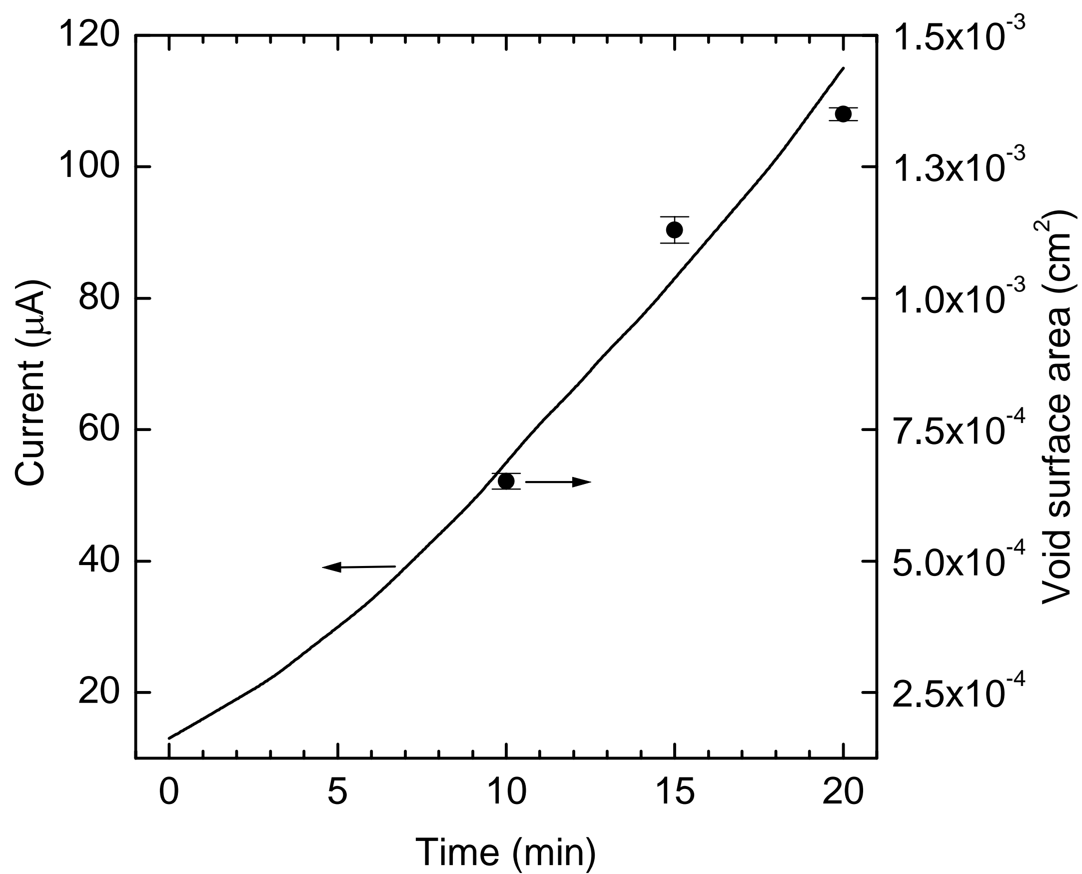

Figure 3.5. Discharge current versus time for etching a 200 μm hole in silicon using CF_4/Ar (1:3) microdischarge at 20 Torr. Discharge voltage was kept constant at 400 V.

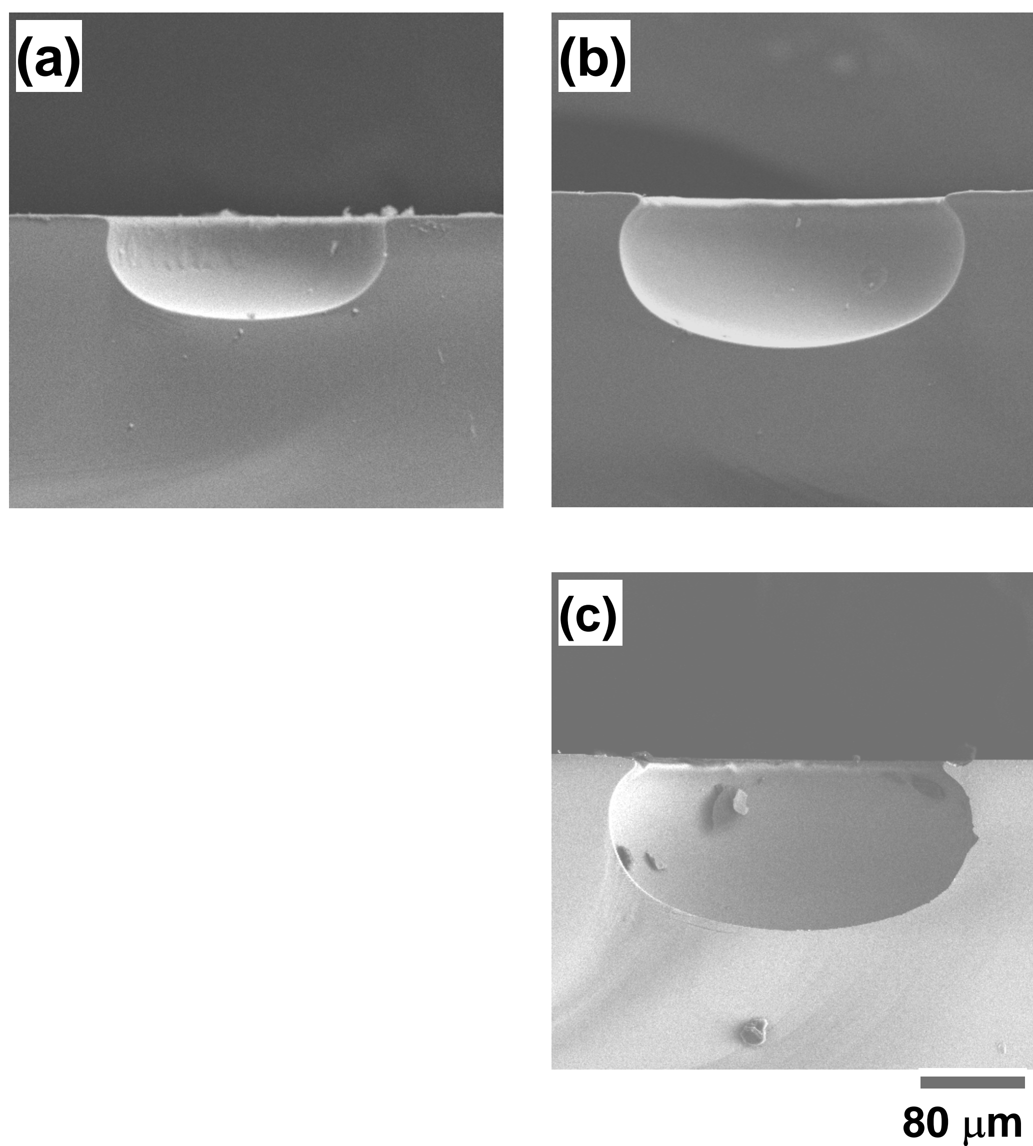

Figure 3.6. SEM images of single holes etched in silicon using CF_4/Ar (1:3) microdischarges at 20 Torr in a structure with a 200 μm diameter hole after (a) 10 min, (b) 15 min, and (c) 20 min.

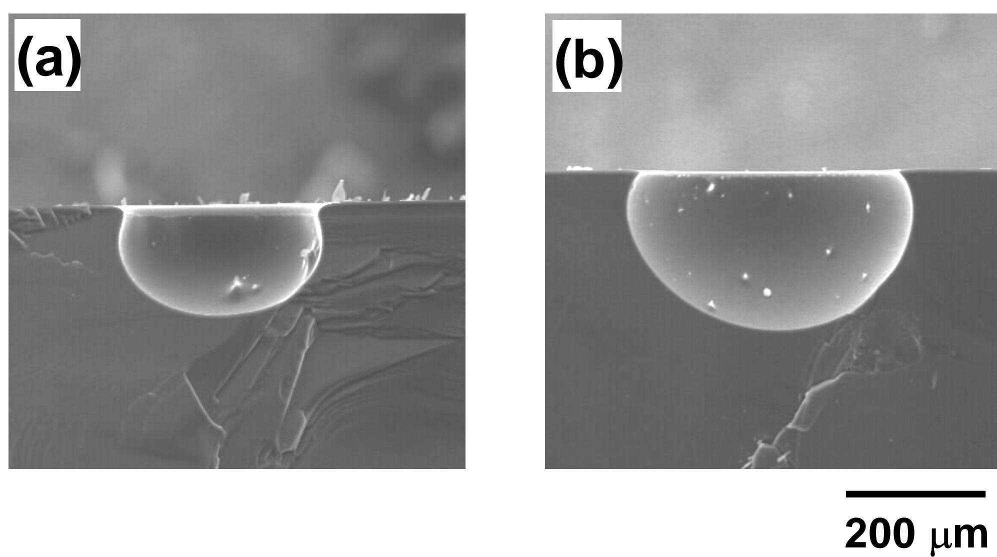

Figure 3.7. SEM images of single holes etched in silicon using SF_6/Ar (1:3) microdischarges at 20 Torr in a structure with a 200 μm diameter hole after (a) 5 min and (b) 10 min.

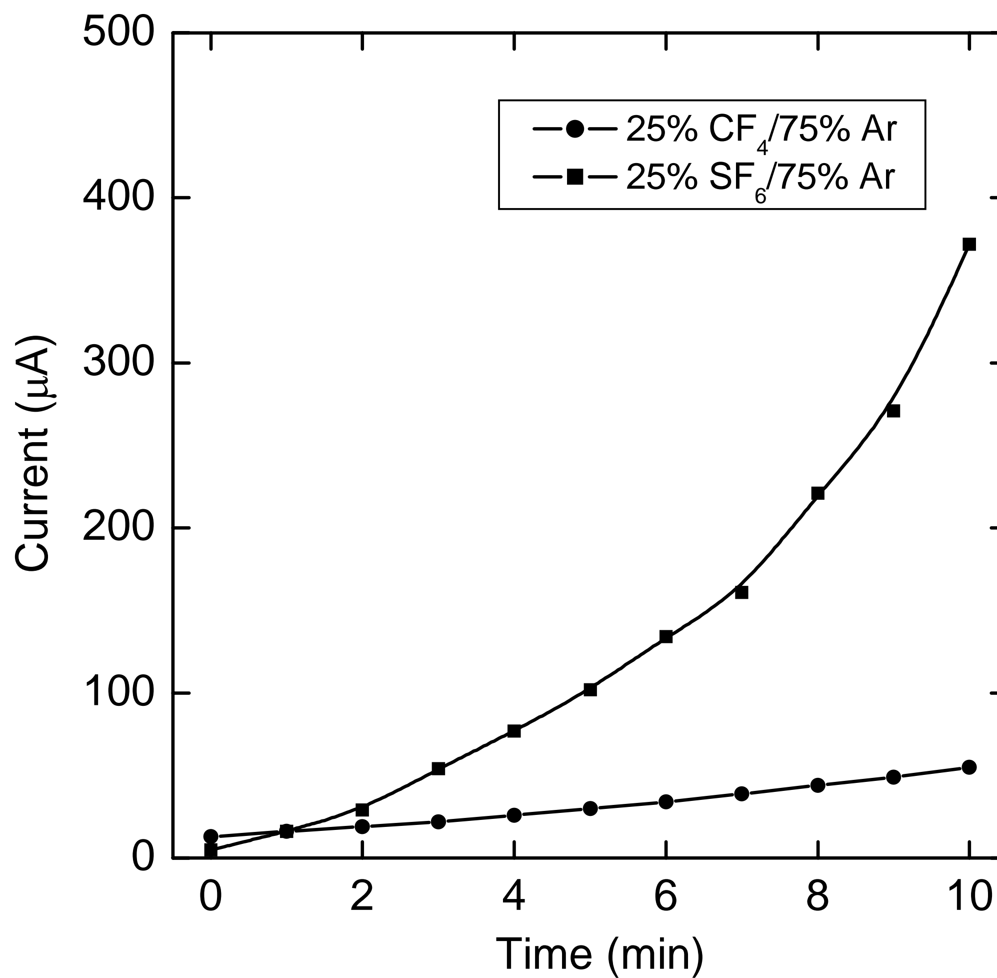

Figure 3.8. Plots of discharge current versus time for etching a 200 μm hole in silicon using CF_4/Ar and SF_6/Ar gas mixtures at 20 Torr. Discharge voltage was kept constant at 400 V in both cases.

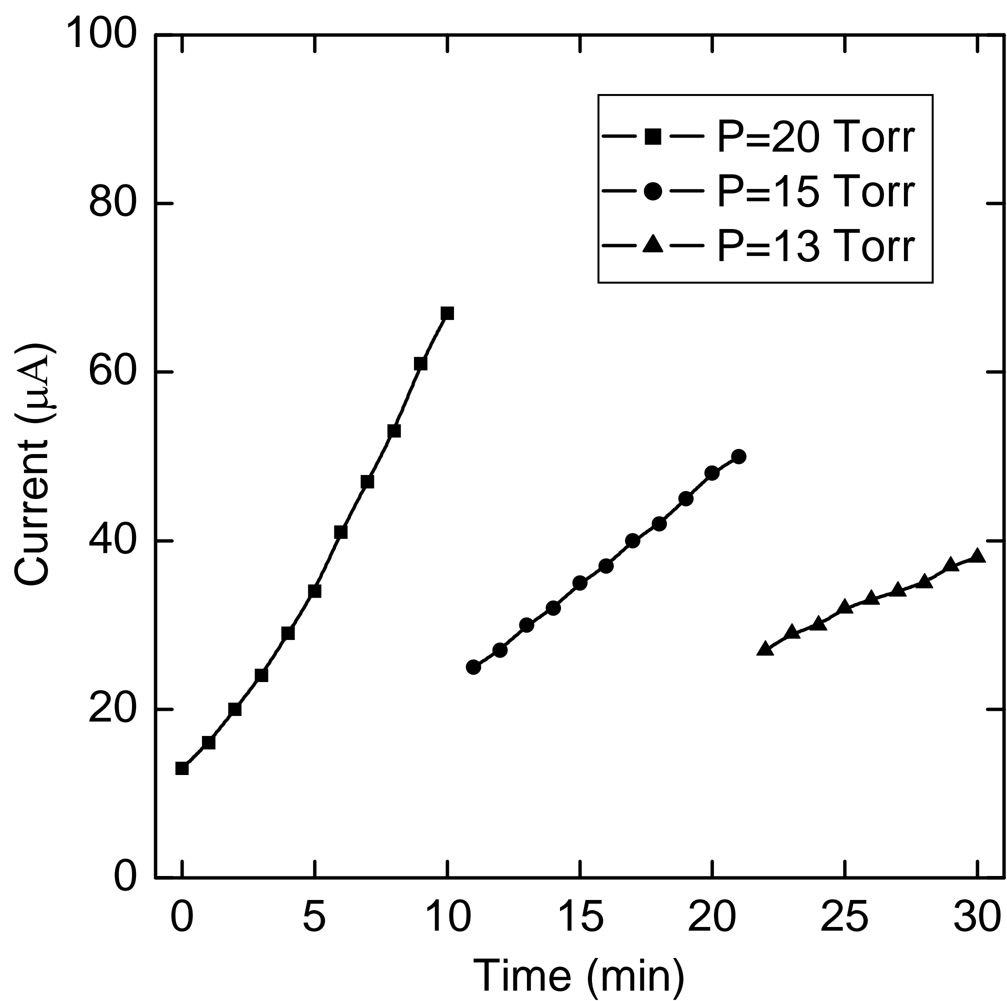

Figure 3.9. Discharge current as a function of time for etching a 200 μm hole in silicon with pressure changes every 10 min during a total etch time of 30 min. Other process conditions: CF_4/Ar (1:3), V = 400 V.

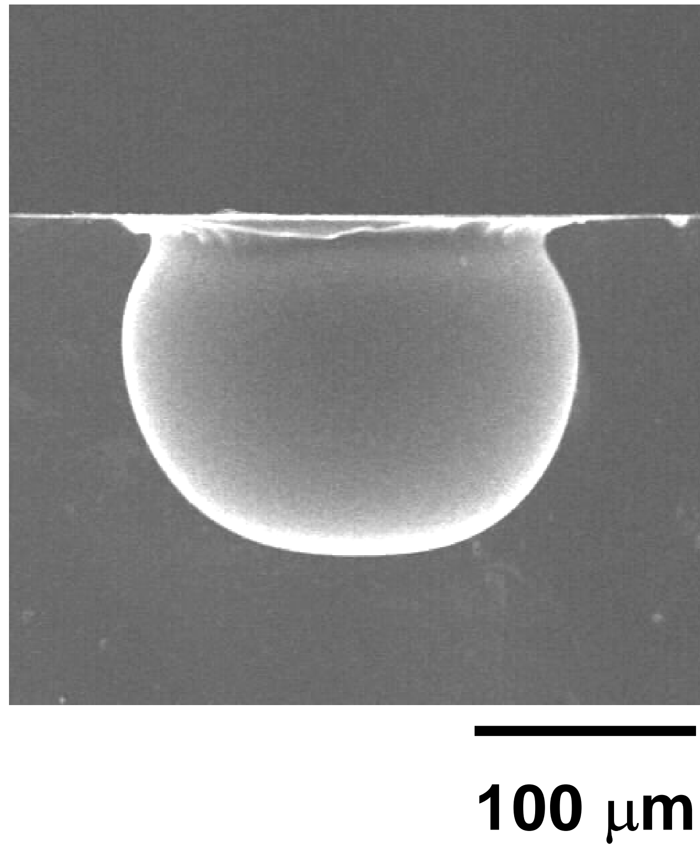

Figure 3.10. SEM image of single hole etched in silicon using process described in Figure 3.9.

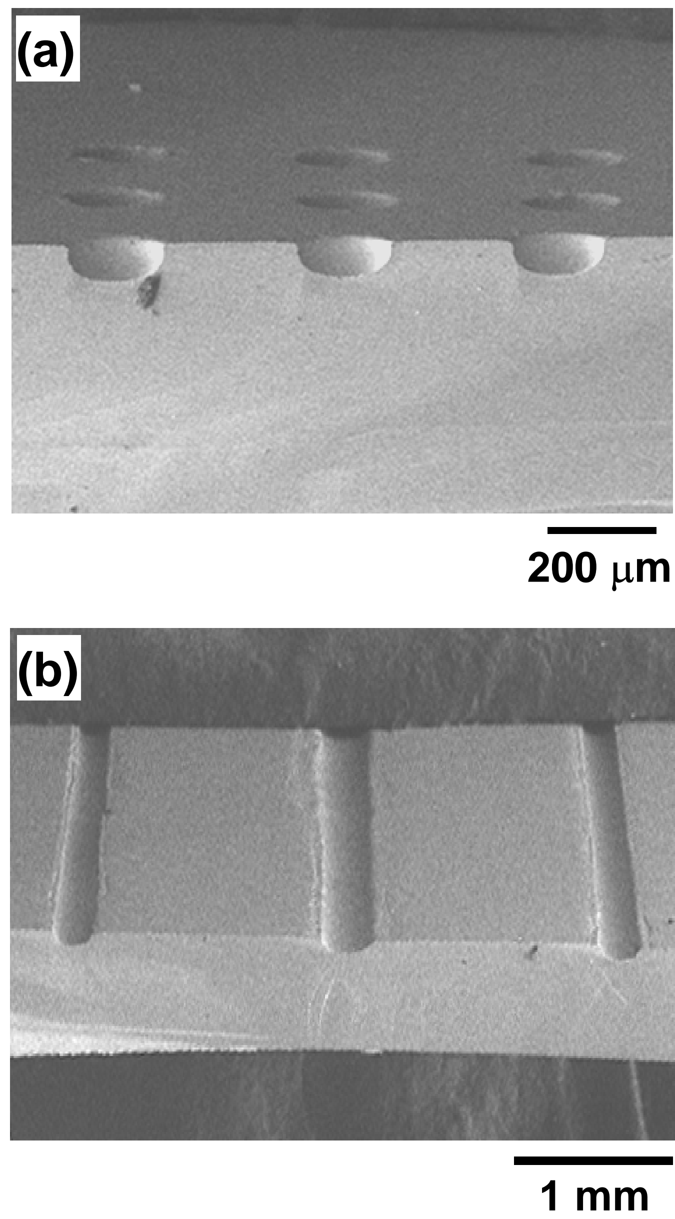

Figure 3.11. SEM images of silicon substrates after direct pattern transfer using stencil mask with (a) 3 x 3 array of 200 μm diameter holes and (b) 3 slots of 200 μm width.

Chapter 4

PLASMA MICROJETS FOR DEPOSITION OF POLYCRYSTALLINE DIAMOND FILMS[3]

4.1 Introduction

Efficient generation of radicals in a microdischarge resulting from operation in the hollow cathode mode is attractive for materials growth. In plasma-enhanced chemical vapor deposition (PECVD), radicals formed in a plasma by electron impact condense on a substrate to form a film [2]. A possible setup for film deposition using a conventional planar (metal-dielectric-metal) microdischarge is shown in Fig. 4.1. Assuming most of the species are neutral and unaffected by electric fields, the flux of radicals is only driven by diffusion as described by Fick's Law:

$$J = D \cdot \frac{dC}{dx} \tag{4.1}$$

where J is the molar flux, D is the diffusion coefficient of radicals in the gas, and dC/dx is the concentration gradient, C, of radicals in a direction, x, perpendicular to the film surface. Coupling of gas flow to the microdischarge would offer several advantages for deposition applications. A flow of gas allows continuous production and removal of radical species

---

[3] Material in this chapter adapted from: R. M. Sankaran and K. P. Giapis, J. Appl. Phys. **92**, 2406 (2002) and R. M. Sankaran and K. P. Giapis, J. Phys. D **36**, 2914 (2003).

from the discharge region avoiding deposition on the electrodes. Additionally, incorporation of gas flow should enhance deposition rates through convective transport of radical species from the discharge to the substrate [30]. This is especially important at high pressures where diffusion is decreased. The flux of species for the case of convective transport is given by:

$$J = C \times v \tag{4.2}$$

where v is the average speed of radicals moving towards the substrate. Previous studies have confirmed that the film deposition rate can be increased by increasing the gas flow rate in these forced flow geometries [30, 31].

Although flow could be adapted to the planar microdischarge in Fig. 4.1, there are several limitations to application of this geometry in film deposition:

1) the dielectric material separating the cathode from anode is a source of contamination;
2) incorporation of gas flow is difficult due to the planar geometry; and
3) device lifetime is adversely influenced by reactive gases and power dissipation.

Since the critical operating parameter for microdischarges is the cathode hole size, we have addressed these issues by replacing the dielectric with ambient gas and the planar cathode electrode with a metal capillary tube as discussed previously in Chapter 2. Possible electrode configurations for film deposition using a hollow cathode tube are illustrated in Fig. 4.2. In one version schematically depicted in Fig. 4.2(a), a discharge is formed between a single metal tube cathode and a substrate biased as the anode. If dc power is used to sustain the

discharge, this arrangement is restricted to substrates that are conductive. Deposition of films on insulators is possible by applying radio-frequency (rf) power to the electrodes [31-34]. Alternatively, the substrate can be decoupled from the discharge by using a coaxial tube structure with an inner tube cathode and an outer tube anode as shown in Fig. 4.2(b). This configuration also allows different gases to be flowed through the cathode and the annular region between the tubes. We have used the setup of Fig. 4.2(a) for experimental study because of its similarity to the conventional microhollow cathode discharge geometry. In this chapter, we discuss the application of plasma microjets to diamond film growth on a metal surface.

4.2 Polycrystalline diamond films

Diamond is a desirable material for applications because of its unique electronic, optical, thermal, and mechanical properties. Characterized by a wide band gap, high thermal conductivity, low dielectric constant, and high carrier mobility, diamond is promising for many semiconductor device applications [35, 36]. The growth of polycrystalline diamond films on a variety of substrates has been achieved by chemical vapor deposition techniques including hot filament activation, plasma enhancement, and combustion (pyrolysis). Although each of these methods has specific advantages and disadvantages, the common features are high processing pressures (10-1000 Torr), radical formation including methyl radicals [37] and atomic hydrogen [38], and transport of species to the substrate. Since plasma microjets are characterized by similar properties, we have pursued diamond film deposition to demonstrate the potential of microdischarges in materials growth.

The reactor setup for diamond growth experiments using plasma microjets is shown in Fig. 4.3. Direct-current discharges were formed between a stainless steel capillary tube cathode (Varian, Inc.) with a hole size of 180 μm and a substrate anode. Experiments were conducted on heated polycrystalline molybdenum foils (99.98% purity), although other conductive substrates could be used as well. Prior to film growth, the molybdenum foil was etched in a liquid solution of $HF/HNO_3/HCl$ and sonicated in an acetone bath. No scratching by diamond powder was necessary to initiate growth. Before each experiment, the deposition chamber was pumped down, then back-filled to the desired pressure between 100 and 500 Torr. Gas flow through the cathode tube was established by mass flow controllers at a constant flow rate of 100 sccm H_2 plus varying amounts of CH_4 between 0.1 and 1 sccm. For the plasma conditions investigated, the substrate was heated by the discharge itself to only slightly above room temperature. Because a temperature of at least 800°C was required to obtain diamond bonded (sp^3) films, external heating of the substrate was necessary. The substrates were heated resistively using a Kepco dc power supply (0-8 V, 400 W) with the temperature measured in situ by a Pt/Pt-Rh thermocouple. Since the gas flow cooled the substrate, it was important that the thermocouple was in contact with the molybdenum foil directly behind the impingement point. Discharges were struck with the capillary tube end 2 mm away from the substrate while maintaining constant discharge current and voltage during the growth. After growing for 2-4 hours, the films were characterized by scanning electron microscopy (SEM), energy-dispersive spectroscopy (EDS), and micro-Raman spectroscopy using a Renishaw M1000 Raman Spectrometer system with a 514.5 nm Ar laser.

4.3 Optical characterization of discharges

Optical emission spectroscopy was used to detect radical species in the discharge with the optical setup described in Section 2.4. Representative emission spectra of H_2 and CH_4/H_2 plasma microjets are shown in Fig. 4.4. In pure H_2, the strongest emission lines are from atomic hydrogen Balmer lines at 486.1 and 656.3 nm, noted as H_β and H_α, respectively. Many of the other lines in the spectrum are weaker atomic and molecular hydrogen states. When CH_4 is added to the discharge, lines appear in the region of 430 nm corresponding to a band of CH [39]. These lines become more intense with increasing CH_4 concentration. The emission spectra confirm that the discharges contain radical species that are necessary for diamond film growth. Although the principle growth species for diamond, CH_3 [37], does not emit and could not be detected, the presence of CH radicals indicates gas-phase decomposition. The nucleation of diamond begins with adsorption of hydrocarbon gaseous species on the substrate [35]. Atomic hydrogen plays a crucial role in abstraction reactions on the film surface that selectively etch non-diamond bonded material (sp^2) reducing the incorporation of graphite or amorphous carbon in the film [35]. Superequilibrium concentrations of hydrogen at the substrate have been previously shown to be necessary to enhance diamond film growth [38, 40]. While the intensity of the optical emission lines is not an absolute measure of the concentrations of the various species, the relative amounts of the radicals suggest that the discharge characteristics are consistent with those required for diamond deposition.

4.4 Characterization of films

A single microjet was used to grow diamond films at 200 Torr employing gas mixtures consisting of H_2 and varying amounts of CH_4. Since CH_4 is introduced in extremely minute amounts (0.1-1 sccm), its flow rate approximates its relative volumetric percentage. The gases were mixed in a region upstream of the microjet. For these conditions, the discharge was remarkably stable over a wide range of currents (5-20 mA) and could be run for hundreds of hours with no apparent damage to the tube. No contamination of the grown films could be detected (e.g., from erosion of the stainless steel tube due to sputtering or evaporation) by EDS. SEM images showed that the growth rate and morphology of the deposited films depended strongly on the CH_4 concentration in the gas mixture. For values over 1% CH_4 in hydrogen, mostly carbon was deposited and filamentary fibers made up of small soot-like particles were observed between the two electrodes. At 0.5% CH_4, a somewhat continuous film was deposited over a 500 μm diameter area. The film consisted of particles in high-density near the center and increasingly sparse coverage moving outwards. A close-up of the film [Fig. 4.5(a)] showed micro-scale roughness and some triangular faceting representative of diamond. As the CH_4 concentration was reduced further to 0.25 and 0.1%, individual crystals were observed with well-defined facets as shown in Figs. 4.5(b) and 4.5(c), respectively. These types of structures have been previously observed when the interaction between the substrate and film is weak as is in our case for an unscratched, non-diamond substrate. The multiply twinned diamond particle in Fig. 4.5(b) is known as an icosahedron [36]. To verify that these particles did not form in the gas-phase itself, we imaged the substrate from the side to view the film interface as shown in Fig. 4.6. The image indicates that nucleation is occurring at

the substrate. At these reduced CH_4 concentrations, the films exhibited sparser coverage with the heaviest number of particles at the stagnation point. This type of isolated particle growth has been reported for an atmospheric-pressure inductively-coupled plasma torch in a similar flow geometry [41]. Interestingly, there was little or no growth at the stagnation point in the latter study. This was attributed to lower concentrations of atomic hydrogen at the center than near the edges of the substrate. The improved coverage at the center in our experiments is consistent with the highest concentration of excited states expected along the centerline of the hollow cathode. At a longer deposition time of 4 hours, intergrowth of the particles resulted in a more continuous film as shown in Fig. 4.7.

Micro-Raman spectroscopy was performed to distinguish diamond bonded carbon (sp^3) from graphite or amorphous carbon (sp^2) for each of the samples in Fig. 4.5. The Raman effect is based on inelastic light-scattering arising from interactions of photons with the material lattice. Photons emitted from the sample will be frequency shifted with the vibrational modes depending on the atomic bonding in the solid. The first order optical phonon mode of natural diamond occurs at 1332 cm^{-1} [36]. Peaks at approximately 1350 cm^{-1} and 1580 cm^{-1} are characteristic of polycrystalline graphite [36]. For amorphous carbon, Raman scattering shows two broad peaks centered at 1350 and 1550 cm^{-1} [36]. If the amorphous carbon is hydrogenated (diamond-like carbon), the broad band at 1350 cm^{-1} becomes a shoulder of the 1550 cm^{-1} band [36]. Spectra for our samples are shown in Fig. 4.8. Each of the spectra contains a sharp peak at approximately 1336 cm^{-1} which is close to that of diamond. The shift in the peak is attributed to compressive stresses caused by lattice mismatch of the film with a possible underlying Mo_2C layer [41]. A broad peak at 1550 cm^{-1} was also present for films grown at the higher CH_4 concentrations of 0.25% and 0.5% indicating the existence of diamond-like carbon. In the latter case, a shoulder at

approximately 1150 cm^{-1} is discernible which has been attributed to small crystal sizes [42]. This observation is consistent with the smaller grain size seen in the SEM image of this film [Fig. 4.5(a)]. As the CH_4 concentration is reduced, the non-diamond peaks disappear and only a single peak at 1336 cm^{-1} remains suggesting a high-purity polycrystalline diamond phase. The overall trends for growth rate and film quality as a function of methane concentration are consistent with those obtained in modeling of CVD processes [40].

At the optimum growth temperature of 800°C, changes in pressure and flow rate were also studied to observe the effect on film morphology. An increase in the total flow rate to 200 sccm at constant pressure (200 Torr) resulted in crystals exhibiting both (100) faceting and (111) faceting; compare Fig. 4.9(a) to Fig. 4.5(b). Some pitting and overgrowth on the crystal planes were also seen. This particle morphology displays a pentagonal profile and is known as a decahedral-Wulff-polyhedron [36]. Increasing the pressure to 400 Torr at constant total flow rate (100 sccm) resulted in similar mixed faceting and more pitting. Figure 4.9(b) shows a particle corresponding to a cubo-octahedron which is the simplest morphology and is referred to as a single crystal [36]. For each of the particles in Figs. 4.5(b), 4.9(a), and 4.9(b), nucleation has been postulated to occur from the following gaseous hydrocarbon compounds: dodecahedrane, hexacyclo-pentadecane, and adamantane respectively [36]. These results suggest that by changing the discharge conditions, we are producing different hydrocarbon species for nucleation.

The diamond growth experiments demonstrate that plasma microjets can be used as a reactive source for depositing films of comparable quality to those produced by other often more complicated deposition techniques. The advantage of this tool is the simplicity of construction and operation, as well as the low power consumption. Although not shown here, thicker films are possible since the source is stable and allows deposition of films

continuously for much longer times. The coatings are restricted to small areas, but this may be desirable for materials processing on the microscale where patterning is not possible. Plasma microjets could also be utilized for the development of materials libraries for rapid property screening and optimization purposes [43]. Operation of arrays of plasma microjets allows multiple processes to be run simultaneously. Process parameters such as gas composition, flow rate, and input power can be varied to determine effects on film characteristics. Microscale integration of plasma processes is advantageous since the overall power and cost is reduced prior to optimization.

4.4 Summary

Incorporation of gas flow into microdischarges to form plasma microjets facilitates the deposition of thin films such as polycrystalline diamond. Optical emission spectroscopy indicates that CH_4/H_2 plasma microjets contain radical precursors that are necessary for diamond deposition. Using a heated molybdenum substrate, diamond particles and polycrystalline films have been deposited. Micro-Raman spectroscopy of the films shows mainly sp^3 content with slight shifting of the diamond peak due to internal stresses. The deposited films are comparable in quality to those produced by other techniques with the advantage that our tool is simple to construct and operate. Although the deposition is localized, the ability to form arrays of plasma microjets using one power supply renders them suitable for application in combinatorial experiments.

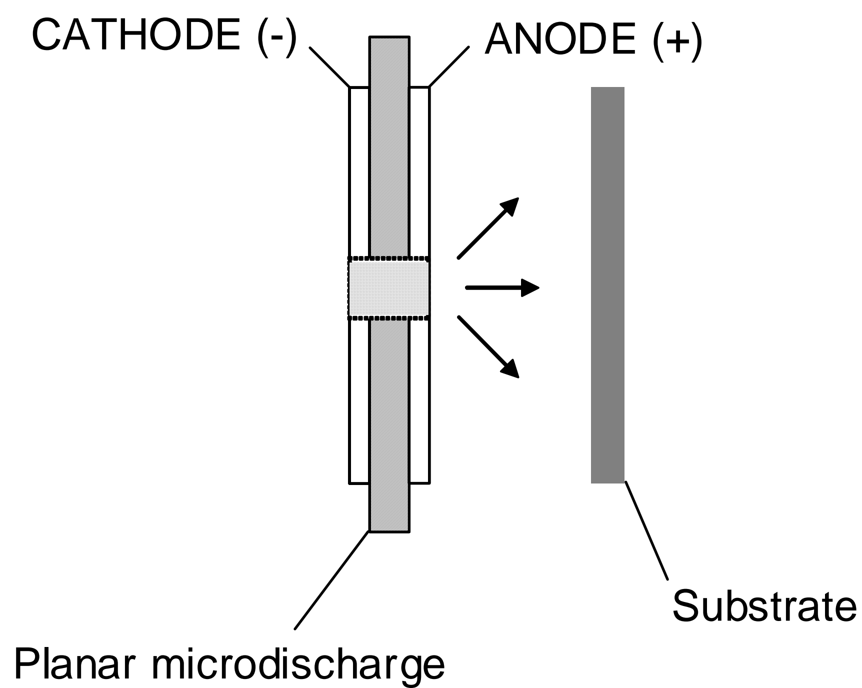

Figure 4.1. Illustration of setup for thin film deposition using a planar microdischarge. Radicals produced in the microdischarge diffuse to the substrate and condense to form a film.

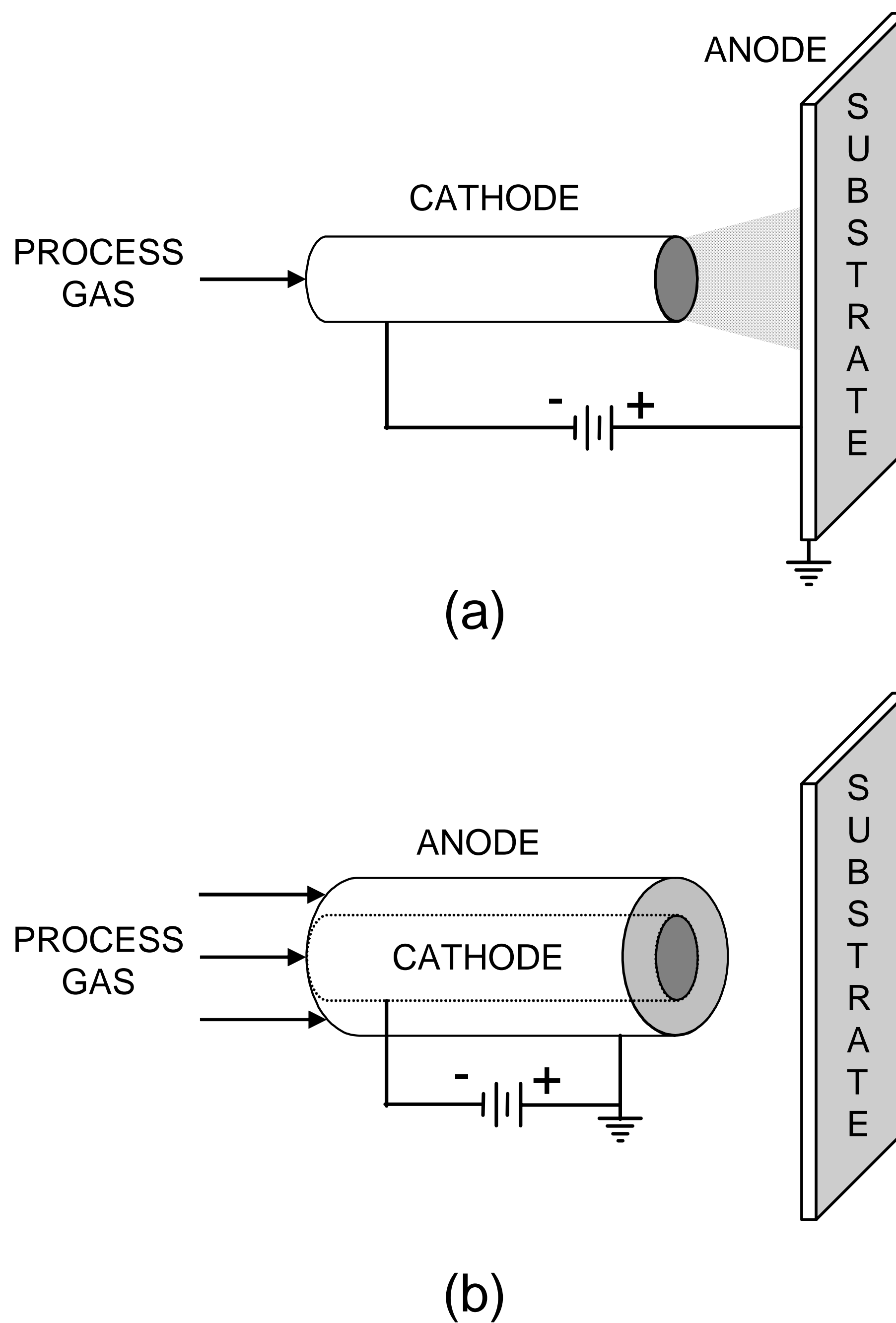

Figure 4.2. Possible configurations for depositing films with gas flow through a dc hollow cathode discharge. The electrode geometries are (a) a tube cathode with the substrate as the anode and (b) a coaxial tube as the cathode and anode with the substrate separated from the plasma circuit. Reproduced from Ref. 30.

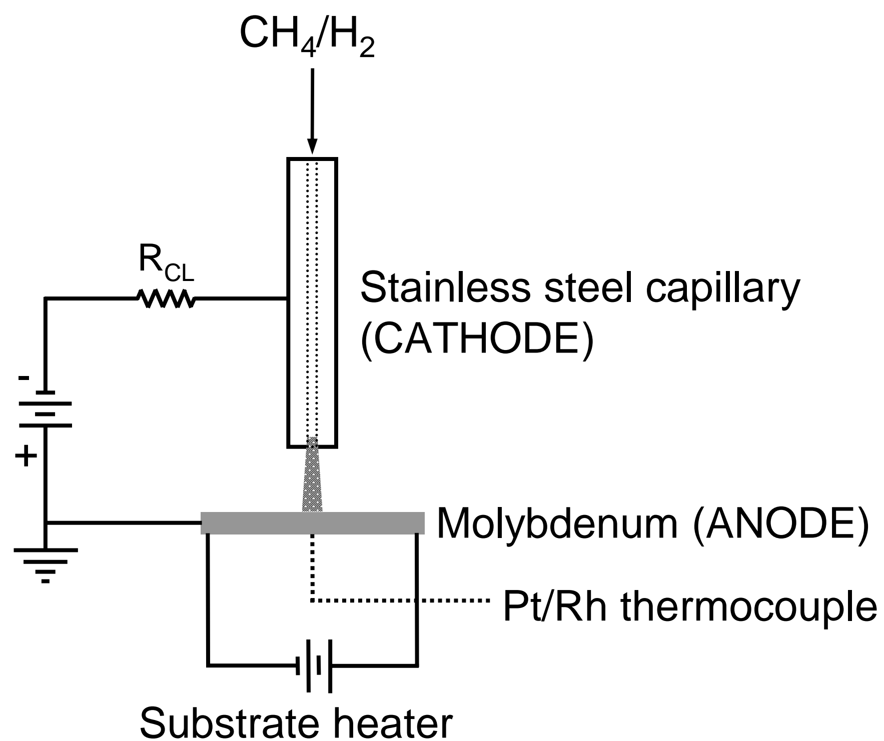

Figure 4.3. Schematic diagram of the setup used for diamond-like carbon deposition; the microdischarge forms at the tip of the capillary tube and expands toward the heated substrate.

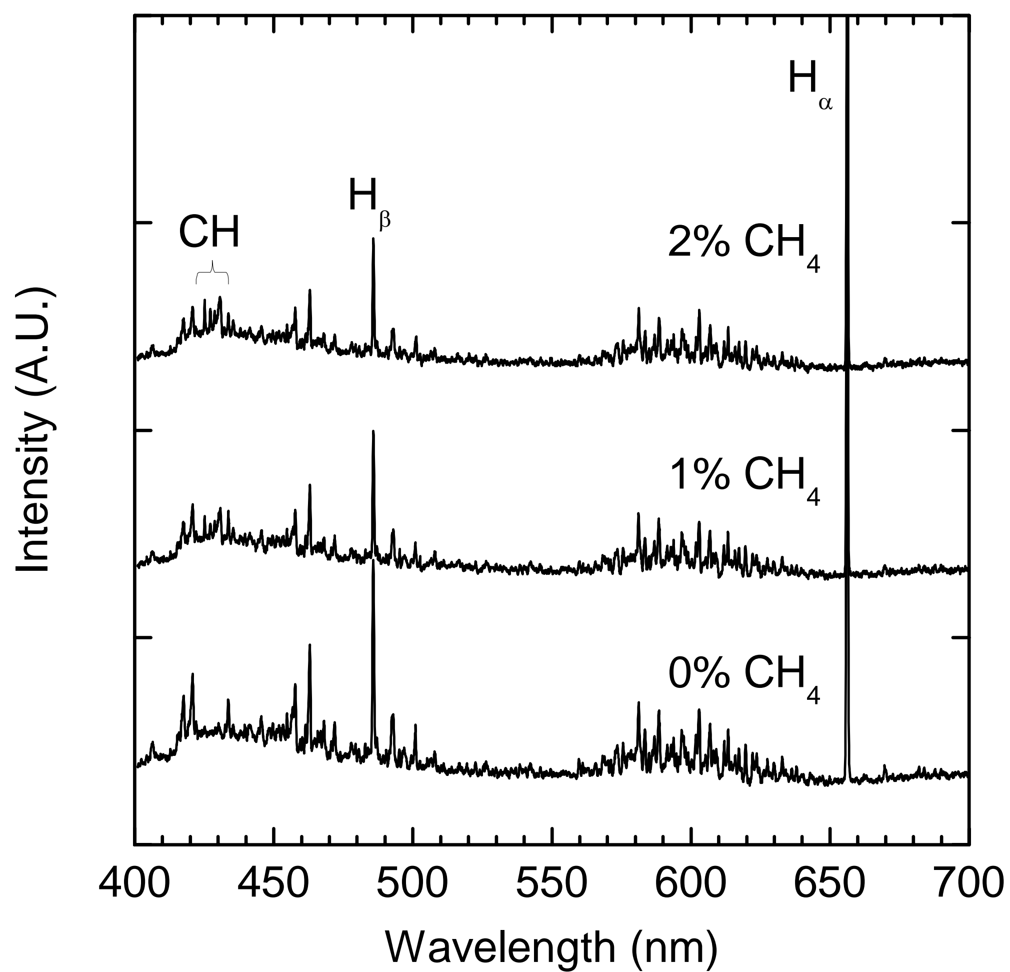

Figure 4.4. Emission spectra of H_2 and CH_4/H_2 plasma microjets at 200 Torr and 20 mA. Band of peaks corresponding to CH radicals is indicated.

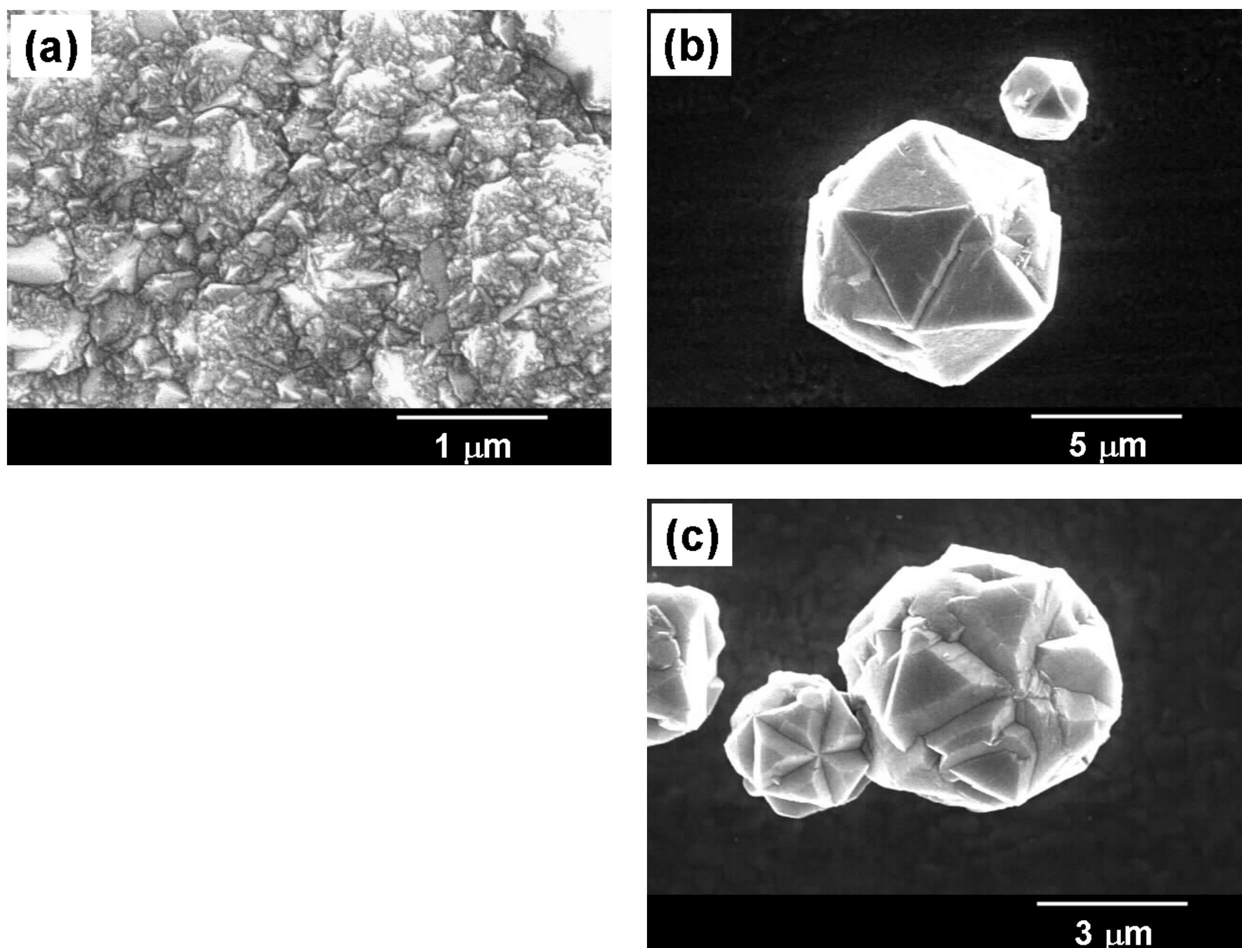

Figure 4.5. SEM images of diamond crystals grown using CH_4/H_2 plasma microjets at 200 Torr for 2 hours at methane concentrations of (a) 0.5%, (b) 0.25%, and (c) 0.1%. Cathode-anode gap=2 mm, total flow rate=100 sccm, plasma current=20 mA, substrate temperature=800 °C.

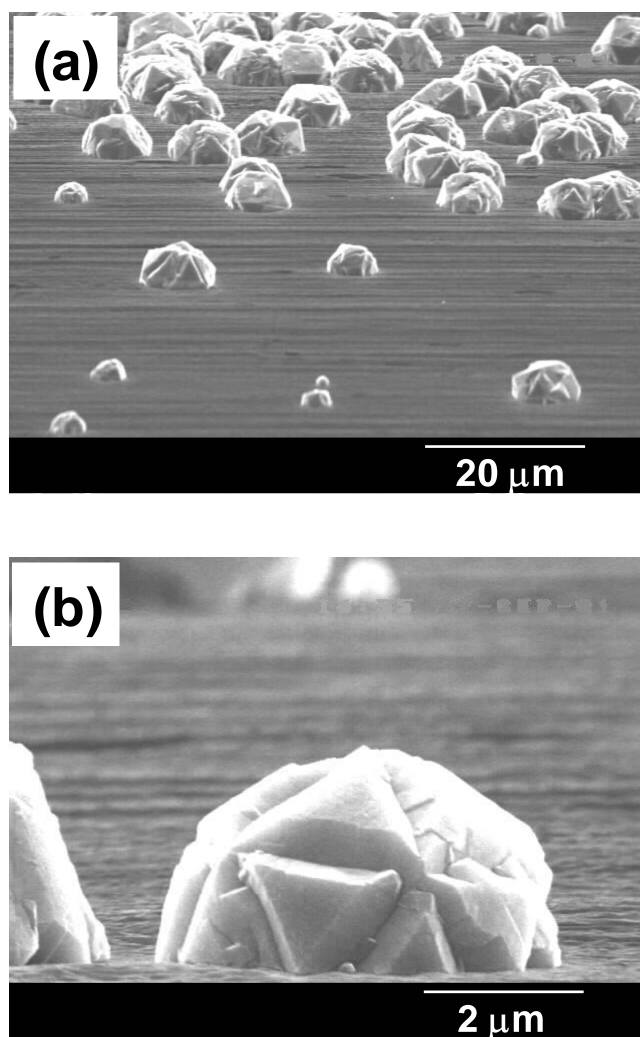

Figure 4.6. Side-on SEM images of diamond particles on molybdenum substrate.

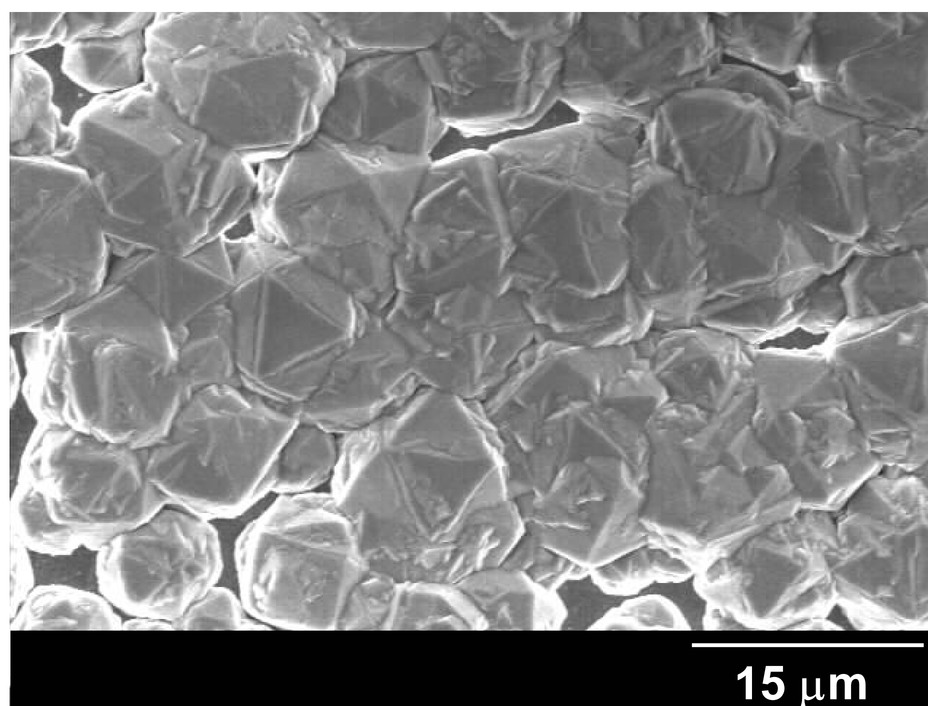

Figure 4.7. SEM image of diamond film grown using CH_4/H_2 plasma microjet at 200 Torr for 4 hours at a methane concentration of 0.1%. Cathode-anode gap=2 mm, total flow rate=100 sccm, plasma current=20 mA, substrate temperature=800 ºC.

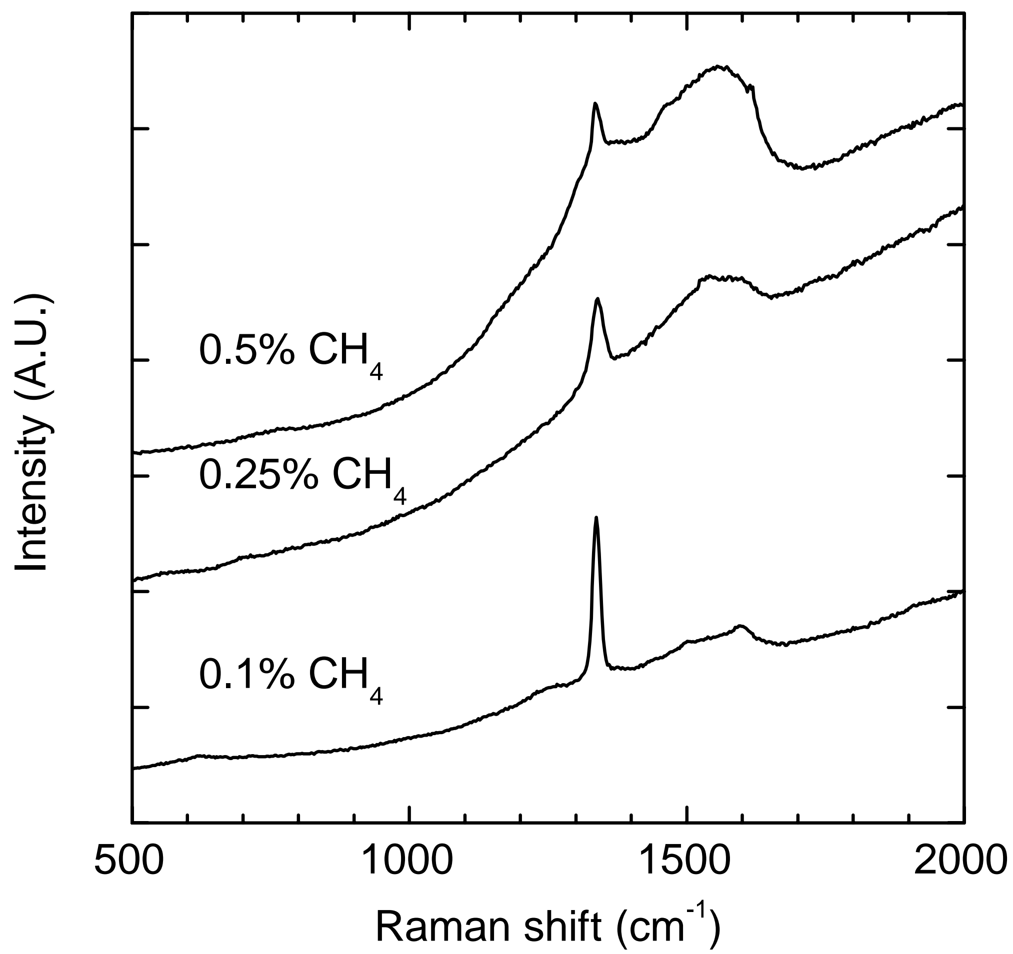

Figure 4.8. Micro-Raman spectra of diamond films corresponding to micrographs shown in Figure 4.5.

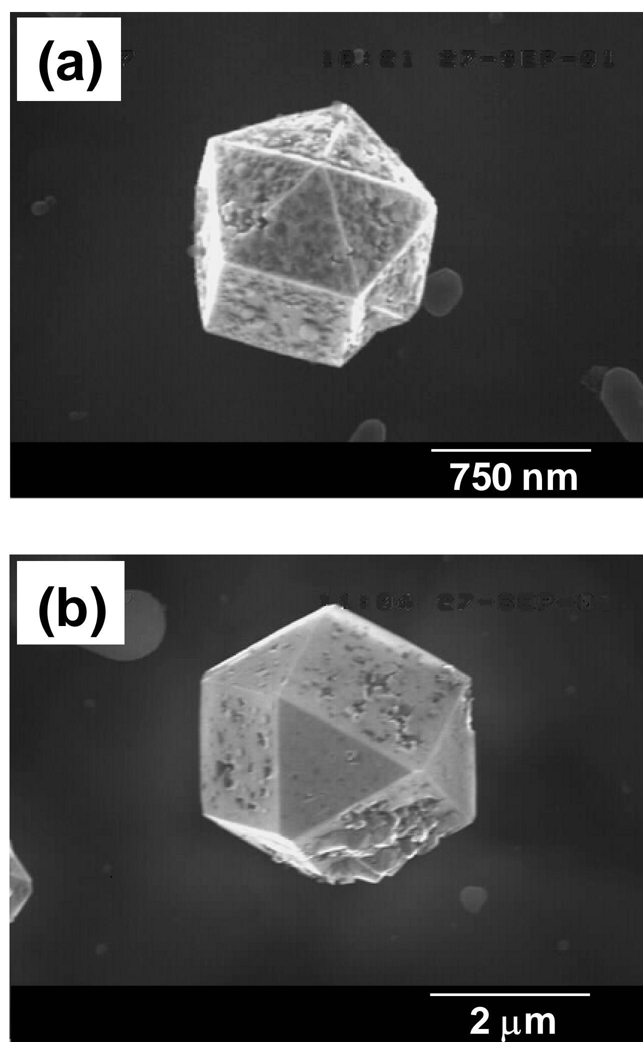

Figure 4.9. SEM images of diamond crystals grown using CH_4/H_2 plasma microjets with 0.5% methane at (a) higher total flow rate (200 sccm) and (b) higher pressure (400 Torr).

Chapter 5

EXCIMER EMISSION FROM MICRODISCHARGES IN METAL CAPILLARIES[4]

5.1 Introduction

Enhanced ionization processes in the hollow cathode can render microdischarges intense sources of UV light. Optical emission from discharges corresponds to radiative transitions involving various excited states in the gas. Excimers are excited molecular dimer complexes which can form in, for example, rare gases. De-excitation of excimers can lead to emission of vacuum ultraviolet (VUV) light with a wavelength below 200 nm [43, 44]. Radiation in this spectral region is important for applications in spectroscopy, photolithography, micromachining, and photochemistry. The use of excimers for VUV radiation offers several advantages including high intensity over a range of different wavelengths, longer lifetime as compared to filament sources, lower toxicity than mercury sources, and potential as a laser medium. Some examples of excimers and their emissive wavelengths are summarized in Fig. 5.1. For the rare gases, excimer formation usually occurs by the following process:

[4] Material in this chapter adapted from: R. M. Sankaran, K. P. Giapis, M. Moselhy, and K. H. Schoenbach, Appl. Phys. Lett. **83**, 4728 (2003).

$$M^* + 2M \longrightarrow M_2^* + M \tag{5.1}$$

where M^* is a metastable state of the neutral gas atom, M is the ground state, and M_2^* is the excimer. The metastable state M^* results from excitation of the rare gas atom in the $^1S_0$ ground state to one of four possible P states. In the case of argon, the metastable states are more than 11.5 eV above the ground state [43]. As described in Eq. 5.1, the excimer molecule is formed by three-body collisions between a metastable rare-gas atom and two ground state atoms. Once formed, the excimer molecules are not very stable and can de-excite to the ground state, emitting a VUV photon:

$$M_2^* \longrightarrow 2M + h\nu \tag{5.2}$$

The conditions for efficient generation of excimers are as follows:

1) a large concentration of electrons with energies above the threshold for the formation of metastable rare gas atoms; and
2) high-pressure operation in order to have sufficiently high rate of three-body collisions.

These conditions can only be met in non-equilibrium plasmas such as microdischarges where operation at high pressure does not result in thermalization and quenching of the electron energy. Indeed, excimer emission has been observed in microdischarges of Ne [45], Ar and Xe [16], ArF [19], XeCl [46], and XeI [47]. In these planar microdischarges, limited enhancement in the excimer intensity has been achieved by

increasing the gas pressure or discharge current [16]. Larger gains in emission intensity could be obtained more readily by increasing the total plasma volume [46, 48]. The tube geometry is attractive to fabricating such a device with more internal area for plasma expansion. Since high-energy electrons in microdischarges are created in the cathode fall region, a thicker cathode with a deeper hole should automatically provide a larger cathode area. In this chapter, measurements of excimer radiation from microdischarges in a metal capillary cathode are presented. We also discuss our efforts to amplify the excimer intensity showing potential for building a continuous wave (cw) excimer microlaser.

5.2 VUV spectroscopy

Detection of excimer radiation presents difficulties because light in the VUV wavelength range is strongly absorbed by oxygen and does not transmit through standard optical materials. Spectral measurements in the VUV were performed using a differentially pumped setup comprising of a high-pressure discharge chamber and vacuum monochromator illustrated in Fig. 5.2. Optical emission from the discharge was collected through a magnesium difluoride window (MgF_2) mounted at the inlet of a 0.2 m McPherson Model 302 scanning monochromator, with a grating of 600 grooves/mm blazed at 150 nm. The spectrally resolved radiation at the exit slit was detected by converting the light to visible using a sodium salicylate coated window (λ_{em}=425 nm) and measuring the photon intensity with a Hamamatsu R1533 photomultiplier tube. The entire spectroscopic system, including the monochromator, space between the source and entrance slit, and space between the exit slit and scintillator, were continuously pumped by a separate turbomolecular pump.

The setup for striking microdischarges in capillary tubes bears similarities with that of planar microdischarges, as schematically depicted in Fig. 5.3. The electrodes consist of a stainless steel tube (5 cm long, i.d.=180 μm) and a stainless steel grid, operated as the cathode and anode, respectively. A sapphire washer (i.d.=200 μm) separates the two electrodes by 380 μm. External cooling was provided by a water-cooled copper jacket surrounding the cathode tube (not shown). This required operation of the discharge with a Glassman dc power supply biased positively; the cathode tube is electrically grounded. Discharge voltage and current were measured via a digital oscilloscope and voltage drop across a resistor in series, respectively. The electrode setup was aligned with the inlet of the monochromator so that emission spectra could be collected through the grid anode. Before each experiment, the discharge chamber was evacuated by a turbomolecular pump then backfilled with high-purity gas to pressures between 200 and 1300 Torr. For xenon, a valve between the discharge chamber and turbo pump was closed off after backfilling. In the case of argon, gas was continuously supplied with a mass flow controller in two different configurations as indicated in Fig. 5.3: in a cross-flow arrangement through a side-port in the vacuum chamber or in an out-flow arrangement through the cathode tube.

5.3 Excimer emission

Emission spectra for Ar microdischarges in a cross-flow of gas are shown in Fig. 5.4 as a function of ambient pressure. At high pressures (> 400 Torr), the spectrum is dominated by the second excimer continuum of argon, peaking near 128 nm [43]. As the pressure is raised from 400 to 1000 Torr, the intensity of the excimer emission increases.

This is expected since excimers are formed by a three-body process which is enhanced at higher pressures. Also evident in the spectra are lines corresponding to atomic oxygen at approximately 130.5 nm and atomic carbon at 156, 160, and 165 nm. These lines are attributed to impurities in the microdischarge from outgassing of materials used in the device setup [49]. Increasing the cross-flow rate did not reduce the contamination. Similar spectra were also obtained for Xe discharges as shown in Fig. 5.5. At 200 Torr, the first and second continua of the Xe molecular state are evident. The second continuum results from the radiative decay of low-lying vibrational levels of the triplet ($^3\Sigma_u^+$) excimer state while transitions from higher vibrational levels of the singlet ($^1\Sigma_u^+$) excimer state give rise to the first continuum [50]. Also evident at 200 Torr is the 147 nm Xe resonance line corresponding to a transition involving the $^3P_1$ state which is a precursor for excimer formation. At higher pressures, spectra are dominated by the second continuum at 172 nm. This effect represents an increase in the population of the $^3\Sigma_u^+$ molecular state at the expense of the $^1\Sigma_u^+$ state [51]. Interestingly, in comparison to argon, the excimer intensity reaches a maximum at an intermediate pressure of 600 Torr. No impurity lines were present in the Xe excimer spectra.

Besides pressure, the excimer intensity was also found to increase with discharge current. The total VUV intensity or optical power was estimated by integrating the emission spectra. In Figs. 5.6-5.9, the optical power of Ar microdischarges is shown as a function of current at various pressures. Also shown for reference are the discharge voltages. To avoid excessive heating of the discharge, the current was limited to 10 mA in all cases. A common feature in each of the plots is a peak value in the optical power as the discharge current is increased. The position of the maximum, however, shifts to higher currents as the pressure

increases. While a maximum is obtained at 2 mA for 400 Torr (Fig. 5.6), the optical power is found to increase up to 6 mA for 1000 Torr (Fig. 5.9). These results can be explained by a picture of how the plasma fills the cathode tube. Expansion of the plasma is a diffusional process and depends inversely on pressure. As a result, the optical power is maximized at higher currents as the pressure is raised. Increasing the discharge current is expected to amplify the intensity of excimer emission by enlarging the plasma volume. Our results suggest that the plasma volume does increase but only to a limited extent. Operation in the abnormal glow discharge mode is indicated by the positively-sloped current-voltage curves in Figs. 5.6-5.9. As described in Section 1.3, the abnormal mode is characteristic of complete coverage of the cathode surface by the discharge. Since the tube geometry should provide abundant surface for the plasma to expand, this result is surprising. It is possible that heating of the tube leads to electron emission at the tube end thus limiting plasma expansion. The eventual decrease in optical power is caused by heating of the gas, known to severely reduce the excimer emission [52]. This is caused both by a reduction in gas density with increasing temperature and a decrease in the rate coefficient of the three-body process required for excimer formation which scales with the neutral gas temperature as $T^{-1/2}$ [53].

5.4 Effect of gas flow

Cooling of the discharge should be more effective when gas is flown through the cathode tube. Figure 5.10 shows emission spectra obtained from an Ar microdischarge as a function of the flow rate. The discharges was operated at an ambient pressure of 1000 Torr and a current of 4 mA. Unlike the emission spectra for cross-flow of the gas (Fig. 5.5), lines

from oxygen and carbon contamination were indiscernible even for the lowest flow rate. The absence of emission lines from contaminants is attributed to a reduction in material outgassing resulting from more efficient cooling. In Fig. 5.11, the optical power and voltage are shown to increase with the gas flow rate. While the addition of gas flow should remove heat from the discharge and increase the excimer intensity through convective cooling, a concomitant increase in nozzle gas pressure also occurs. Supersonic expansion of rare gas excimers has been found to increase the excimer intensity with a pressure dependence of P^2 [54]. In our case, we observe a much weaker dependence, suggesting that the main effect of flow is to reduce gas heating.

5.5 Series operation of microdischarges

Experiments in single capillary microdischarges suggest that gains in excimer emission intensity are limited despite the dependence on discharge current, gas pressure, and flow rate. An alternative scheme for intensifying the on-axis excimer emission is to fabricate aligned arrays of identical microdischarges as illustrated for the case of two discharges in Fig. 5.12. Operation of multiple discharges in series is achieved by adding voltage rather than current [46, 48]. Using the same voltage drop across each tube sustains a fixed current through the array. The current is adjusted for maximum excimer emission while minimizing heating problems for a single microdischarge. We tested this idea by introducing a tube segment between the cathode and the anode of a single microdischarge. The supply voltage was increased to permit two discharges to form: two identical plasma potentials must be maintained. Since the current is kept low, tip heating is not excessive and the plasma

expansion is not impeded. The total discharge volume is thus doubled. To determine the difference in excimer emission between a single-tube and dual-tube setup, the two discharges were operated sequentially. First, a single discharge ("discharge 1") was formed in tube 1 with the grid as the anode [Fig. 5.12(a)]; second, a single discharge ("discharge 2") was formed in tube 2 with tube 1 as the anode [Fig. 5.12(b)]; finally, both discharges were formed simultaneously with tube 1 floating and the grid as the anode [Fig. 5.12(c)]. Spectra, obtained at 1000 Torr and a constant current of 4 mA, are compared in Fig. 5.13. If each discharge had formed identically, we would have expected to obtain the same intensity for each individual discharge and twice the intensity for both. Overall results for optical power in the dual-discharge setup are shown as function of pressure in Fig. 5.14. It is evident that the excimer intensity is always higher for discharge 1, which was closer to the monochromator [compare Figs. 5.12(a) and 5.12(b)]. Since the solid angle for light collection is a function of the distance from the point source, it is possible that more of the emission is collected from discharge 1 than discharge 2. The excimer intensity of the dual discharge setup is approximately equal to the sum of the intensities from the individual discharges for pressures between 600 and 1350 Torr as confirmed in Fig. 5.14.

The additivity of excimer intensity from pre-aligned dual microdischarges--operated simultaneously at a current such that the intensity of a single discharge is maximum--suggests a scheme for fabricating a source of intense excimer radiation that could lead to a dc microexcimer laser. Similar segmented electrode designs have been used in argon ion lasers to extend the length of the discharge and achieve lasing [55]. The main difference here is the pressure regime necessary for excimer formation. At high pressures, gas heating is accelerated through a mechanism known as ohmic heating. This effect is described by the following equation [2]:

$$P_{ohm} = \frac{1}{2} J^2 \frac{m\nu_m}{e^2 n} \quad (5.3)$$

where P_{ohm} is the time-averaged power per unit area deposited by ohmic heating, J is the current density, m is the mass, ν_m is the electron-neutral collision frequency, e is the electron charge, and n is the plasma density. Ohmic heating is especially important at high pressures where the collision frequency is very high. In addition, the current density in a microdischarge is extremely large (more than 1 A/cm^2) because of the small spatial scale. Since lasing requires even higher input powers to achieve the necessary gain, solving the thermal problems remains a major challenge.

5.6 Summary

Excimer emission has been studied in high-pressure microdischarges formed in metal capillary tubes. The emission intensity from a single tube was found to increase linearly with discharge current at low powers. The intensity gains were limited at higher currents by gas heating which reduces plasma expansion and excimer formation. For argon, gas flow rate through the discharge intensified the emission by convective cooling. Larger amplification of the excimer intensity is achieved by increasing the plasma volume. We have designed a scheme for operating multiple discharges in series. For two discharges, the excimer intensity is shown to be additive which demonstrates potential for building a dc microlaser.

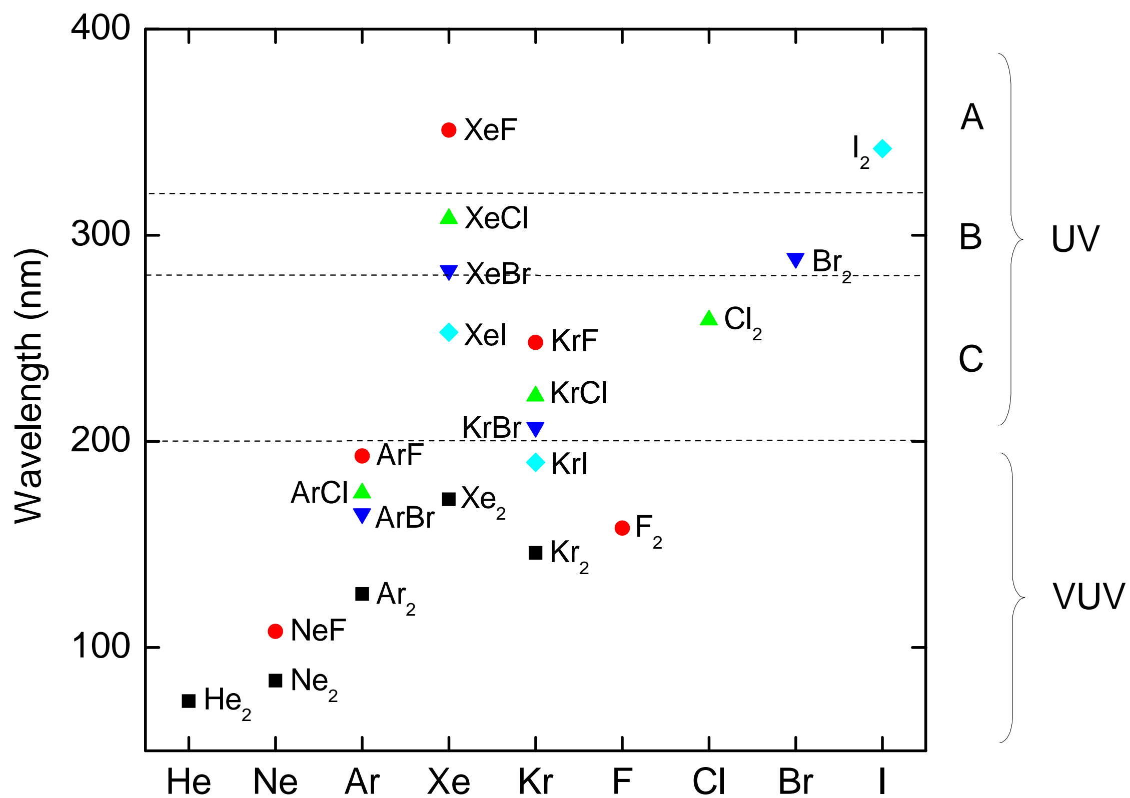

Figure 5.1. Emissive wavelengths of various excimer species. Also shown for reference are the wavelength ranges classified as UV A (320-400 nm), UV B (280-320 nm), UV C (200-280 nm), and VUV (below 200 nm).

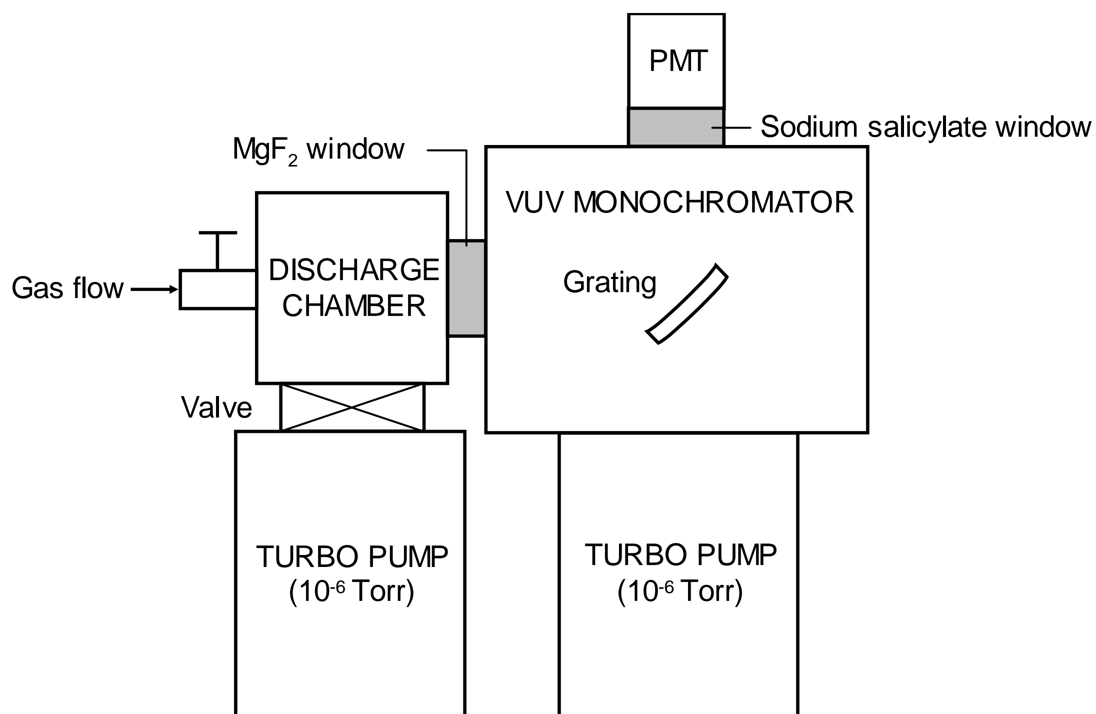

Figure 5.2. Setup for vacuum ultraviolet spectroscopy including discharge chamber, monochromator, and photomultiplier tube (PMT). Light from discharge is transmitted through a magnesium difluoride window onto the grating in the monochromator. Intensity of the spectrally resolved radiation is obtained with a sodium salicylate scintillator and PMT.

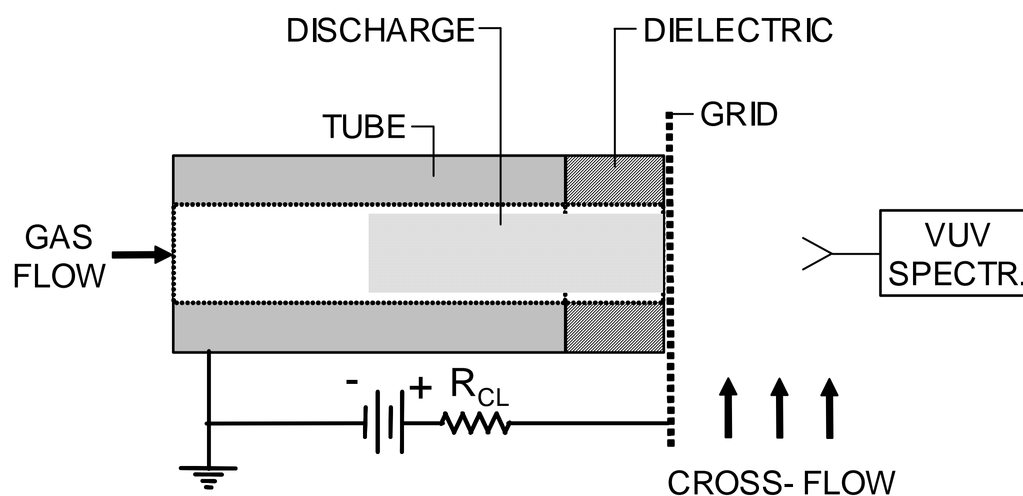

Figure 5.3. Schematic of the microdischarge setup (not to scale). The device consists of a stainless steel capillary tube (cathode), a metal grid (anode) and a sapphire spacer washer. VUV spectra were collected from the anode side. Connection to the DC power supply was through a current limiting resistor (R=100 kΩ).

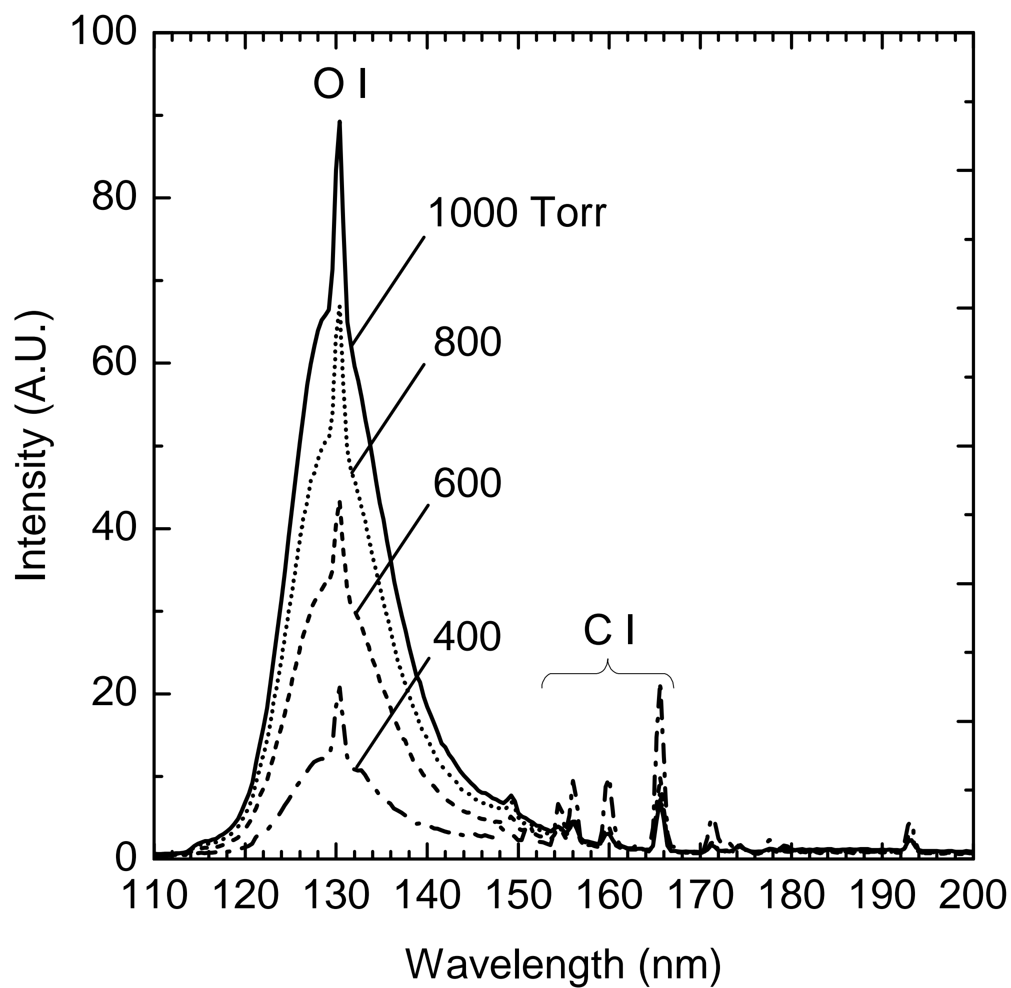

Figure 5.4. VUV emission spectra of Ar microdischarge in a cathode tube (i.d.=180 μm) as a function of the ambient gas pressure. The discharge current was held constant at 4 mA. O I and C I refer to lines corresponding to atomic oxygen and carbon states (impurities).

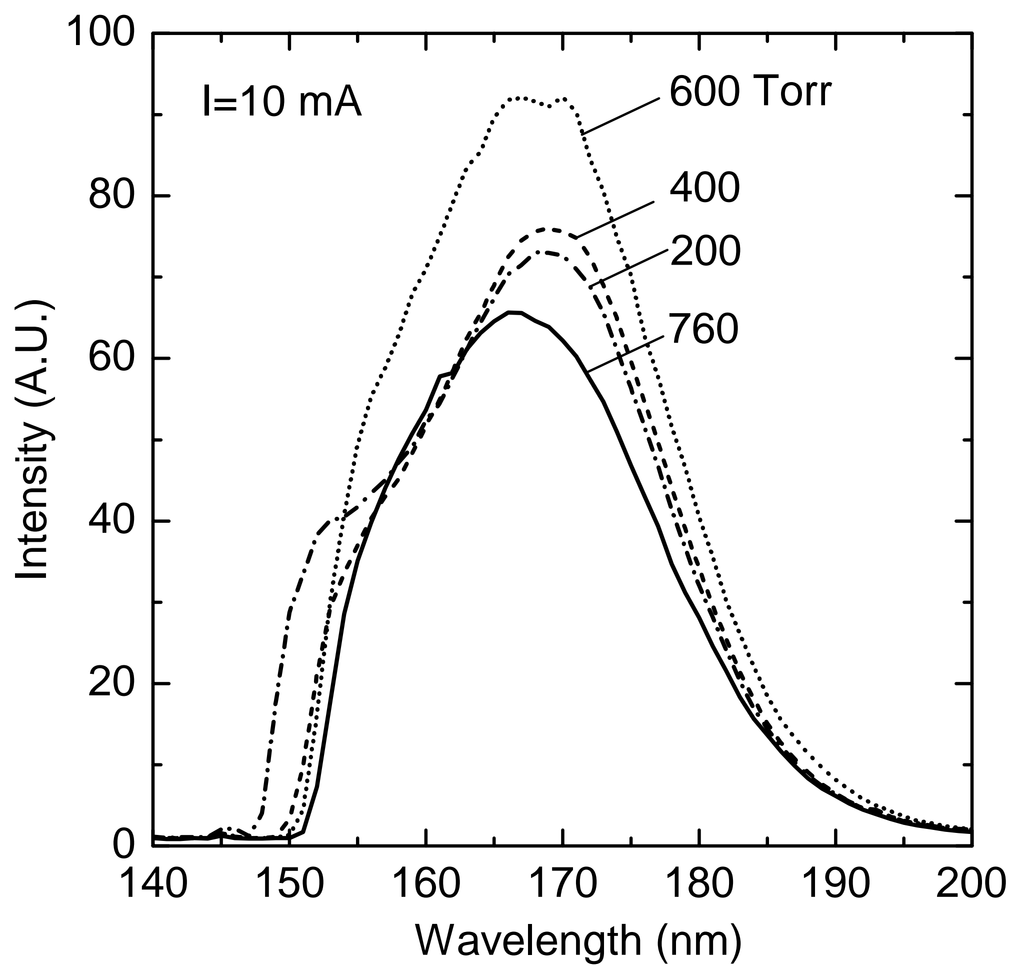

Figure 5.5. VUV emission spectra of Xe microdischarge in a cathode tube (i.d.=180 μm) as a function of the ambient pressure. Discharge current was kept constant at 10 mA.

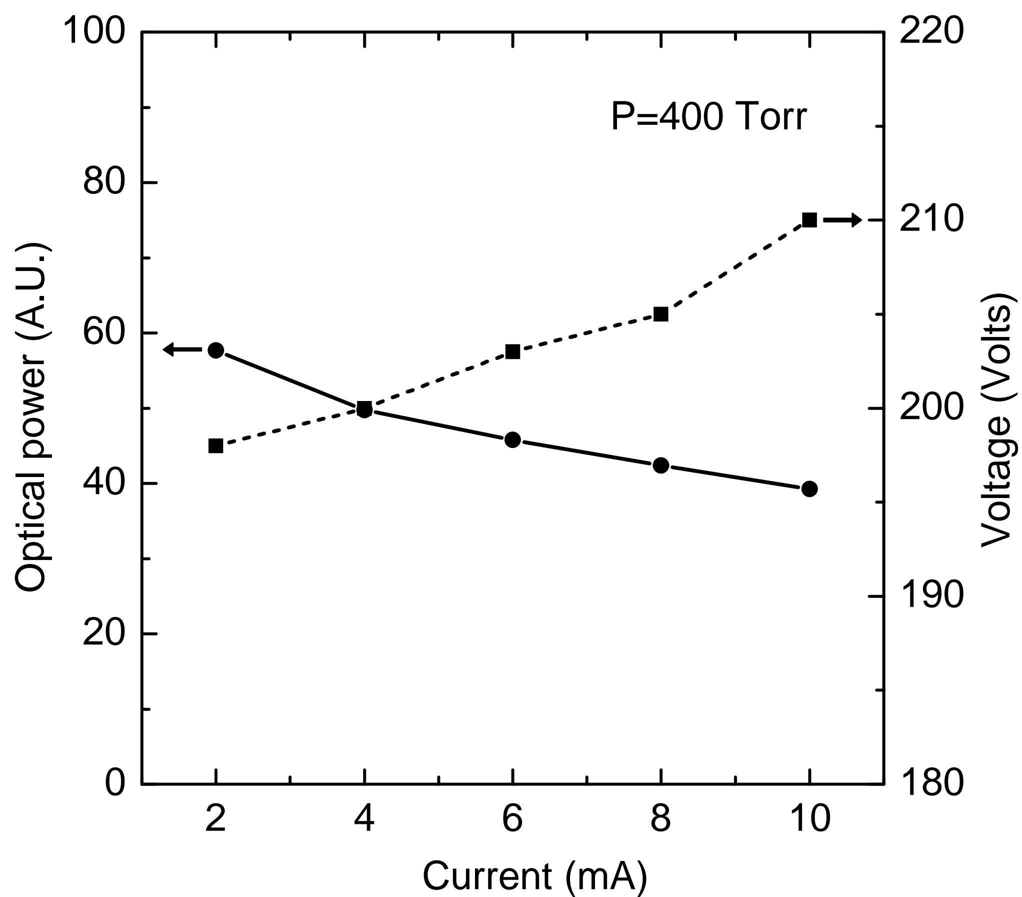

Figure 5.6. VUV optical power and discharge voltage as a function of current for Ar microdischarge in cathode tube (i.d.=180 μm) at 400 Torr.

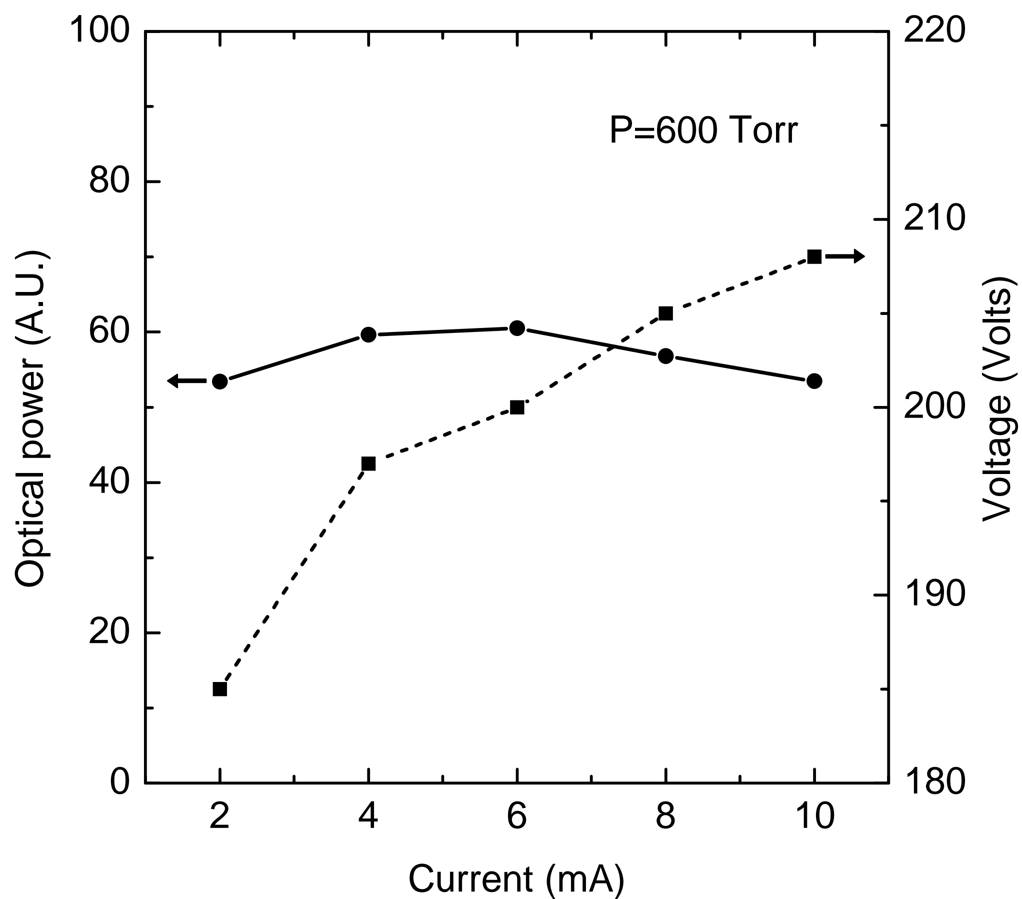

Figure 5.7. VUV optical power and discharge voltage as a function of current for Ar microdischarge in cathode tube (i.d.=180 μm) at 600 Torr.

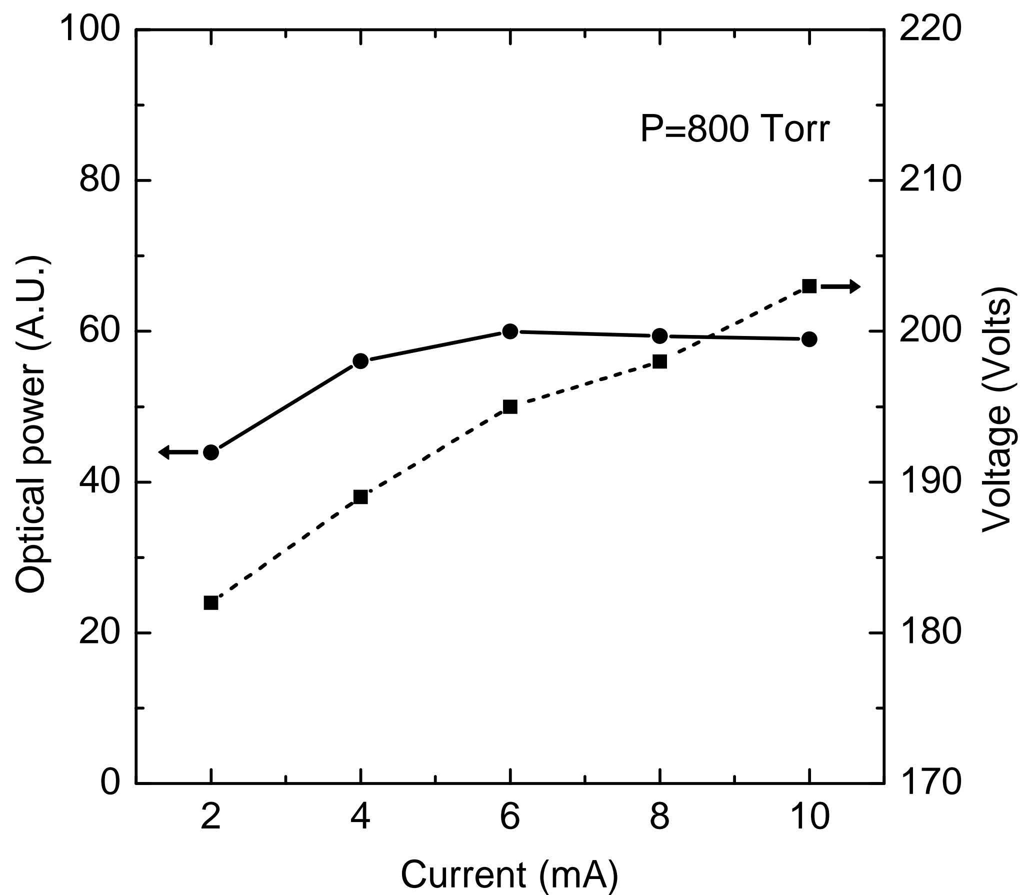

Figure 5.8. VUV optical power and discharge voltage as a function of current for Ar microdischarge in cathode tube (i.d.=180 μm) at 800 Torr.

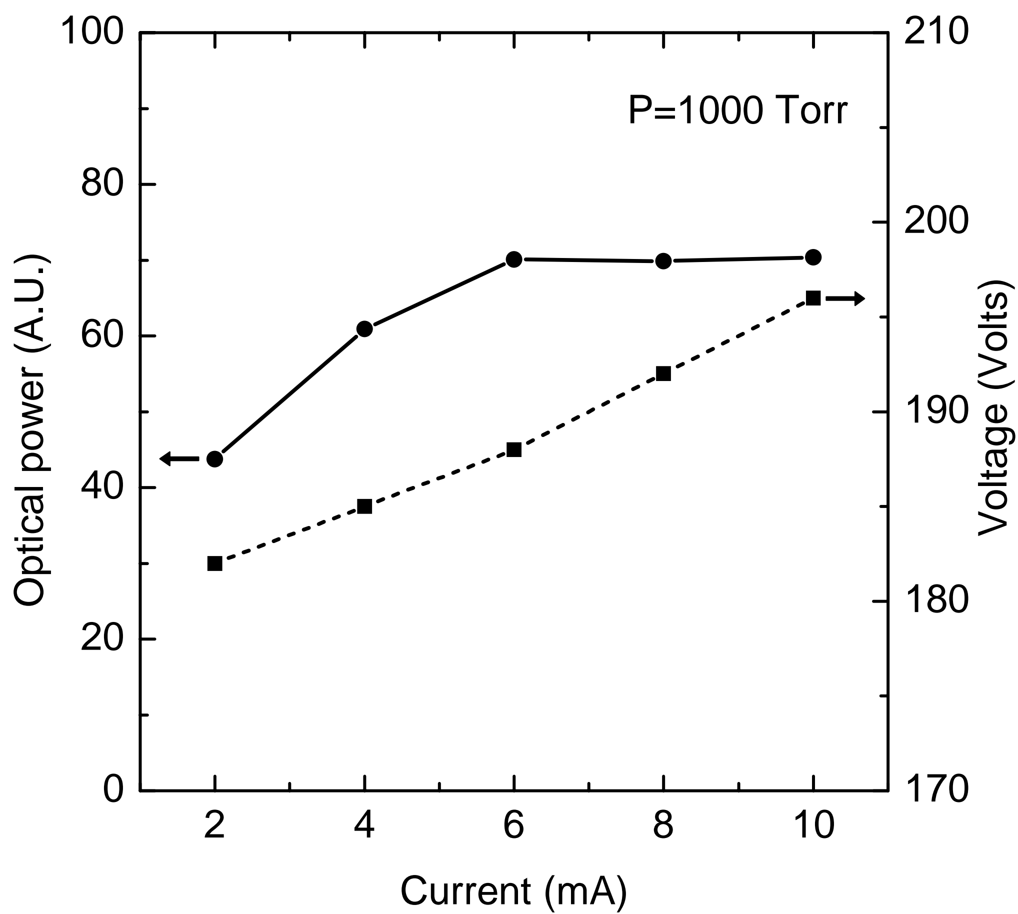

Figure 5.9. VUV optical power and discharge voltage as a function of current for Ar microdischarge in cathode tube (i.d.=180 μm) at 1000 Torr.

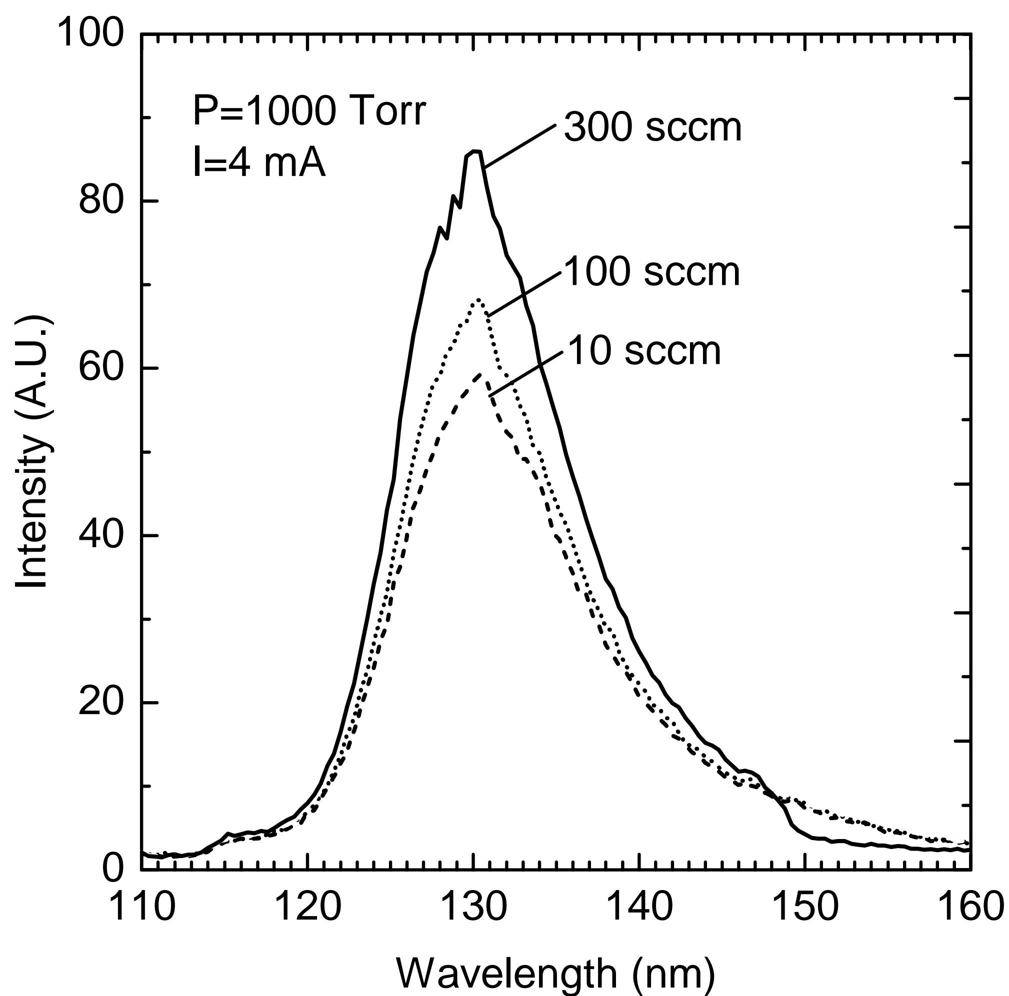

Figure 5.10. Argon excimer emission spectra of microdischarges with gas flown through the cathode tube at the indicated flow rates. Ambient gas pressure and discharge current `were kept constant at 1000 Torr and 4 mA, respectively.

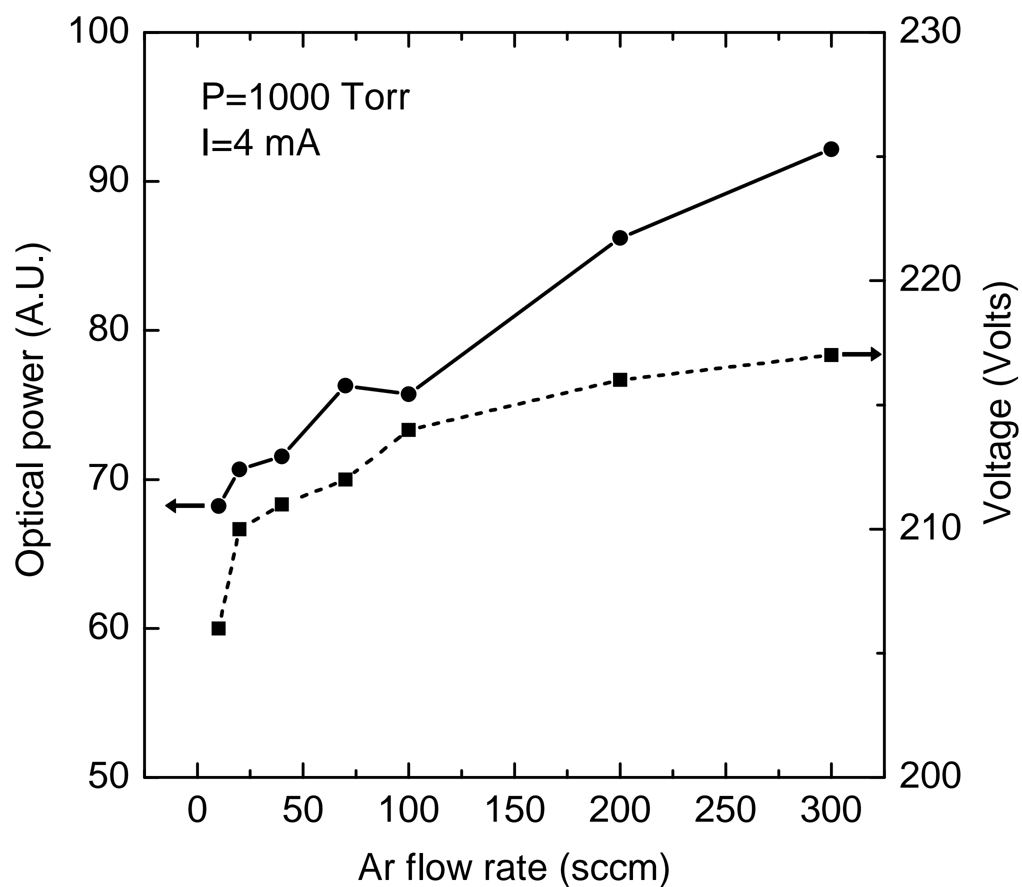

Figure 5.11. VUV optical power and discharge voltage as a function of Ar flow rate through the cathode tube. Ambient pressure and discharge current were kept constant at 1000 Torr and 4 mA, respectively.

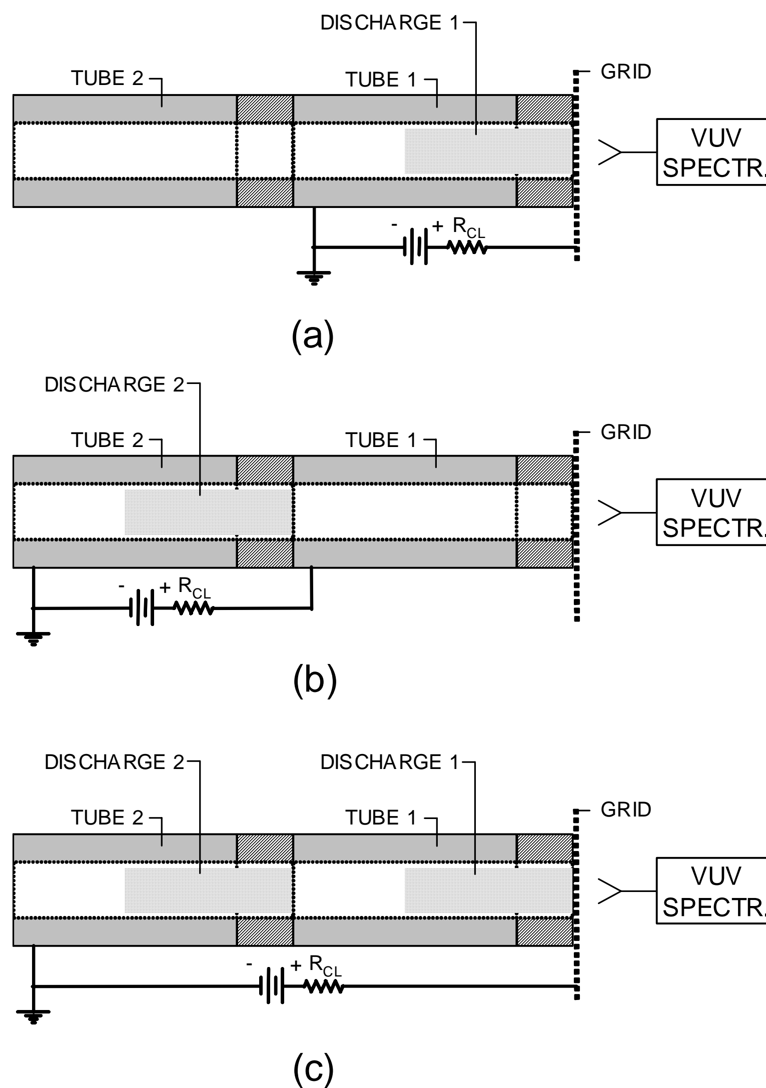

Figure 5.12. Schematic diagram of dual-tube setup for operation of microdischarges in series. Experiments were conducted in the following sequential fashion: (a) discharge 1 is formed in tube 1 with the grid as the anode, (b) discharge 2 is formed in tube 2 with tube 1 as the anode, (c) discharge 1 and 2 are formed simultaneously with tube 1 floating and the grid as the anode.

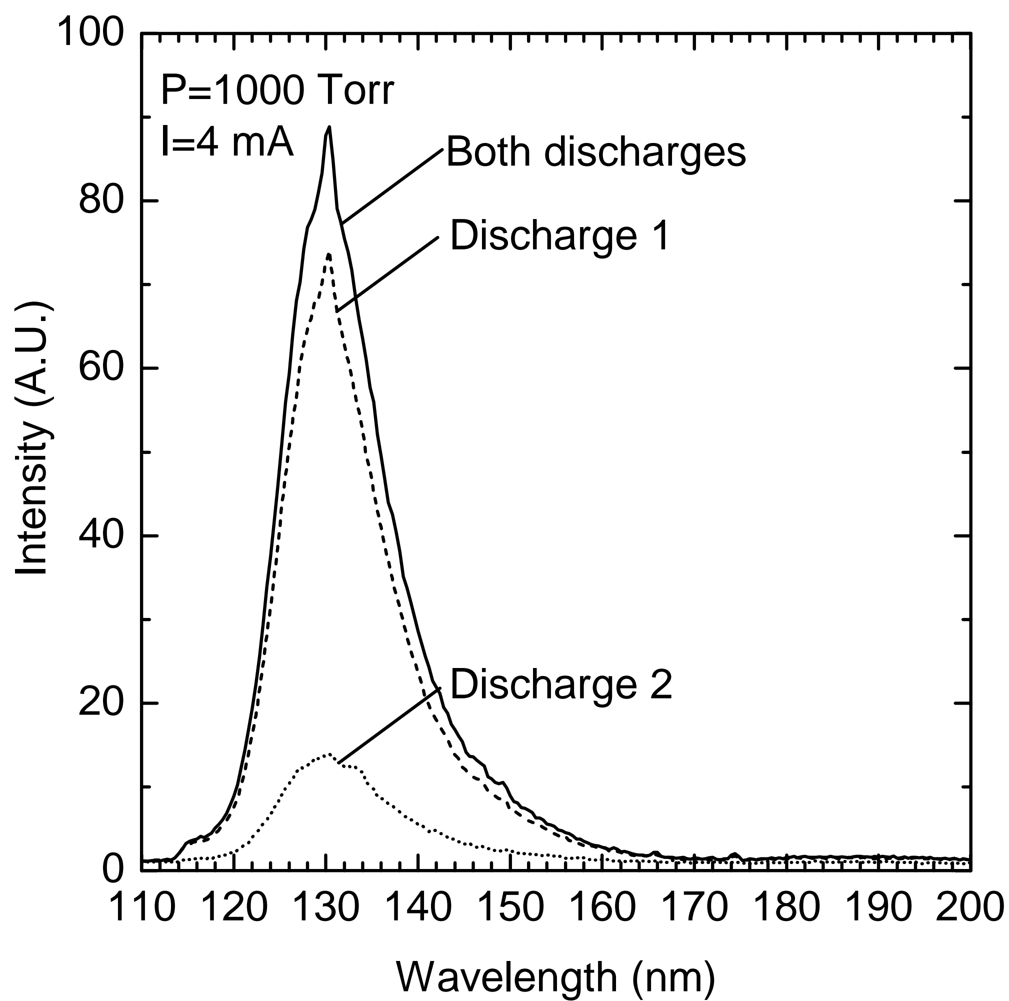

Figure 5.13. Argon excimer emission spectra from single-tube and dual-tube microdischarges operated in a sequence depicted in Fig. 5.12. The single-tube discharges were each operated at a current of 4 mA and voltage of 210 V; simultaneous operation of the dual-tube was obtained at a current of 4 mA and voltage of 420 V.

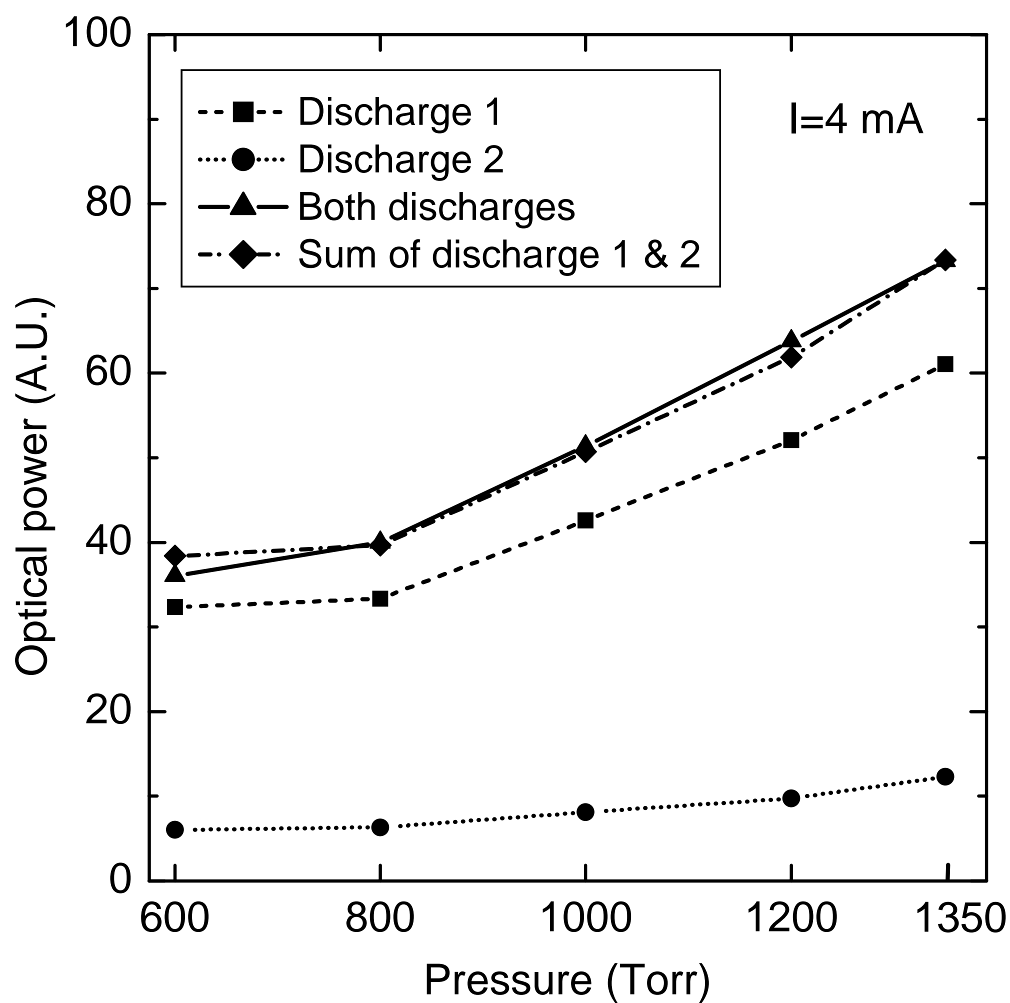

Figure 5.14. VUV optical power from single-tube and dual-tube microdischarges as a function of pressure. The single-tube discharges were each operated at a current of 4 mA and voltage of 210 V; simultaneous operation of the dual-tube was obtained at a current of 4 mA and voltage of 420 V.

Chapter 6

NANOPARTICLE SYNTHESIS IN SHORT-RESIDENCE TIME MICROREACTORS

6.1 Introduction

Materials synthesis at the nanoscale (e.g. nanoparticles) has attracted a great deal of interest because of unique electronic, magnetic, and optical properties at these length scales. Reducing the size of semiconductor crystals, for example, leads to an increased optical band gap and size-dependent light emission [56, 57] which is desirable for applications in advanced optoelectronic devices. Silicon is of particular interest since it is the most important material in the semiconductor device industry. Although bulk Si, characterized by an indirect band gap, is not capable of emitting light efficiently, room temperature visible photoluminescence (PL) has been observed in porous Si [58] and from nanoparticles with diameters less than 5 nm [59]. PL emission from Si nanoclusters has been theorized to occur through two main mechanisms: quantum confinement of electron-hole pairs (excitons) [60] and surface-related processes [61]. While theoretical studies have attempted to elucidate the underlying physics of PL [61, 62], experimental discrepancies still remain. The challenge for experimental investigation of silicon nanoparticles is the development of a synthesis route with precise control over the size, distribution, and chemical composition of Si nanoparticles.

Silicon nanoparticles (np-Si) have been produced using a variety of techniques including colloidal growth [63-66], aerosol processes [60, 67-75], plasma synthesis [76, 77] and electrochemical etching [78, 79]. Gas-phase synthesis is generally preferred because of the high-purity that can be achieved and compatibility with solid state device manufacturing. Drawbacks of aerosol methods are broad size distributions that necessitate post-synthesis size-selection [69, 74] and particle agglomeration [80]. Figure 6.1 illustrates a simplified picture of the processes that govern the growth dynamics of nanoparticles in an aerosol flow reactor [80]. The steps described occur at different time scales and locations in the reactor. Initial nucleation of particles results from the formation of a supersaturated vapor of gas precursors. Possible means of generating a vapor source include pyrolysis [60, 67, 68, 70, 75], laser ablation [73, 74], spark ablation [69], and plasmas [71, 72]. In the early stages, particles grow by condensation of vapor at their surface and coalescent coagulation. Normally, these processes occur in a region near the vapor source where the temperature is high. As the particle concentration increases, collisions between particles become more frequent and agglomeration begins. Formation of these undesirable aggregates is usually found away from the vapor source as the temperature drops off. In order to grow dense, unagglomerated nanoparticles, the nucleation, growth, and coagulation of particles must be controlled by limiting the time scales of the relative steps. In this chapter, we demonstrate the ability of microdischarges to function as short-residence time reactors for the synthesis of nanoparticles. Because of the small spatial scale of our source, particle growth is limited in the reaction zone allowing the production of ultrasmall nanoparticles (1-2 nm) with relatively narrow size distributions. The luminescent properties of our np-Si suggest potential applications in optical devices and fundamental studies to clarify the luminescence mechanism.

6.2 Aerosol synthesis and characterization

A generic experimental setup for nanoparticle synthesis using a direct-current (dc), atmospheric-pressure microdischarge is schematically shown in Fig. 6.2. The discharge is formed in a stainless steel capillary tube cathode (i.d.=180 μm) and extends towards a metal tube anode (i.d.=1 mm). Electrodes were pressure sealed inside a Pyrex glass tube, separated by a gap of 0.5 to 2 mm which could be adjusted using a micrometer. Typical voltages and currents used to strike and sustain the discharge were 0-1000 V and 3-10 mA. The gas precursor for particle synthesis was diluted in an inert gas such as argon and flowed through the cathode. In the case of np-Si, 1 to 5 ppm of silane was introduced into the discharge by varying the flow rate of a 50 ppm SiH_4/Ar mixture (electronic grade, Matheson Tri-Gas) while maintaining a constant total flow rate with a balance of argon. Outside of the cathode, a flow of gas approximately three times larger than through the discharge was applied to reduce coagulation downstream of the plasma reaction zone. To insure complete removal of oxygen, the inert gas, research purity argon (99.9995%), was run through a copper getter gas purifier heated to 350 ^{o}C before flowing into the reactor.

Vapor-phase synthesis of nanoparticles enables coupling of the reactor setup with aerosol instrumentation that measures the size and distribution of particles *in situ*. Size-classification was performed using a radial differential mobility analyzer (RDMA) [81, 82]. As shown in more detail in Fig. 6.3, the instrument is a capacitor in which charged aerosol particles migrate in an electric field across a laminar flow of sheath gas. The aerosol stream enters the RDMA at a position on the outer radius and flows inward towards the center where the classified aerosol is collected. The particle size measurement is based on their electrical mobility in the carrier gas and thus, corresponds to the projected area of the

aerosol particles. For a given voltage, particles within a narrow range of mobilities transverse the gap between the electrodes and are extracted by a sampling orifice opposite to the aerosol inlet. Particles with higher mobilities deposit on the bottom electrode. Particles with too low mobility are carried out with the excess sheath gas flow. By varying the voltage, particles of different mobilities are transmitted through the instrument. The concentration of classified nanoparticles is measured by flowing the aerosol into an electrometer. Combined operation of the RDMA and electrometer allows determination of the nanoparticle size distribution.

To impart a known charge distribution on particles, the aerosol is normally passed through a bipolar charger (sealed ^{85}Kr-β source), commonly referred to as a "neutralizer," before entering the RDMA [69]. For particles in the size range explored here, the neutralizer was found to cause growth by agglomeration, perhaps because of its large volume (100 mls). Figure 6.4 shows size distributions of np-Si grown in the microdischarge and classified by the RDMA with and without a neutralizer in-line. When a neutralizer was used, the measured size distribution appeared broad with an extended tail indicating a coagulated aerosol. A narrower size distribution with a smaller mean diameter was obtained by removing the neutralizer and collecting plasma-charged particles directly. The residence time for particle growth in the microdischarge is estimated to be on the order of 1 millisecond. At an aerosol flow rate of 600 sccm, the neutralizer increases the residence time to 10 seconds, artificially causing broadening. Shortening the residence time of particles between the reactor and size classifier should be a more accurate representation of the distribution of particles synthesized in our process.

Size distributions of np-Si synthesized in the microdischarge and classified by the RDMA are shown in Fig. 6.5. The orientation of the electric field in the RDMA for these

experiments was such that positively charged particles are transmitted. In the range of silane concentrations explored here, the discharge was stable with highly reproducible size distributions. Below a silane concentration of 1 ppm, particles could not be detected, presumably because they were smaller than the 2.5 nm detection limit of the present RDMA. As the silane concentration was raised from 2.5 to 4.0 ppm, the mean particle size increased and the size distribution broadened significantly. Fitting to the following log-normal distribution [83] provided estimates of the geometrical mean diameter (D_g) and geometrical standard deviation (σ_g):

$$\frac{dN}{d\ln D_p} = \frac{N}{(2\pi)^{1/2}\ln\sigma_g}\exp\left(-\frac{(\ln D_p - \ln D_g)^2}{2\ln^2\sigma_g}\right) \tag{6.1}$$

where N is the total aerosol number concentration, and D_p is the mean diameter. Regression to the log-normal distribution was performed using a software package (Igor Pro v. 4.0) with D_g and σ_g as the fitting parameters and are shown in Fig. 6.6. The particle distributions are closely approximated by the log-normal fit, but exhibit a tail at larger diameters. At a silane concentration of 2.5 ppm, D_g and σ_g were found to be 2.9 nm and 1.32, respectively. The observed σ_g compares favorably with values measured by other growth processes without size-selection which were reported to be 1.5-1.6 [69, 71, 72, 84, 85]. Increasing the silane concentration to 4.0 ppm increased D_g and σ_g to 6.2 nm and 1.45, respectively. The increasing value of σ_g at higher silane concentrations may indicate the onset of particle growth by agglomeration.

6.3 Particle charging

Charged particles of both polarities could be measured by alternating the orientation of the electric field in the RDMA. In Fig. 6.7, size distributions of charged np-Si grown in the microdischarge are shown. The presence of positively and negatively charged particles is not surprising since particles can acquire charge in a plasma from ions and electrons. Most objects placed in a plasma charge negatively as a result of the higher mobility of electrons. The mobility of charge carriers in a plasma is given by:

$$\mu = \frac{|q|}{m\upsilon_m} \tag{6.2}$$

where μ is the mobility constant, q is the charge, m is the mass, and ν_m is the momentum transfer frequency. It is the large mass difference between ions and electrons that leads to a difference in mobility. Charging of small particles, less than 3 nm in diameter, is complicated, however, by statistical fluctuations [86]. Note that in our case more positively charged particles are detected (Fig. 6.7) at both the low and high silane concentration. This is consistent with Si cluster nucleation in low-pressure discharges where photo-detachment studies found very little negative charge on crystallites smaller than 2 nm [87]. Large particles ($\geq$10 nm) charge up negatively in a plasma as a result of the larger electron mobility. Thus, observation of both charge polarities corroborates the existence of very small particles.

Remarkably, the peak number density for each charge polarity does not change appreciably with silane concentration. This suggests that the particle density exceeds that of

ions and electrons in the discharge available for attachment and the particles must be at most singly charged. Particles in this size range are not likely to carry multiple charges. Figure 6.8 illustrates the charging probability of particles passed through a neutralizer where negative and positive ions are responsible for charging. The results are obtained by approximating an empirical expression of the Fuchs model [88]. It is apparent that particles less than 10 nm in diameter have a very low probability of acquiring more than a single charge, supporting our observations. Since the RDMA measures particle mobility which is a function of size and charge, the existence of only singly charged particles signifies that the distributions are reflective of the particle size.

6.4 Characterization of silicon nanoparticles

Particles were collected either on a substrate or in liquid without size-selection for characterization by transmission electron microscopy (TEM), atomic force microscopy (AFM), micro-Raman spectroscopy, and energy dispersive X-ray spectroscopy (EDS). Particles were deposited onto carbon-coated copper TEM grids by flowing the aerosol stream into an electrostatic precipitator [81]. Films of particles were obtained by placing a molybdenum substrate in the microreactor in a stagnation flow geometry with the microdischarge. Dispersions of particles in a solution phase were obtained by bubbling the aerosol stream through a glass frit into a solvent that was outgassed for 1-2 hours [67]. We used 1-octanol for its low volatility and since it has been shown to stabilize silicon particles [65, 89]. After collecting particles for 24 hours, the solvent was removed by vacuum evaporation and the particles were redispersed in hexane.

A bright-field TEM image of np-Si deposited from the microdischarge is shown in Fig. 6.9. The image shows the presence of large aggregates more than 10 nm in size. Since structures of this size were not observed in the RDMA, we suspect that agglomeration occurred during the deposition process. The aggregates appear to be made up of smaller spherical particles approximately 5 nm in diameter. These primary particles appear to be uniform in size, consistent with the narrow size distributions obtained using the RDMA. Electron diffraction (see inset of Fig. 6.9) is characteristic of an amorphous material. Since the samples were exposed to air during loading into the TEM, oxidation of the particles may have occurred, preventing the preservation of the crystalline core. It has been previously reported that for particles in this size limit (less than 4 nm), crystal structure is difficult to observe because the surface energy is higher than the lattice energy [73]. The formation of a silicon oxide shell could also be responsible for the larger particle sizes observed by TEM.

AFM was used to determine the size of np-Si in hexane solution by evaporating a drop of the dispersion on a crystalline Si wafer. Diluting the dispersion appropriately allowed particles to be well isolated as shown in Fig. 6.10(a). The particles were sized by measuring the height of approximately 500 particles. From the histogram in Fig. 6.11(b), the mean particle height is calculated to be 1.6 nm. Particles as small as 1.0 nm and as large as 6.6 nm were also observed.

To characterize the chemical nature of our np-Si, thin films were deposited on substrates. Figure 6.11(a) illustrates a micro-Raman spectrum of a np-Si film deposited on molybedenum for 1 hour. The peak corresponds to the sum of two Gaussian peaks at 477 cm^{-1} and 507 cm^{-1} attributed to amorphous silicon, a-Si:H, and grain boundaries in nanocrystalline silicon films, respectively [90]. This spectrum was compared to that of a crystalline silicon substrate which showed a single sharp peak at 519 cm^{-1} [see Fig. 6.11(a)].

The broad shape of the peak as well as the shift from crystalline Si confirms that deposited films are amorphous and made up of nanoparticles [91]. Analysis by EDS confirmed that the films consist of only silicon and oxygen, as depicted in Fig. 6.11(b). Peaks from the molybdenum substrate were also evident but no other contaminants were detected.

6.5 Photoluminescence spectroscopy

The size-dependent shift of the band gap in np-Si makes optical characterization an important probe of the particle properties. The emission of particles is especially relevant for technological applications. We have performed photoluminescence (PL) measurements at room temperature on both colloidal samples and np-Si films. For hexane-suspended np-Si, the PL excitation and emission spectra were obtained using a spectrophotometer (Photon Technology International, Model QM). Figure 6.12 illustrates spectra from np-Si grown with the 2.5 ppm silane stream. The spectra exhibit an excitation peak at 360 nm (dashed line) and an emission maximum at 420 nm (solid line). The strong blue emission was readily observable by the naked eye. Also shown is the UV-visible absorbance spectrum (dotted line). The yellow absorption tail corresponds to the indirect gap of bulk Si [64, 67]. Some of the features in the spectrum, including the peak at approximately 320 nm, have also been reported for 2.0 nm Si colloids and attributed to a higher energy, direct transition [64]. It is apparent that the absorption edge and excitation peak are at similar energies, while the emission peak is red-shifted. In general, the absorption gap in np-Si has been found to be larger than the emission gap. When light is absorbed, the particle undergoes an electronic excitation in which an electron-hole pair (exciton) is formed. Recombination of the electron

and hole by emission of a photon occurs at a lower energy because of structural relaxation processes in the particle [92]. The difference between the absorption and emission energy is known as the Stokes shift [92]:

$$E^{Stokes} = E^{absorption} - E^{emission} \tag{6.3}$$

where $E^{absorption}$ is the energy required to excite the cluster from its ground state to the lowest excited state, $E^{emission}$ is the energy released during recombination, and E^{Stokes} is the Stokes shift. From Fig. 6.12, the $E^{absorption}$, $E^{emission}$, and E^{Stokes} for our np-Si are approximately 3.4 eV, 2.9 eV, and 0.5 eV, respectively. The shift of the optical gap from the bulk value for Si of 1.12 eV represents the effect of quantum confinement. Assuming that the PL emission at 420 nm (2.9 eV) is excitonic, the silicon particle core size can be estimated from calculations to be less than 2 nm [61, 62]. This size is close to the AFM result but significantly smaller than the RDMA measurement. The size discrepancy could be related to smaller particle agglomeration in the aerosol measurements or larger particle oxidation upon exposure to ambient air. We note that particles grown at higher silane concentrations, which appear to be bigger according to the RDMA, do not exhibit red-shifted PL peaks as expected from quantum confinement. We hypothesize that the short residence time in the microreactor limits the primary particle size in the 1-2 nm range. Larger silane concentrations result in the production of more particles in the same size range which subsequently grow by agglomeration.

The emission spectra of np-Si in hexane are strongly dependent on the excitation wavelength as shown in Figure 6.13. Although excitation at 370 nm resulted in the

maximum PL emission, luminescence was observed at other excitation wavelengths. As the excitation was increased from 300 to 400 nm, the emission peak shifted from 370 to 450 nm. Exciting at 500 nm resulted in virtually no visible emission. The PL shift as a function of excitation wavelength is caused by the size distribution in the sample. At longer wavelengths, larger particles with lower HOMO→LUMO band gap energies are excited and the emission peak red-shifts [93, 94]. At wavelengths longer than 500 nm, the excitation energy is insufficient to excite any of the particles in the sample. As before, we can calculate the Stokes shift as a function of the excitation wavelength:

Table 6.1. Emission energy and Stokes shift as a function of excitation energy for np-Si in hexane.

Excitation energy (eV)	Emission energy (eV)	Stokes shift (eV)
4.12	3.34	0.78
3.86	3.25	0.61
3.43	2.94	0.49
3.09	2.75	0.34
2.47	2.38	0.10

As the excitation energy is decreased, emission is obtained from larger particles in the sample. Therefore, the observed decrease in the Stokes shift can be inferred to be related to particle size. Calculations have previously shown a similar trend approximated by $E^{Stokes} \sim D^{-n}$ with the Stokes shift becoming independent of the size of the cluster at diameters larger than 3 nm [92]. Because this parameter is related to a relaxation mechanism in the particle, it depends on specific bonds at the surface. For larger particle diameters, surface states have

been observed to be inconsequential to PL emission [61]. The sensitivity of the Stokes shift to particle size suggests that we are producing 1-2 nm np-Si. Particles in this size range have important implications in studies of the PL mechanism [61, 62, 66].

PL spectra of np-Si thin films were acquired using a GaN laser (405 nm) and collecting the emission with a 27.5 cm focal length grating spectrograph equipped with a cooled charge-coupled device detector. A representative spectrum, plotted in Fig. 6.14 (dashed line), exhibits a peak at 511 nm. The considerable red-shift from 420 nm for the hexane suspended np-Si may be a result of: a) uncontrolled oxidation of the directly deposited np-Si, or b) the excitation at the longer wavelength. To distinguish the effect of the latter, a PL spectrum of the hexane-suspended np-Si was compared at the same excitation wavelength of 405 nm. This spectrum (Fig. 6.14, solid line) shows a PL peak at approximately 465 nm, smaller than that seen for the directly deposited np-Si films. Based on the work of Puzder *et al.* [62], we attribute the difference to surface oxidation of the films. Exposure to oxygen can create surface states that produce defect levels and close the optical gap [61, 62]. Apparently, the octanol-capped nanoparticles suspended in hexane are protected from oxidation.

6.6 Summary

Atmospheric-pressure microdischarges have been used as short-residence time microreactors for the synthesis of nanometer-size silicon particles. Gas flow of SiH_4/Ar mixtures through the microdischarge nucleates particles which grow to a few nanometers in diameter before their growth is quenched in the short afterglow. The charged aerosol

particles were size classified on-line with a radial differential mobility analyzer (RDMA). The electrical mobility measurements showed relatively narrow size distributions of particles and aggregates in the 2-5 nm range with σ_g = 1.3 to 1.5. Positively and negatively charged particles were detected by the RDMA with a slightly lower concentration of the latter. Samples collected in solution exhibited strong PL emission with a peak at 420 nm, indicative of particles with a core size smaller than 2 nm. Silicon particles in this size range are of interest for fundamental studies of PL and optoelectronic applications. This synthetic route should be easily adaptable to grow a range of metal and semiconductor nanoparticles.

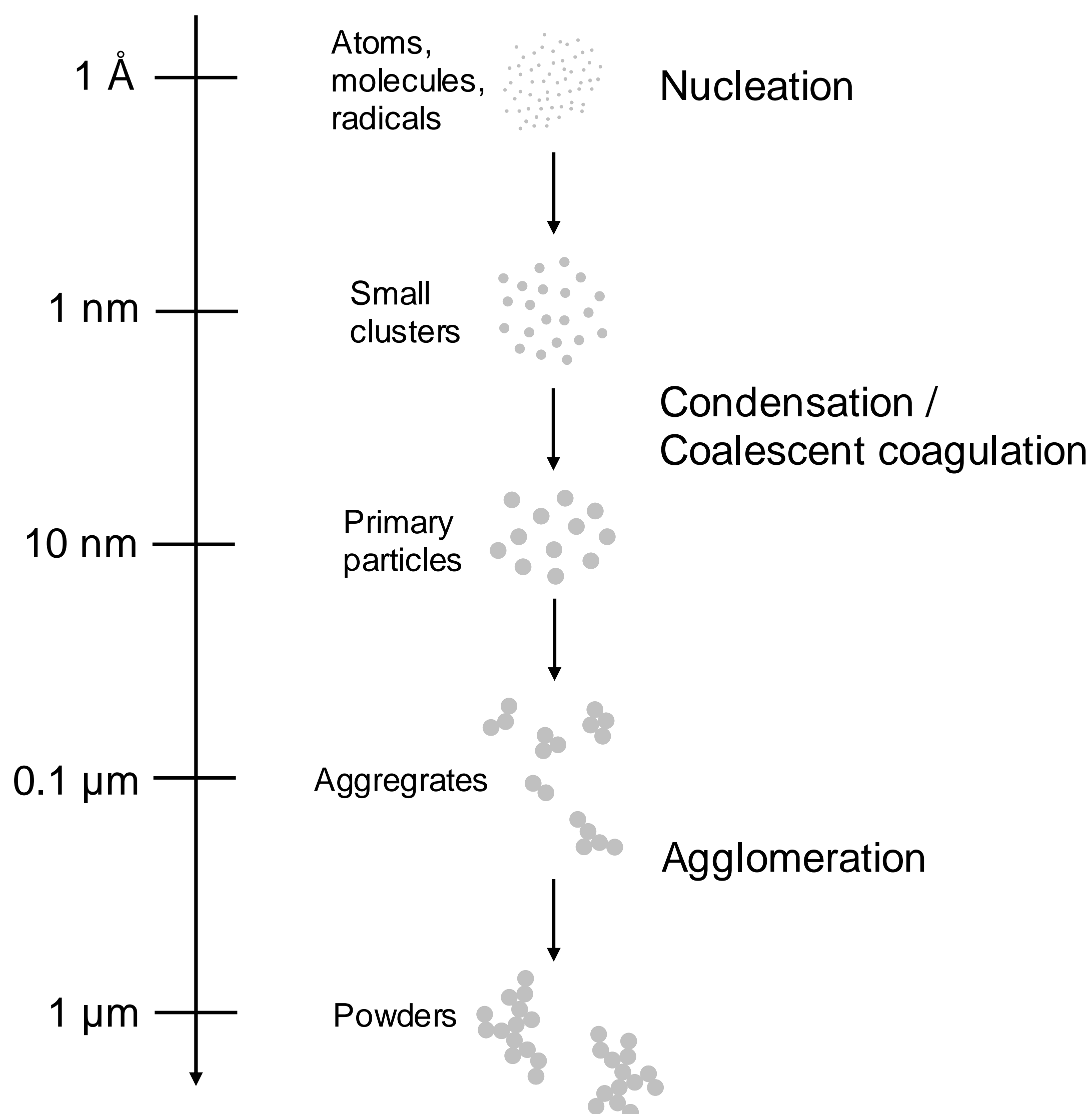

Figure 6.1. Illustration of processes involved in the formation and growth of particles from the vapor phase.

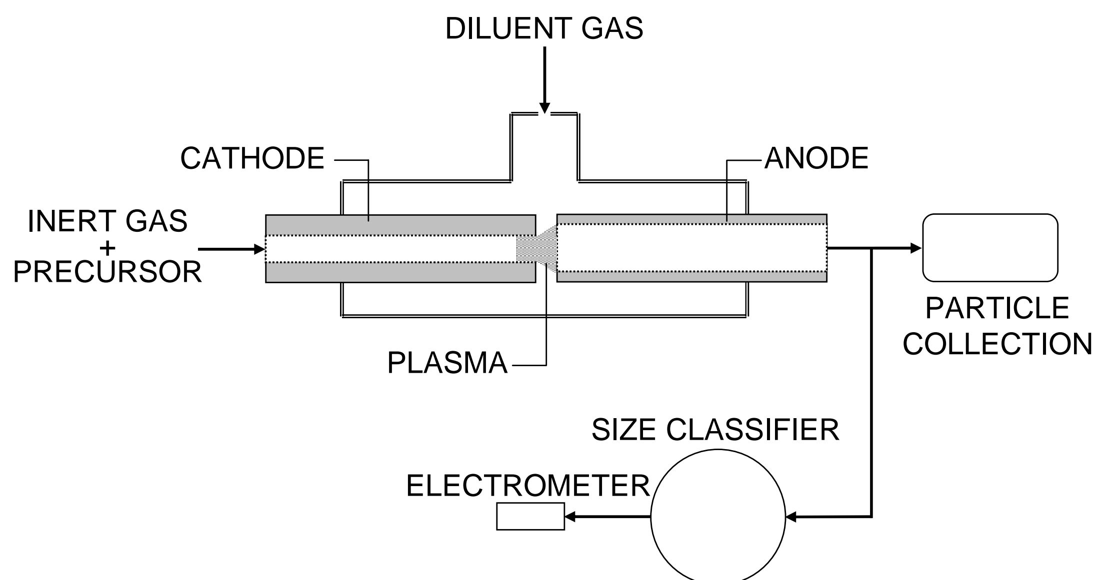

Figure 6.2. Schematic diagram of microdischarge reactor for synthesis of nanoparticles. Particles are analyzed *in situ* using a radial differential mobility analyzer (RDMA) to determine size and concentration. Particles are collected for optical characterization by depositing onto substrates using an electrostatic precipitator (ESP) or bubbling aerosol stream into a liquid.

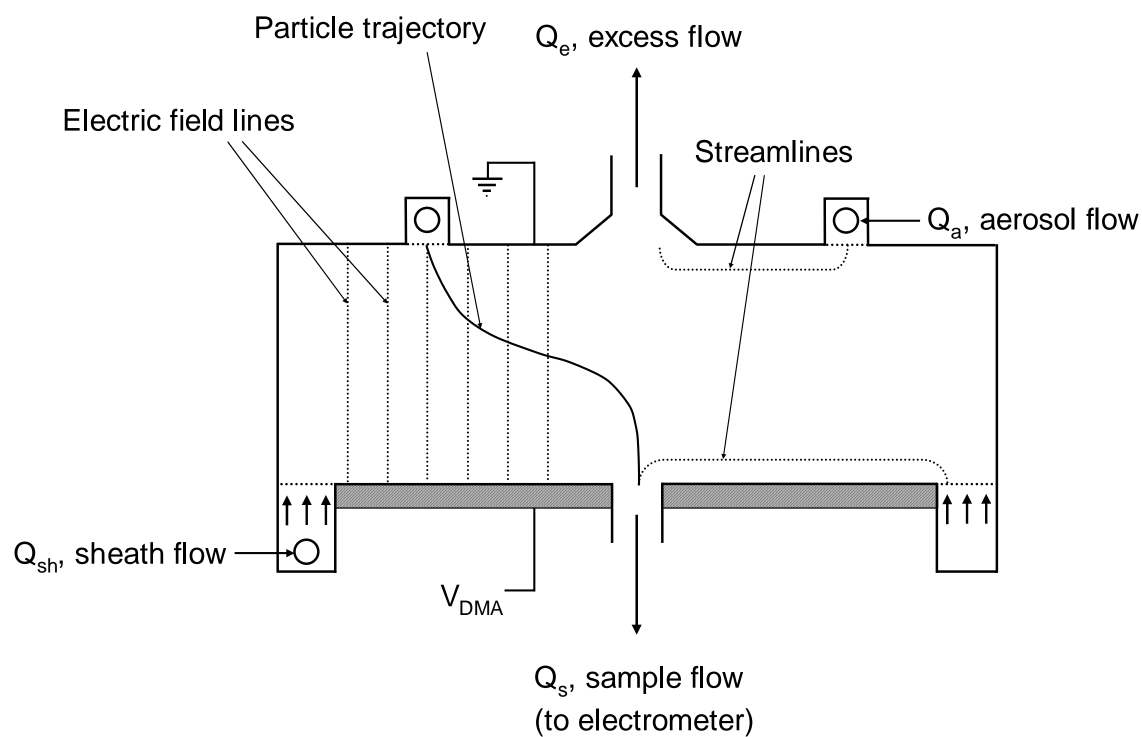

Figure 6.3. Schematic cross section of radial differential mobility analyzer (RDMA) [81, 82]. Typical values of Q_a, Q_{sh}, Q_s, and Q_e were 600 sccm, 5.5 slm, 600 sccm, and 5.5 slm, respectively.

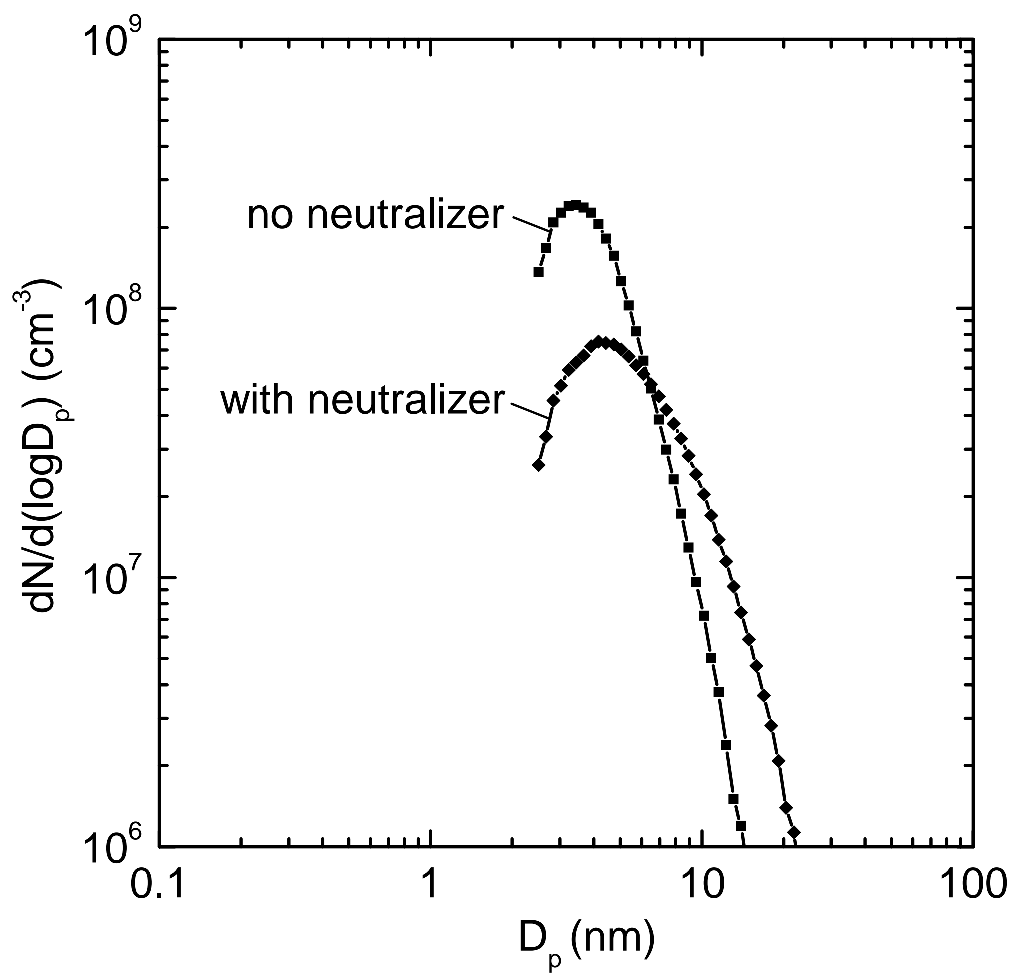

Figure 6.4. Particle size distributions of np-Si classified by RDMA with and without a neutralizer in-line.

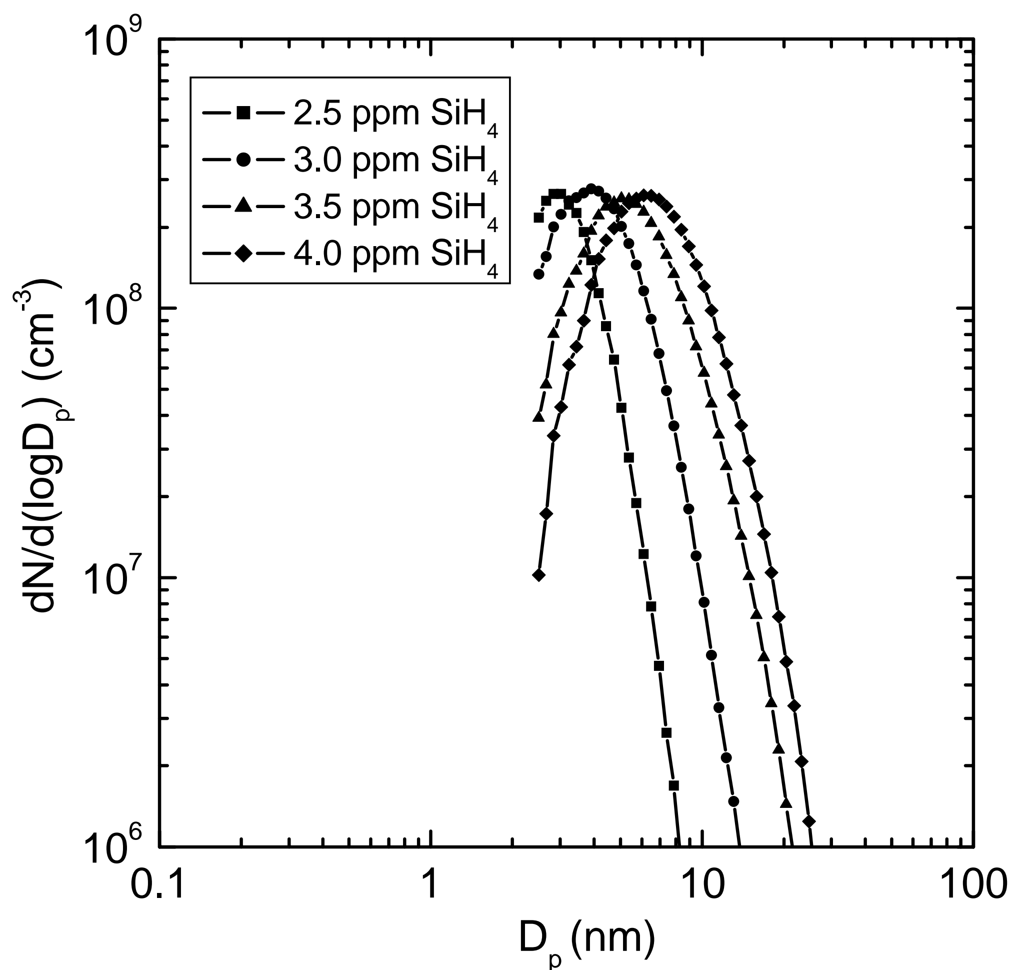

Figure 6.5. Particle size distributions of np-Si synthesized in a SiH_4/Ar microdischarge as classified by the RDMA. Plasma reactor conditions: total flow rate through the discharge=150 sccm, Ar diluent gas flow rate=450 sccm, electrode gap=1 mm, discharge current=6 mA.

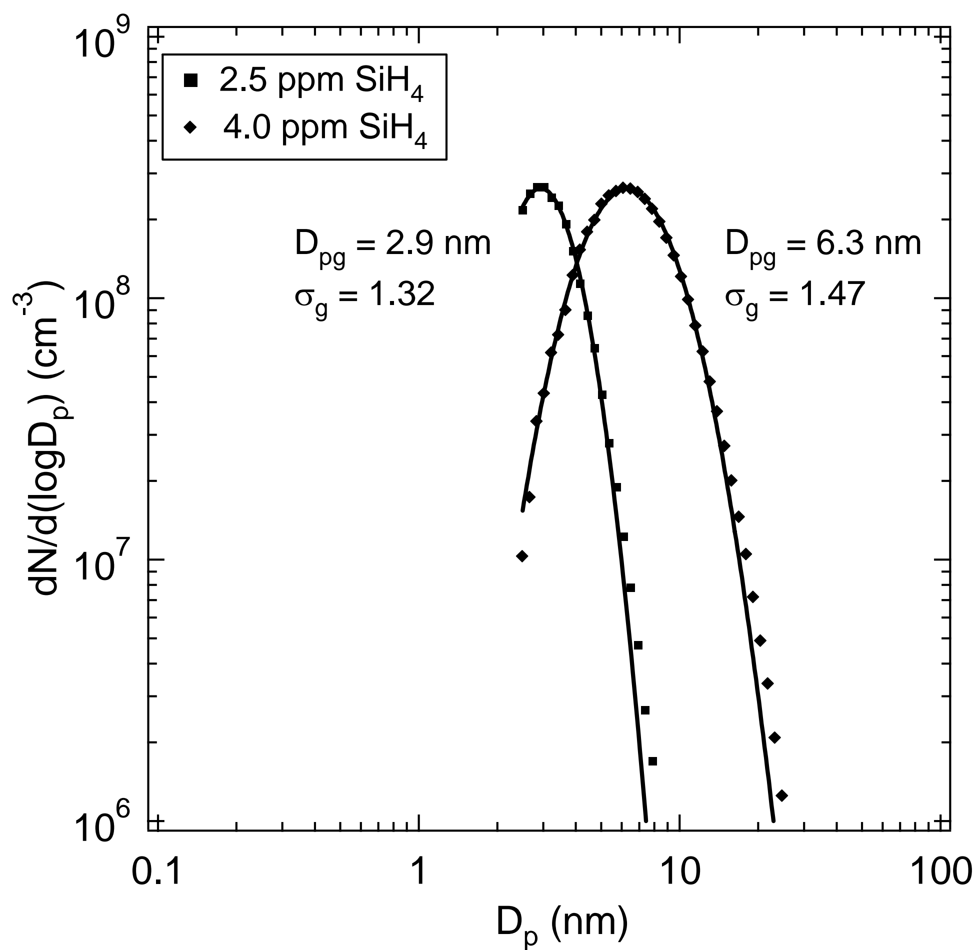

Figure 6.6. Log-normal fits to particle distributions measured in the RDMA. D_{pg} and σ_g are the geometric mean diameter and geometric standard deviation, respectively.

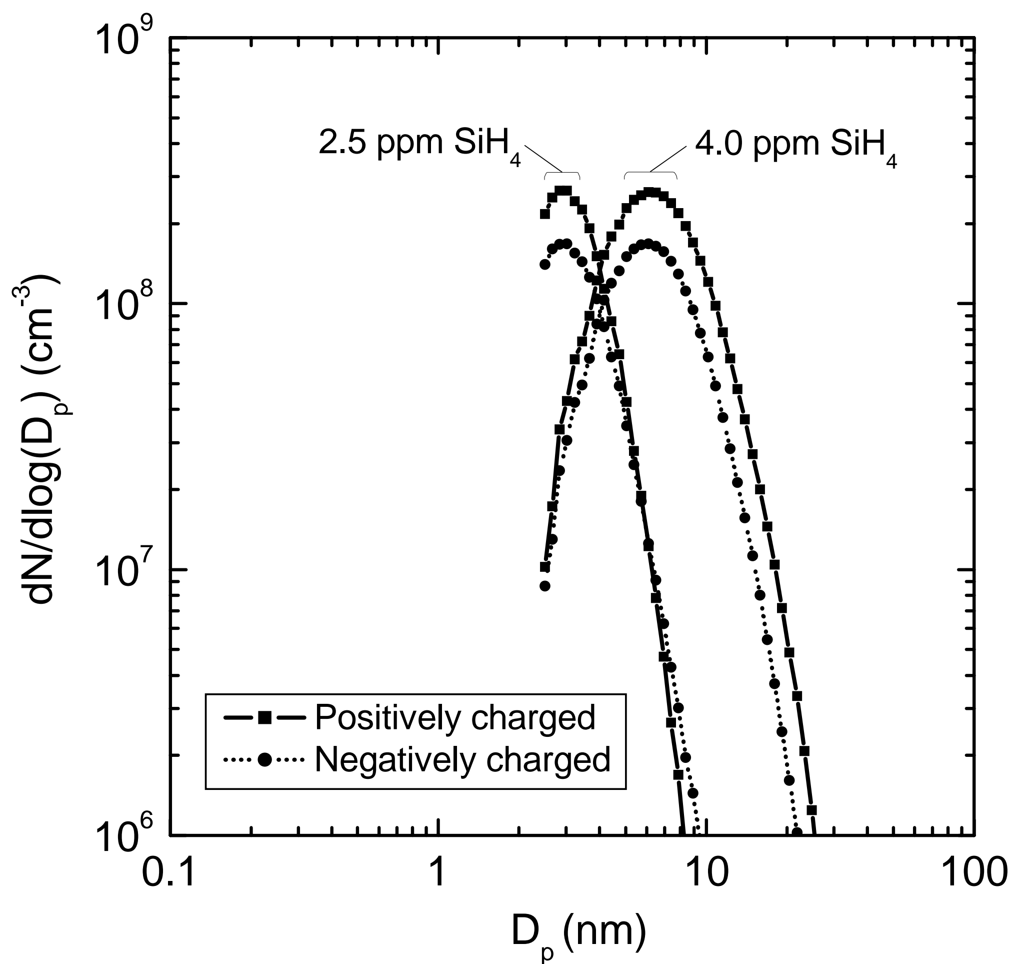

Figure 6.7. Size distributions of positively and negatively charged np-Si at two different silane concentrations as classified by the RDMA.

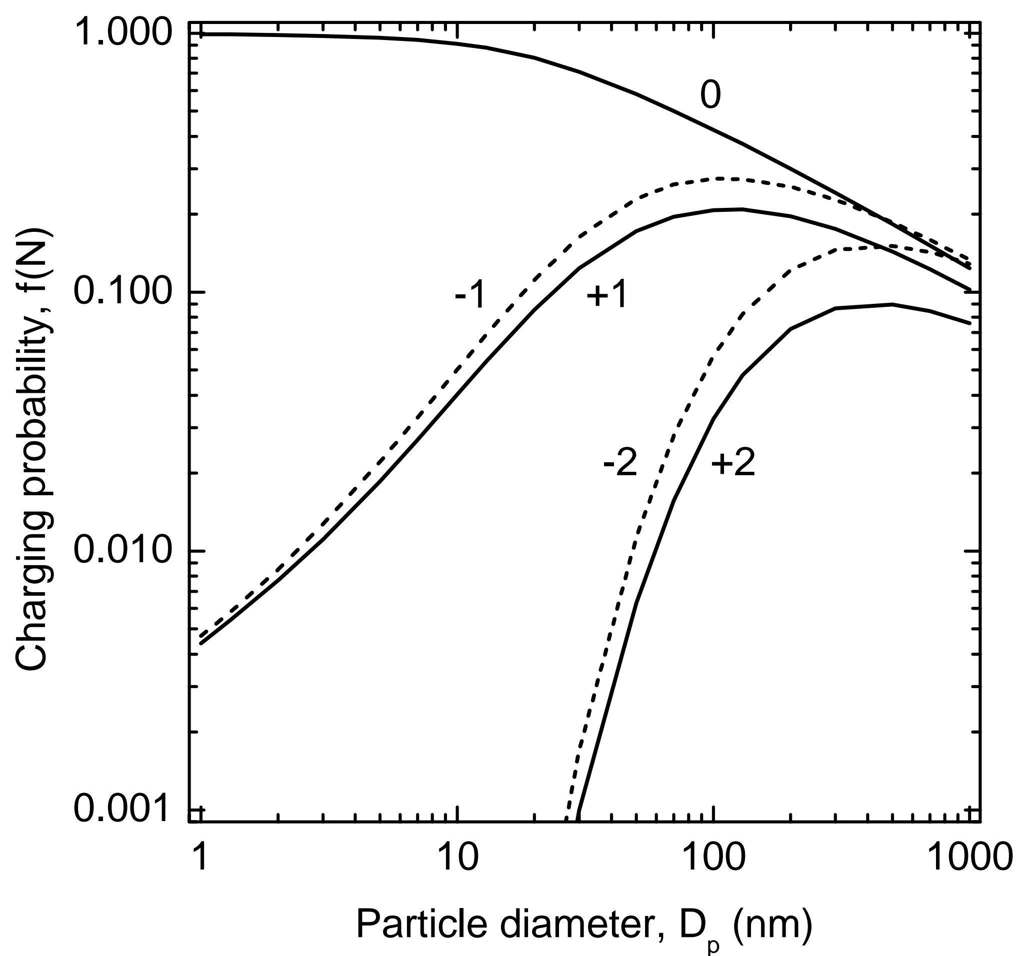

Figure 6.8. Steady-state charge distribution of particles passed through a bipolar charger (^{85}Kr β) [88].

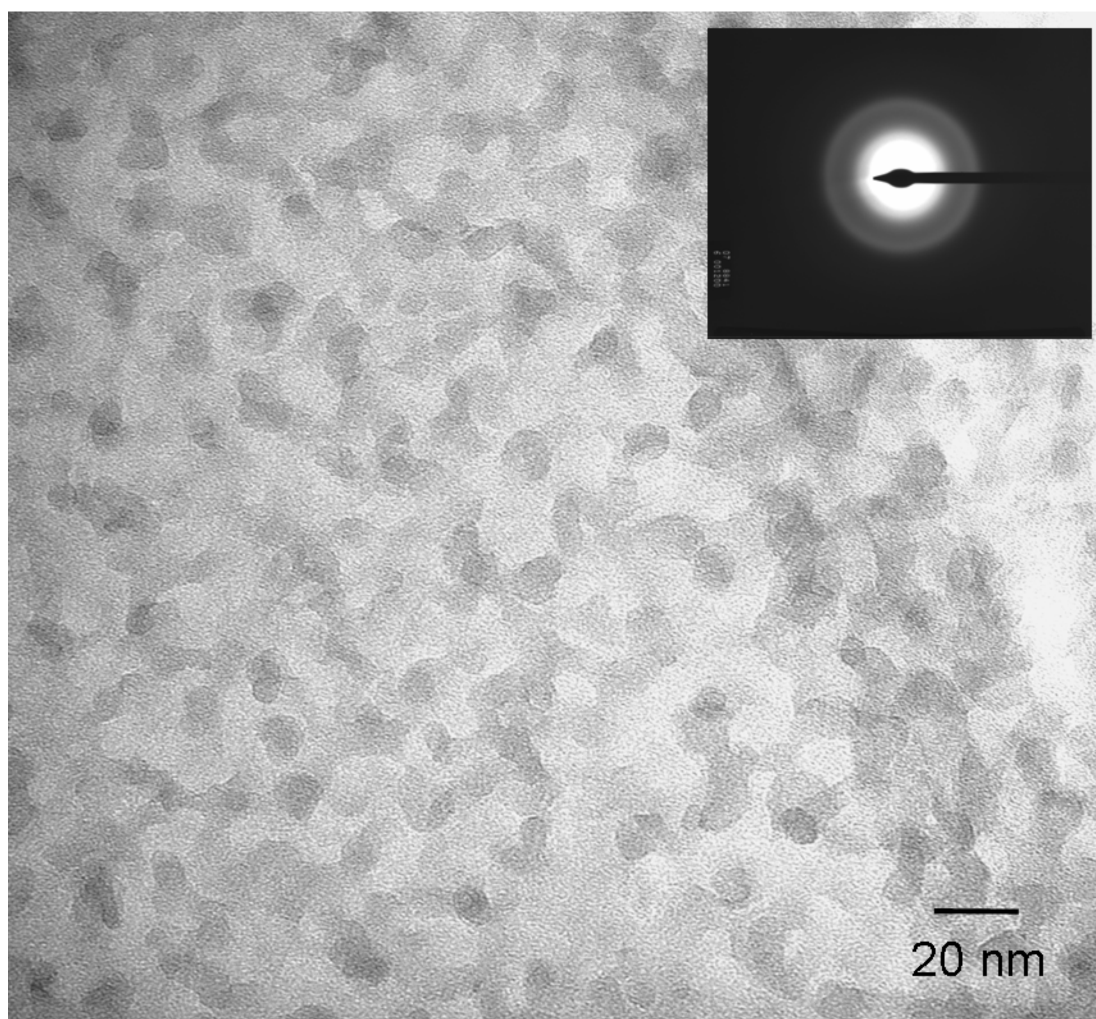

Figure 6.9. Transmission electron micrograph (TEM) of np-Si synthesized in microdischarge and deposited on carbon grid. Inset shows electron diffraction of particles.

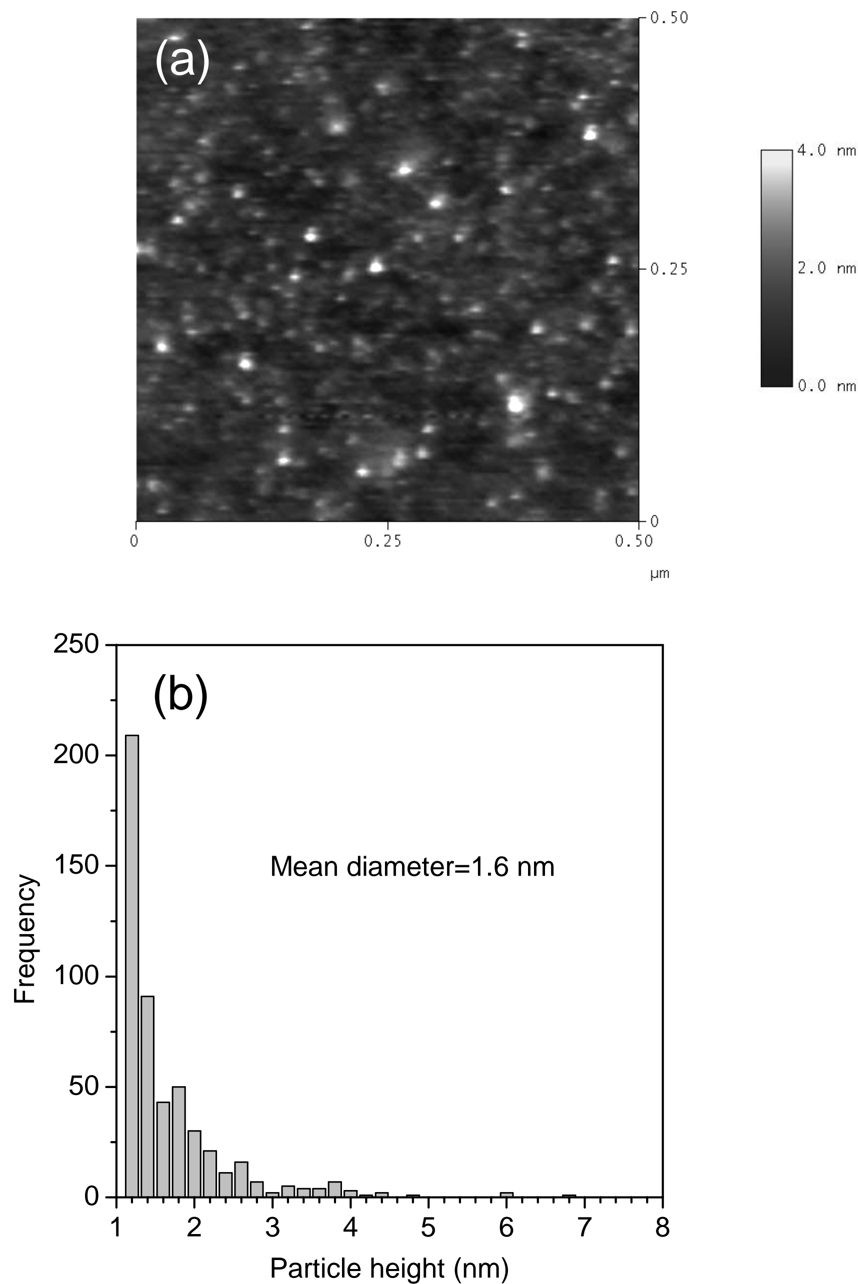

Figure 6.10. (a) Atomic force microscopy (AFM) image of np-Si drop-cast from hexane solution onto a crystalline Si wafer. (b) Histogram of np-Si heights measured by AFM.

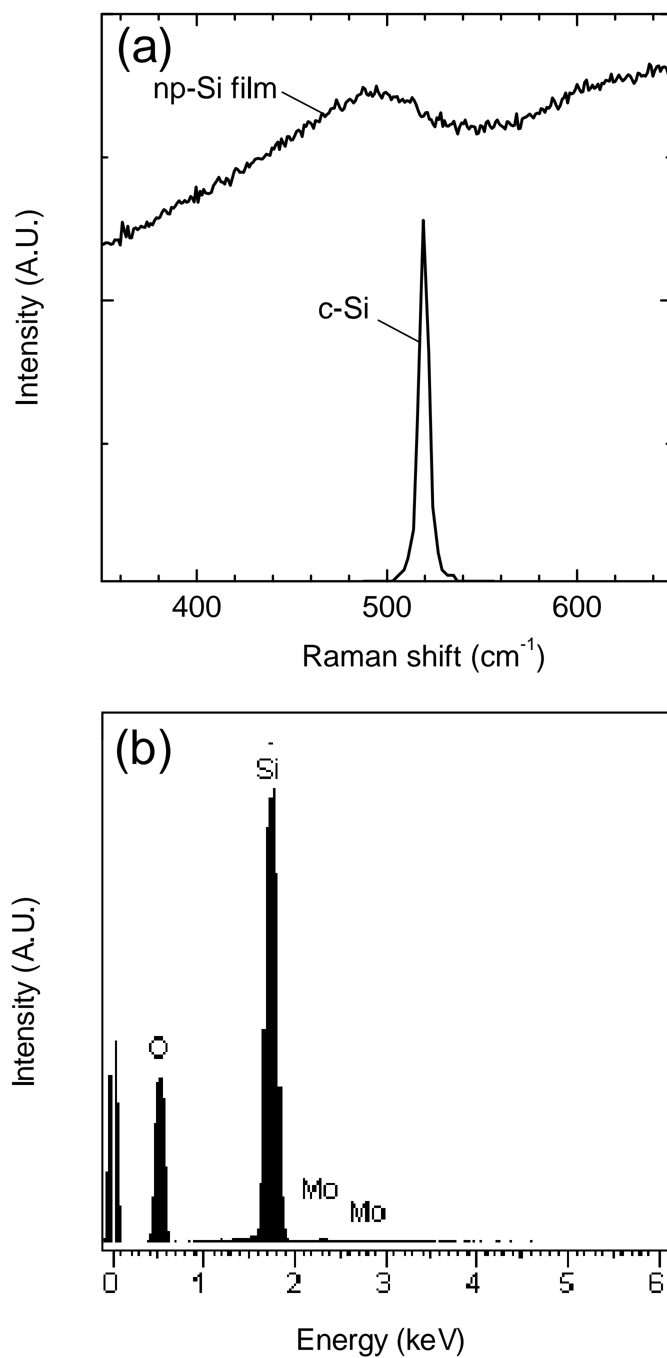

Figure 6.11. Characterization of np-Si film deposited on molybdenum substrate by (a) micro-Raman spectroscopy and (b) energy dispersive spectroscopy. Micro-Raman spectrum of crystalline Si wafer is shown for comparison as indicated.

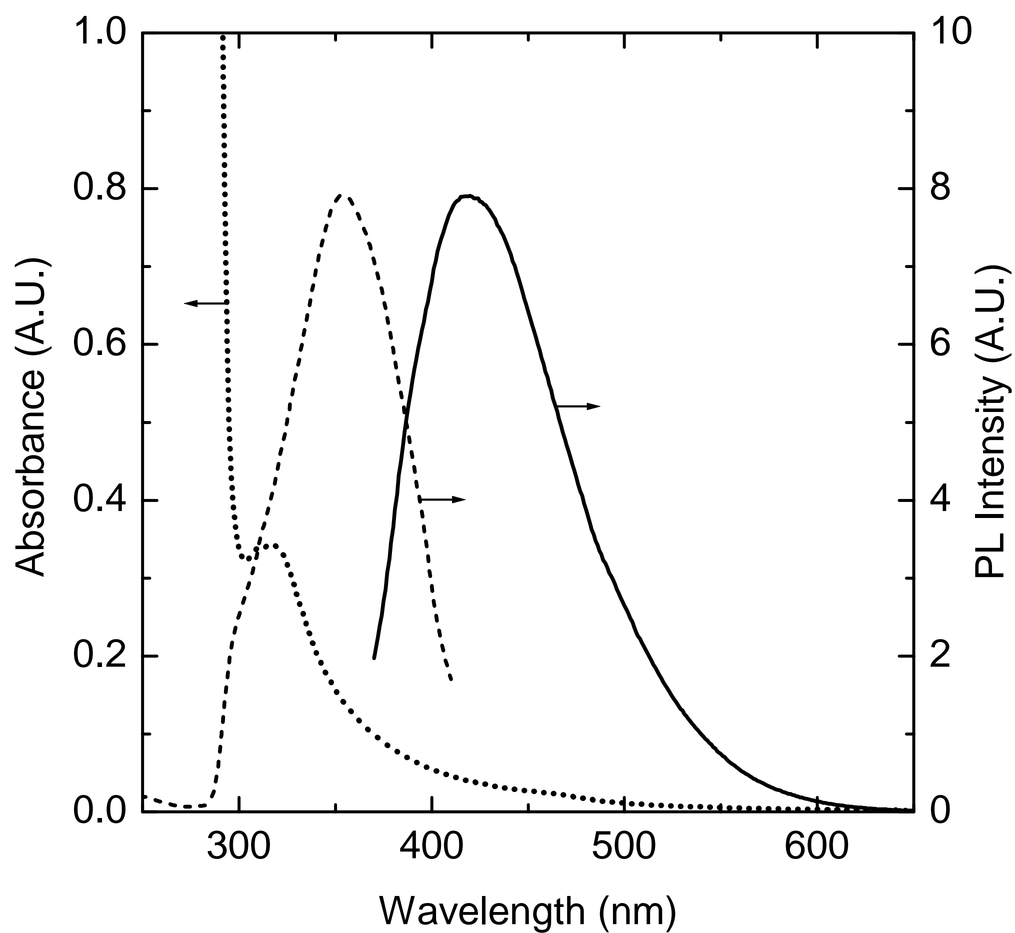

Figure 6.12. Room temperature absorbance (dotted line), PL excitataion (dashed line), and PL emission (solid line) spectra of np-Si in hexane solution. The PL emission is obtained with fixed excitation wavelength at 360 nm while the excitation spectrum is collected by fixing the detection at 420 nm.

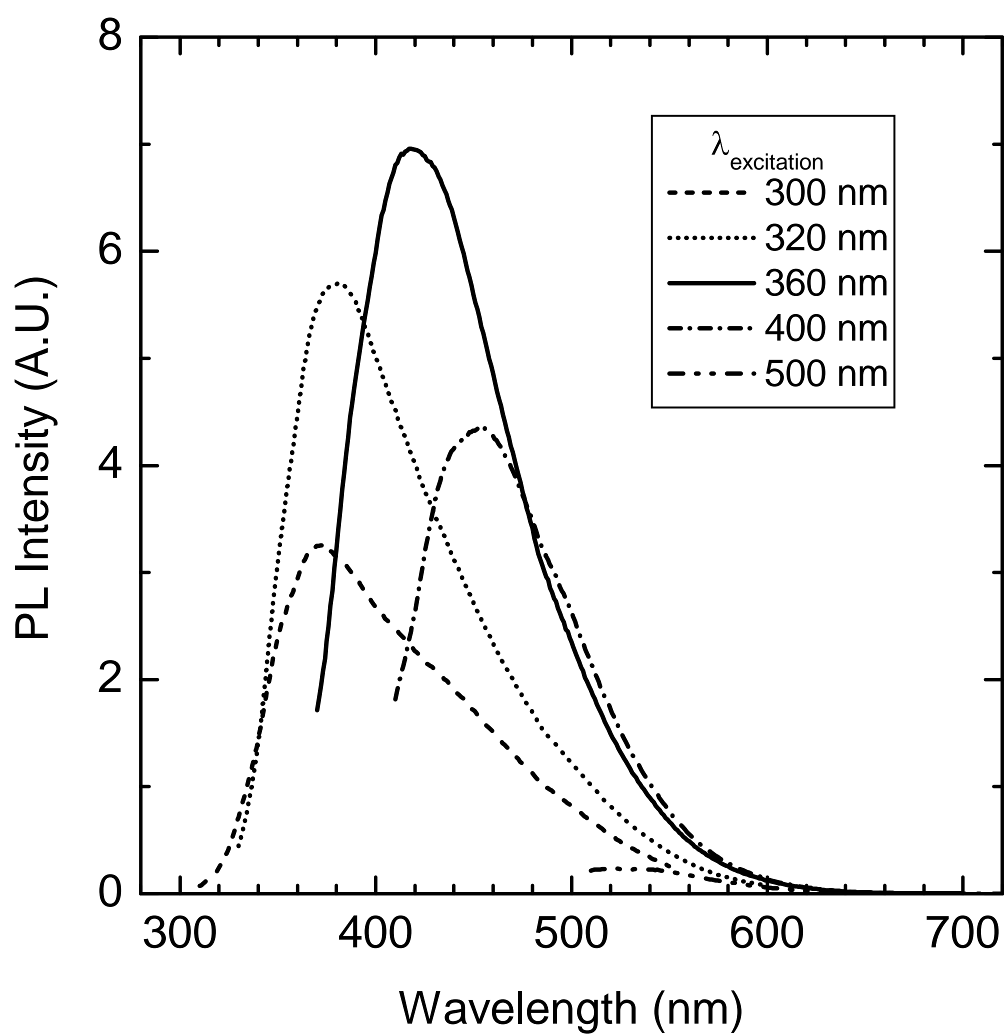

Figure 6.13. Room temperature PL spectra of np-Si in hexane solution as a function of excitation wavelength.

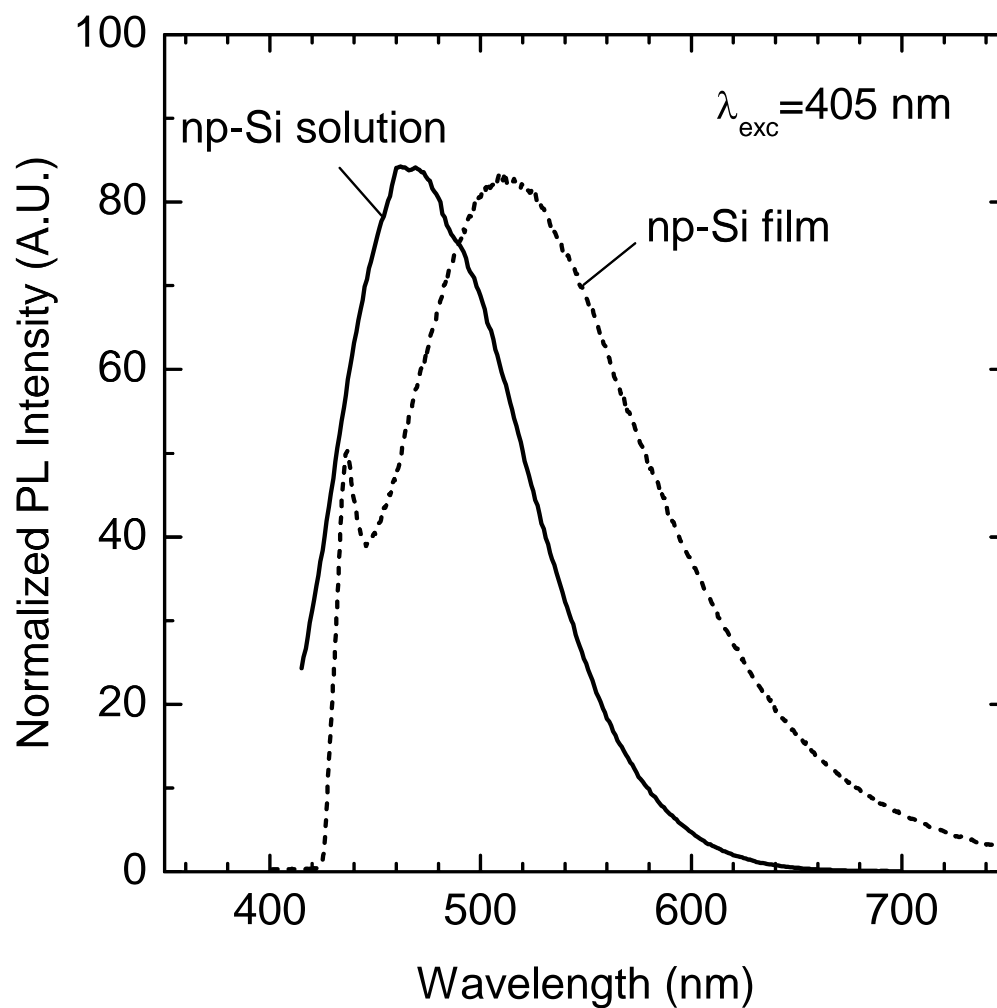

Figure 6.14. Room temperature PL spectrum of a np-Si film deposited on molybdenum substrate (dashed line), excited by a 20 mW GaN laser line at 405 nm. The sharp peak at 438 nm is an artifact of the cutoff filter used in the setup. Shown for comparison is a PL spectrum of np-Si in hexane solution also excited at 405 nm using a lamp.

Chapter 7

FUTURE APPLICATIONS OF MICRODISCHARGES

The versatility of microdischarges has been demonstrated by their applications in a broad range of technological areas. Because of their microscale dimensions, high-pressure stability, and intense ionization, microdischarges offer exciting possibilities for future studies. In this chapter, some future directions for the projects we have already explored are presented. In addition, a new application for microdischarges in gas conversion is proposed.

7.1 Etching

Etching structures with a planar microdischarge as a stencil mask has shown limitations in the pattern transfer. Using plasma microjets as an etch tool may allow deeper holes to be etched. For applications where a through hole is desired, this technique could offer a simple route to achieving rapid etch rates. If the plasma microjet is electrically isolated from the substrate, it would also be possible to etch insulating materials. Lines and other patterns could be etched by moving the plasma microjet across the substrate similar to a machine tool. In contrast to other techniques such as laser drilling and milling, the plasma microjet enables reactive removal of material which should be more efficient.

7.2 Film deposition

The ability of plasma microjets to function as a radical source for materials growth has been illustrated by its application to diamond deposition. The technique is general and should be applicable to depositing other film chemistries. A possible material for study is carbon nitride which has been experimentally difficult to grow. The superhard β-C_3N_4 phase has been predicted to have novel material properties similar to or better than diamond [95]. CVD methods similar to those used for diamond film growth have had some success synthesizing carbon nitride [96]. The main challenge for the synthesis of carbon nitride is the incorporation of nitrogen into carbon films. Large fluxes of atomic nitrogen are necessary to prepare carbon nitride films with high nitrogen content [97]. Microdischarges are promising as a source of atomic nitrogen because of the energetic electrons contained in the hollow cathode. The concept of using microjets as a combinatorial tool is especially relevant here to optimize discharge conditions for material synthesis.

7.3 Excimer emission

Enhancement of the excimer emission in microdischarges has been limited by gas heating. While convective cooling with gas flow shows improvement, the increase in excimer emission is only incremental. Operation of the microdischarge with pulsed electric fields could increase the excimer intensity without heating the gas. Nanosecond voltage

pulsing has been found to excite electrons without considerable increase in the gas temperature [98]. The temporary shift in electron energy towards higher energies causes an increase in the ionization rate and, as a result, a rise in the electron density. This effect could expand the discharge in a single metal capillary tube and increase the excimer intensity.

7.4 Nanoparticle synthesis

The luminescence mechanism in our synthesized silicon nanoparticles is still not understood. To clarify the mechanism, the role of surface effects must be determined. One approach is to controllably oxidize the surface of the particle to induce shifts in the photoluminescence [61]. Particles can be oxidized as they form by adding oxygen to the quench gas in our process. The mixing of small amounts of O_2 in the plasma afterglow should allow a thin oxide to form on the surface of the Si nanoparticles. Changing the concentration of O_2 in an inert gas permits control of the oxide thickness. PL studies could be performed as before by bubbling the particles into a liquid.

The aerosol synthesis route for nanoparticle growth is easily adaptable to different materials simply by changing the gas precursor. An important study would be to compare the properties of silicon nanoparticles to other semiconductors. For example, while germanium is an indirect band gap material like silicon, it has a band gap energy of 0.76 eV as compared to 1.12 eV for silicon. Experimental investigations on Ge nanocrystals have shown quantum confinement effects similar to Si [99]. Some studies have suggested that below a critical size, Ge nanoparticles should show stronger quantum confinement than Si [100]. Since we expect that our synthesis route is limited to producing particles between 1

and 2 nm, it should be possible to produce Ge nanoparticles at the same sizes. Measuring the PL of similarly sized particles can confirm if the band gap indeed shifts to higher energies.

7.5 Gas processing applications

The dimensions of microdischarges make them suitable for gas-phase reactions at pressures exceeding 1 atmosphere on extremely short time- and length-scales. Chemical processing in microreactors offers several advantages over traditional large-scale reactors including point-of-use capability, improved safety, and attainability of unique process conditions [101]. For example, studies by Schmidt *et al.* on millisecond/microsecond reactors have shown great promise in the partial oxidation of methane [102]. The reaction of methane and oxygen is a combustion reaction; it is highly exothermic and the thermodynamically-favored products are carbon dioxide and water. Kinetic control of the reaction results in conversion of methane, a cheap and abundant source, to more valuable liquid fuels and chemicals. In Schmidt's experiments, gases are passed across a heated metal wire gauze catalyst ($T>1000$ ^{o}C) and quenched as shown in Fig. 7.1. The short contact times are necessary to minimize the contributions from non-selective homogenous reactions, allowing the selective catalytic partial oxidation processes to dominate. The rapid rise in temperature depicted in Fig. 7.1 is an essential feature of the process to heat the gases only at the catalytic surface. An analogous setup is possible with microplasmas (see Fig. 7.1) where gases are now disassociated by electron impact and perhaps thermal decomposition. Similar

to the case of the wire gauze catalyst, radicals would form in the plasma, react to form products, and be rapidly quenched.

We have performed some preliminary experiments involving gas conversion using microplasmas. An example where microplasmas could provide significant enhancement is the generation of ozone. Ozone is a valuable commercial chemical with applications in water treatment, air clean-up, and medical sterilization. Since it is a free radical species that is highly reactive, it must be synthesized locally as needed. Ozone is produced from O_2 by the following reaction:

$$O_2 + O + M \rightarrow O_3 + M \tag{7.1}$$

where O is an excited atomic oxygen state and M is a third body that could be oxygen or another gas atom or molecule such as N_2. This reaction should look familiar; it is mechanistically the same as that of excimer generation. Similar to excimers, ozone forms by a three-body process that is favorable at high pressures where the collision frequency is high. Although plasmas such as corona discharges and dielectric barrier discharges (DBDs) have been successfully implemented in generating ozone, the yields are often low and the power requirements are extremely large. Short residence times are required in the reaction zone for efficient ozone production because ozone is decomposed by thermal process and collisions with low-energy electrons.

Experiments to investigate ozone generation were performed by passing O_2/Ar gas mixtures through a plasma microjet and measuring the ozone concentration in the gas effluent with UV absorption photometry [103]. Since ozone has a known absorption cross-section at 254 nm, this technique is an excellent *in situ* monitor of the absolute ozone

concentration [104]. The results for ozone yield and efficiency are shown in Fig. 7.2. It is clear that using more power (current) decreases the concentration of ozone produced. This is expected since an increase in the discharge current results in heating and a higher electron density which should cause a reduction in ozone formation. If higher powers are to be used, either the residence time of ozone in the microplasma will have to be decreased or the discharge will have to be cooled to avoid ozone decomposition. Although the ozone yields are lower than other large-scale processes, our efficiencies are comparable to some of the largest values that have been obtained in the range of 10-50 g/kW-h. The application of microreactors for ozone generation is promising if we can continue to reduce the residence time and control the power dissipation in the microdischarge. In addition, unlike alternative plasma sources, the microscale nature is attractive as a compact, point-of-use ozone generator.

The physical properties of microdischarges are potentially useful for gas processing applications. Hollow cathode operation leads to unique discharge characteristics including the formation of energetic electrons and stable operation at high pressures. Intense ionization in a small volume results in an extremely high power density (more than 10^3 kW/cm^3) that permits the efficient disassociation of gases. A by-product of power dissipation is gas heating which is detrimental to processes such as ozone generation. Future studies will have to overcome these issues by investigating shorter residence times and more effective cooling of the discharge.

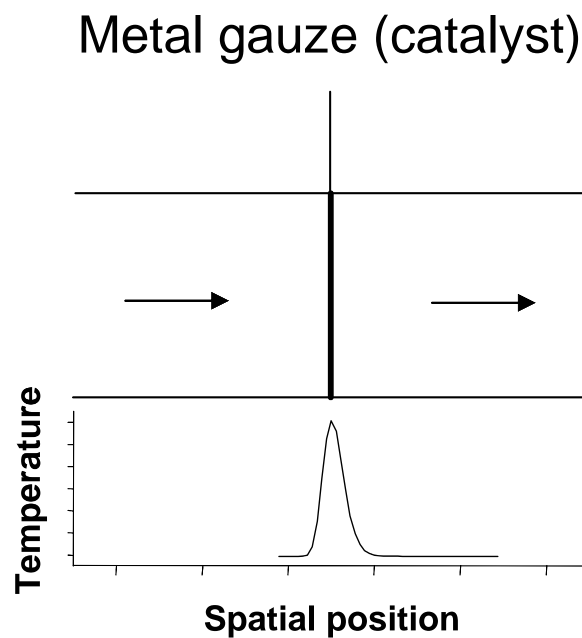

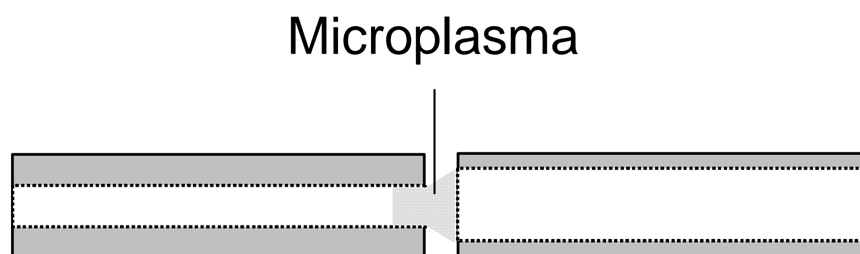

Figure 7.1. Illustration of short contact time millisecond/microsecond reactors. The top picture shows a reactor setup with a hot wire metal gauze catalyst and its approximate temperature profile [102]. Also shown is an analogous setup with a microplasma (bottom).

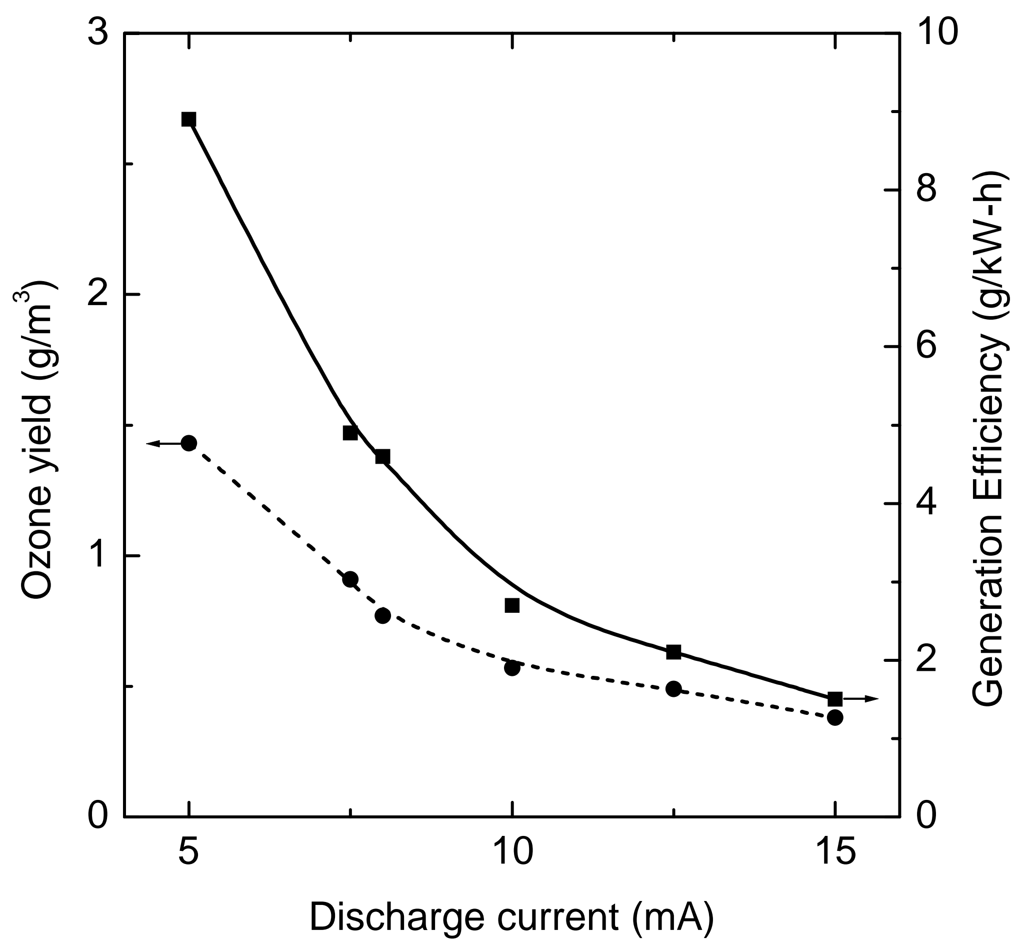

Figure 7.2. Ozone production in an O_2/Ar plasma microreactor as a function of current. The ozone concentration in the gas effluent was measured by UV absorption photometry (λ_{abs}=254 nm). Plasma conditions: 360 sccm Ar + 40 sccm O_2, 1 mm gap.

BIBILIOGRAPHY

[1] F. Chen, *Introduction to Plasma Physics and Controlled Fusion*, Plenum Press, New York, New York, 1984.

[2] M. A. Liebermann and A. J. Lichtenberg, *Principles of Plasma Discharges and Materials Processing*, John Wiley & Sons, Inc., New York, New York, 1994.

[3] A. von Engel, *Ionized Gases*, Clarendon, Oxford, 1965.

[4] Y. P. Raizer, *Gas Discharge Physics*, Springer, Berlin, Germany, 1991.

[5] F. M. Penning, *Electrical Discharges in Gases*, The Macmillan Company, New York, New York, 1957.

[6] F. W. Aston, Proc. R. Soc. A **79**, 80 (1907).

[7] J. D. Cobine, *Gaseous Conductors*, Dover, New York, 1958.

[8] F. Paschen, Ann. Physik **50**, 901 (1916).

[9] A. Güntherschulze, Z. Physik **19**, 313 (1923).

[10] A. D. White, J. Appl. Phys. **30**, 711 (1959).

[11] P. F. Little and A. von Engel, Proc. R. Soc. London, Ser. A **224**, 209 (1954).

[12] D. J. Sturges and H. J. Oskam, J. Appl. Phys. **35**, 2887 (1964).

[13] P. Gill and C. E. Webb, J. Phys. D. **10**, 299 (1977).

[14] K. H. Schoenbach, A. El-Habachi, W. Shi, and M. Ciocca, Plasma Sources Sci. Technol. **6**, 468 (1997).

[15] S-J. Park, C. J. Wagner, C. M. Herring, and J. G. Eden, Appl. Phys. Lett. **77**, 199 (2000).

[16] A. El-Habachi and K. H. Schoenbach, Appl. Phys. Lett. **72**, 22 (1998).

[17] R. M. Sankaran and K. P. Giapis, J. Appl. Phys. **92**, 2406 (2002).

[18] R. M. Sankaran, M. J. Gordon, K. P. Giapis, "Method and apparatus for providing flow-stabilized microdischarges in metal capillaries," U.S. Patent No. 6,700,329 (2004).

[19] K. H. Schoenbach, A. El-Habachi, M. M. Moselhy, W. Shi, and R. H. Stark, Phys. Plasmas **7**, 2186 (2000).

[20] V. Kapicka, M. Sicha, M. Klima, Z. Hubicka, J. Tous, A. Brablec, P. Slavicek, J. F. Behnke, M. Tichy, and R. Vaculik, Plasma Sources Sci. Technol. **8**, 15 (1999).

[21] M. Sira, M. Klima, J. Janca, V. Kapicka, and M. Capoun, Czech. J. Phys. **50**, 415 (2000).

[22] J. Kousal, M. Klima, J. Janca, V. Kapicka, P. Slavicek, A. Brablec, and P. Sulovsky, Czech. J. Phys. **50**, 409 (2000).

[23] W. Shi, R. H. Stark, and K. H. Schoenbach, IEEE Trans. Plasma Sci. **27**, 16 (1999).

[24] S-I. Pai, *Fluid Dynamics of Jets,* D. Van Nostrand Company, Inc., New York, New York, 1954.

[25] V. S. Borodin and Y. M. Kagan, Sov. Phys. Tech. Phys. **11**, 131 (1966).

[26] J. W. Frame, D. J. Wheeler, T. A. DeTemple, and J. G. Eden, Appl. Phys. Lett. **71**, 1165 (1997).

[27] S. J. Park and J. G. Eden, Appl. Phys. Lett. **81**, 4127 (2002).

[28] B. Cho, J. Ryu, S. Hwang, G. Lee, and S. H. Moon, J. Vac. Sci. Technol. B **18**, 2769 (2000).

[29] W. R. Harshbarger, R. A. Porter, T. A. Miller, and P. Norton, Appl. Spec. **31**, 1 (1977).

[30] F. Jansen, D. Kuhman, C. Taber, J. Vac. Sci. Technol. A **7**, 3176 (1989).

[31] L. Bardos and V. Dusek, Thin Solid Films **158**, 265 (1988).

[32] H. Barankova, L. Bardos, and S. Berg, J. Electrochem. Soc. **142**, 883 (1995).

[33] H. Barankova, L. Bardos, and S. Berg, J. Vac. Sci. Technol. A **14**, 3033 (1996).

[34] L. Bardos, H. Barankova, and S. Berg, Surf. Coat. Tech. **97**, 723 (1997).

[35] L. S. Pan and D. R. Kania, *Diamond: Electronic Properties and Applications*, Kluwer Academic Publishers, Boston, Massachusetts, 1995.

[36] R. F. Davis, *Diamond Films and Coatings*, Noyes Publications, Park Ridge, New Jersey, 1993.

[37] D. G. Goodwin, Appl. Phys. Lett. **59**, 277 (1991).

[38] J. C. Angus, H. A. Will, and W. S. Stanko, J. Appl. Phys. **39**, 2915 (1968).

[39] R. W. B. Pearse and A. G. Gaydon, *The Identification of Molecular Spectra* (John Wiley and Sons, Inc., New York, 1950), p. 79.

[40] D. G. Goodwin, J. Appl. Phys. **74**, 6888 (1993).

[41] M. A. Cappelli, T. G. Owano, and C. H. Kruger, J. Mater. Res. **5**, 2326 (1990).

[42] R. J. Nemanich, J. T. Glass, G. Lucovsky, and R. E. Shroder, J. Vac. Sci. Technol. A **6**, 1783 (1988).

[43] N. Thonnard and G. S. Hurst, Phys. Rev. A. **5**, 1110 (1972).

[44] P. K. Leichner, Phys. Rev. A **8**, 815 (1973).

[45] P. Kurunczi, H. Shah, and K. Becker, J. Phys. B **32**, L651 (1999).

[46] A. El-Habachi, W. Shi, M. Moselhy, R. H. Stark, and K. H. Schoenbach, J. Appl. Phys. **88**, 3220 (2000).

[47] J. W. Frame, P. C. John, T. A. DeTemple, and J. G. Eden, Appl. Phys. Lett. **72**, 2634 (1998).

[48] B. A. Vojak, S.-J. Park, C. J. Wagner, and J. G. Eden, Appl. Phys. Lett. **78**, 1340 (2001).

[49] M. Moselhy, R. H. Stark, K. H. Schoenbach, and U. Kogelschatz, Appl. Phys. Lett. **78**, 880 (2001).

[50] R. J. Carman and R. P. Mildern, J. Phys. D. **36**, 19 (2003).

[51] M. Moselhy and K. H. Schoenbach, J. Appl. Phys. **95**, 1642 (2004).

[52] J. D. Ametepe, J. Diggs, D. M. Manos, and M. J. Kelley, J. Appl. Phys. **85**, 7505 (1999).

[53] D. J. Eckstrom, H. H. Nakano, D. C. Lorents, T. Rothem, J. A. Betts, M. E. Lainhart, D. A. Dakin, and J. E. Maenchen, J. Appl. Phys. **64**, 1679 (1988).

[54] P. Dubé, T. Efthimiopoulos, M. J. Kiik, and B. P. Stoicheff, Opt. Lett. **16**, 1887 (1991).

[55] E. F. Labuda, E. I. Gordon, and R. C. Miller, IEEE J. Quantum Electron. **QE-1**, 273 (1965).

[56] A. P. Alivisatos, Science **271**, 933 (1996).

[57] C. B. Murray, D. J. Norris, M. G. Bawendi, J. Am. Chem. Soc. **115**, 8706 (1993).

[58] L. T. Canham, Appl. Phys. Lett. **57**, 1046 (1990).

[59] S. Furukawa and T. Miyasato, Phys. Rev. B **38**, 5726 (1988).

[60] W. L. Wilson, P. F. Szajowski, and L. E. Brus, Science **262**, 1242, 1993.

[61] M. V. Wolkin, J. Jorne, P. M. Fauchet, G. Allan, and C. Delerue, Phys. Rev. Lett. **82**, 197 (1999).

[62] A. Puzder, A. J. Williamson, J. C. Grossman, and G. Galli, Phys. Rev., Lett. **88**, 097401-1 (2002).

[63] J. R. Heath, Science **258**, 1131 (1992).

[64] J. P. Wilcoxon, G. A. Samara, and P. N. Provencio, Phys. Rev. B **60**, 2704 (1999).

[65] J. D. Holmes, K. J. Ziegler, R. C. Doty, L. E. Pell, K. P. Johnston, and B. A. Korgel, J. Am. Chem. Soc. **123**, 3743 (2001).

[66] D. E. Harwell, J. C. Croney, W. Qin, J. T. Thornton, J. H. Day, E. K. Hajime, and D. M. Jameson, Chem. Lett. **32**, 1194 (2003).

[67] K. A. Littau, P. J. Szajowski, A. J. Muller, A. R. Kortan, and L. E. Brus, J. Phys. Chem. **97**, 1224 (1993).

[68] S. Schuppler, S. L. Friedman, M. A. Marcus, D. L. Adler, Y. H. Xie, F. M. Ross, Y. J. Chabal, T. D. Harris, L. E. Brus, W. L. Brown, E. E. Chaban, P. F. Szajowski, S. B. Christman, and P. H. Citrin, Phys. Rev. B **52**, 4910 (1995).

[69] R. P. Camata, H. A. Atwater, K. J. Valhala, and R. C. Flagan, Appl. Phys. Lett. **68**, 3162 (1996).

[70] M. L. Ostraat, J. W. DeBlauwe, M. L. Green, L. D. Bell, M. L. Brongersma, J. Casperson, R. C. Flagan, H. A. Atwater, Appl. Phys. Lett. **79**, 433 (2001).

[71] N. Rao, B. Micheel, D. Hansen, C. Fandrey, M. Bench, S. Girschick, J. Heberlein, and P. McMurry, J. Mater. Res. **10**, 2073 (1995).

[72] N. Rao, S. Girschick, J. Heberlein, P. McMurry, S. Jones, D. Hansen, and B. Micheel, Plasma Chem. Plasma Process. **15**, 581 (1995).

[73] T. Seto, Y. Kawakami, N. Suzuki, M. Hirasawa, and N. Aya, Nano Lett. **1**, 315 (2001).

[74] T. Orii, M. Hirasawa, and T. Seto, Appl. Phys. Lett. **83**, 3395 (2003).

[75] X. Li, Y. He, S. Talukdar, and M. T. Swihart, Langmuir **19**, 8490 (2003).

[76] G. Viera, M. Mikikian, E. Bertran, P. R. i Cabarrocas, and L. Boufendi, J. Appl. Phys. **92**, 4684 (2002).

[77] Z. Shen, T. Kim, U. Kortshagen, P. H. McMurry, and S. A. Campbell, J. Appl. Phys. **94**, 2277 (2003).

[78] M. H. Nayfeh, O. Akcakir, G. Belomoin, N. Barry, J. Therrien, and E. Gratoon, Appl. Phys. Lett. **77**, 4086 (2000).

[79] M. H. Nayfeh, N. Barry, J. Therrien, O. Akcakir, E. Gratton, and G. Belomoin, Appl. Phys. Lett. **78**, 1131 (2001).

[80] R. C. Flagan and M. M. Lunden, Mat. Sci. Eng. A. **A204**, 113 (1995).

[81] R. P. Camata, *Aerosol Synthesis and Characterization of Silicon Nanocrystals*, Ph.D. dissertation, California Institute of Technology, Pasadena, California, 1998.

[82] S. H. Zhang, Y. Akutsu, L. M. Russell, and R. C. Flagan, Aerosol Sci. Technol., **23** 357, (1995).

[83] J. H. Seinfeld and S. N. Pandis, *Atmospheric Chemistry and Physics: From Air Pollution to Climate Change*, John Wiley & Sons, Inc., New York, New York, 1998.

[84] T. Makino, N. Suzuki, Y. Yamada, T. Yoshida, T. Seto, and N. Aya, Appl. Phys. A **69**, S243 (1999).

[85] N. Suzuki, T. Makino, Y. Yamada, T. Yoshida, and T. Seto, Appl. Phys. Lett. **78**, 2043 (2001).

[86] T. Matsoukas, M. Russell, and M. Smith, J. Vac. Sci. Technol. A **14**, 624 (1996).

[87] E. Stoffels, W. W. Stoffels, G. M. W. Kroesen, and F. J. de Hoog, J. Vac. Sci. Technol. A **14**, 556 (1996).

[88] A. Wiedensohler, J. Aerosol Sci. **19**, 387 (1988).

[89] R. K. Baldwin, K. A. Pettigrew, E. Ratai, M. P. Augustine, and S. M. Kauzlarich, Chem. Commun. **17**, 1822 (2002).

[90] N. Chaabane, A. Kharchencko, H. Vach, and P. Cabarrocas, New J. Phys. **5**, 37.1 (2003).

[91] T. Seto, T. Orii, M. Hirasawa, and N. Aya, Thin Solid Films **437**, 230 (2003).

[92] A. Puzder, A. Williamson, J. C. Grossman, and G. Galli, J. Am. Chem. Soc. **125**, 2786 (2003).

[93] G. Belomoin, J. Therrien, and M. Nayfeh, Appl. Phys. Lett. **77**, 779 (2000).

[94] D. S. English, L. E. Pell, Z. Yu, P. F. Barbara, and B. A. Korgel, Nano Lett. **2**, 681 (2002).

[95] A. Y. Liu and M. L. Cohen, Science **245**, 841 (1989).

[96] T. Yen and C. Chou, Appl. Phys. Lett. **67**, 2801 (1995).

[97] C. Niu, Y. Lu, and C. M. Lieber, Science **261**, 334 (1993).

[98] R. H. Stark and K. H. Schoenbach, J. Appl. Phys. **89**, 3568 (2001).

[99] J. P. Wilcoxon, P. P. Provencio, and G. A. Samara, Phys. Rev. B **64**, 035417-1 (2001).

[100] C. Bostedt, T. van Buuren, T. M. Wiley, N. Franco, and L. J. Terminello, Appl. Phys. Lett. **84**, 4056 (2004).

[101] W. Ehrfeld, V. Hessel, and H. Löwe, *Microreactors: New Technology for Modern Chemistry*, Wiley-VCH, New York, New York, (2000).

[102] D. A. Goetsch and L. D. Schmidt, Science **271**, 1560 (1996).

[103] G. Nair, *Ozone Generation by Microhollow Cathode Discharges in an Ar/*O_2 *Plasma*, ChE 126B Report (Chemical Engineering Undergraduate Laboratory), 2004.

[104] W. B. DeMore, S. P. Sander, D. M. Golden, C. J. Howard, A. R. Ravishankara, C. E. Kolb, and M. J. Molina, *Chemical Kinetics and Photochemical Data for Use in Stratospheric Modelling*, JPL Pub. 94-26, Jet Propulsion Laboratory, Pasadena, California, 1994.